

UC Berkeley

UC Berkeley Electronic Theses and Dissertations

Title

Search for Non-pointing and Delayed Photons in pp collisions at $\sqrt{s}=13$ TeV using the ATLAS detector

Permalink

<https://escholarship.org/uc/item/63j1q7m6>

Author

Santpur, Sai Neha

Publication Date

2022

Peer reviewed|Thesis/dissertation

Search for Non-pointing and Delayed Photons in pp collisions at $\sqrt{s}=13$ TeV using the
ATLAS detector

by

Sai Neha Santpur

A dissertation submitted in partial satisfaction of the

requirements for the degree of

Doctor of Philosophy

in

Physics

in the

Graduate Division

of the

University of California, Berkeley

Committee in charge:

Professor Marjorie Shapiro, Chair

Professor Kam-Biu Luk

Professor Karl Van Bibber

Spring 2022

Search for Non-pointing and Delayed Photons in pp collisions at $\sqrt{s}=13$ TeV using the ATLAS detector

Copyright 2022
by
Sai Neha Santpur

Abstract

Search for Non-pointing and Delayed Photons in pp collisions at $\sqrt{s}=13$ TeV using the ATLAS detector

by

Sai Neha Santpur

Doctor of Philosophy in Physics

University of California, Berkeley

Professor Marjorie Shapiro, Chair

This thesis describes the search for displaced photons in the exotic decays of the Standard Model Higgs boson using 139 fb^{-1} of proton-proton collision data recorded by the ATLAS detector. The signal model involves the decay of the Higgs boson into a pair of long-lived supersymmetric particles, each of which subsequently decay into a photon and a stable supersymmetric particle. The current upper limits on the decays of the Higgs boson to the undetected particles is around 21% making this search extremely relevant. This analysis utilizes the ATLAS electromagnetic calorimeter's unique capabilities to measure the photon's direction of flight and its time of arrival. No significant excess was observed compared to the estimated Standard Model background and this null result was used to set 95% confidence level limits on the branching ratio of the Higgs to the pair of long-lived particles for the very first time.

"The purpose of education is to replace an empty mind with an open one." - Malcolm S.
Forbes

To my family

Contents

Contents	ii
List of Figures	v
List of Tables	xiii
1 Introduction	1
1.1 Standard model of particle physics	1
1.1.1 Particle content of SM	2
1.1.2 Strong interaction	3
1.1.3 Electroweak interaction and spontaneous symmetry breaking	4
1.2 Limitations of the Standard Model	5
1.3 Supersymmetry	5
1.3.1 Particle content	5
1.3.2 R-parity	7
1.3.3 SUSY breaking and mass eigenstates	7
1.3.4 GMSB SUSY model	8
2 Signal model and phenomenology	10
2.1 Status of displaced photon searches	11
3 ATLAS experiment	12
3.1 The Large Hadron Collider	12
3.2 The ATLAS detector	14
3.2.1 Inner detector	15
3.2.2 Calorimeters	17
3.2.3 Muon spectrometer	20
3.3 Trigger and data acquisition system (TDAQ)	21
3.3.1 Level-1 trigger (L1)	21
3.3.2 High-Level trigger (HLT)	22
4 Data and simulated signal samples	25
4.1 Data samples	25

4.2	Simulated signal samples	26
4.3	Simulated background samples	28
5	Object reconstruction	29
5.1	Tracking and vertexing	30
5.2	Photons	30
5.2.1	Photon identification	30
5.2.1.1	Prompt-photon identification efficiency	31
5.3	Electrons	35
5.4	Jets	35
5.5	Muons	35
5.6	Overlap removal	36
5.7	Missing transverse energy	36
6	Photon pointing and timing	37
6.1	Photon pointing	37
6.1.1	Non-pointing photon identification efficiency	41
6.2	Photon timing	43
7	Event selection	46
7.1	Event preselection	46
7.2	Selection optimization procedure	47
7.3	Signal and background yields	48
8	Background estimation	51
8.1	Analysis strategy	51
8.2	Background timing templates	52
8.3	KS-tests for background templates	59
8.4	Selection of the background timing templates	59
9	Systematic uncertainties	62
9.1	Background systematic uncertainties	62
9.1.1	Template shape systematics	62
9.1.2	Non-closure uncertainty	65
9.2	Signal systematic uncertainties	67
9.2.1	Theoretical uncertainties	67
9.2.2	Experimental systematics	68
9.2.3	Prompt-photon identification uncertainty	68
9.2.4	Non-pointing photon identification uncertainty	68
9.2.5	Pointing related uncertainties	68
9.2.6	Timing smearing uncertainty	72
10	Statistical analysis and background validation	75

10.1	Statistical analysis	75
10.2	Background estimation validation	77
10.2.1	High- Δm VR(t) region	77
10.2.2	Validation in low- Δm VR(t) region	77
10.2.3	Validation in VR(E_T^{miss}) region	77
10.3	Signal injection studies	78
11	Results	89
11.1	Sensitivity for the simulated signal samples	94
11.2	Interpolation of the results	95
11.2.1	Intermediate mass interpolation	95
11.2.2	Lifetime reweighting procedure	96
11.2.3	Lifetime interpolation	97
11.3	Model-independent results	101
12	Summary and outlook	107
A	Power board stress testing	109
A.1	Module	109
A.2	Power board	110
A.2.1	Components and functions	110
A.3	Power board testing	112
A.3.1	Efficiency measurement	113
A.3.2	Other measurements	114
A.4	Power board reliability measurement	114
A.4.1	Reliability definition	114
A.4.2	Failure modes of power board	114
A.5	Stress testing the power board	115
A.5.1	Power cycling test	115
A.5.2	Long-term power-on test	117
A.5.3	Thermal characterization	119
A.6	Summary and outlook	125
B	Studying performance of the Strips module using X-ray beams	127
B.1	Experimental setup	127
B.2	Results	129
B.2.1	Surface scan	129
B.2.2	Head-on scan	130
	Bibliography	134

List of Figures

1.1	Particle content of the Standard Model [7].	2
1.2	Feynman diagram of an example proton-proton collision event. The hard scatter interaction with cross section σ is shown here along with the underlying event.	9
2.1	Example Feynman diagram for the exotic decay of the Higgs boson produced in association with a Z boson. The Higgs boson decays into a pair of long-lived particles (NLSPs) which each decay into a photon and a stable LSP. The Z boson decays into leptons which are used to trigger the event.	10
3.1	Layout of the CERN accelerator complex [28].	13
3.2	Diagram of the ATLAS detector including different sub-detector systems [38].	15
3.3	Layout of the ATLAS Inner Detector [41].	16
3.4	Layout of the ATLAS calorimeters [45].	17
3.5	Sketch of the ATLAS electromagnetic calorimeter.	18
3.6	Segmentation of the Tile Calorimeter modules in radius and η shown for barrel on the left side and extended barrel on the right side.[49]	19
3.7	Layout of the ATLAS muon spectrometer system [52].	20
3.8	ATLAS trigger and data acquisition system showing the peak event rate and bandwidth at each step [54].	22
3.9	Event rate after the L1 trigger is shown for different trigger signatures for a given data-taking period in October 2015. The X-axis is time with one unit corresponding to $\tilde{60}$ s [55].	23
3.10	Event rate after the HLT trigger is shown for different trigger signatures for a given data-taking period in October 2015 [55].	24
4.1	Cumulative luminosity for pp collisions delivered to ATLAS with stable operation during Run-2 along with the luminosity recorded and the luminosity that is good for physics analysis.[56]	25
4.2	Mean number of interactions per bunch crossing for datasets recorded per year during Run-2.[56]	26
5.1	Sketch of particle paths for different objects passing through the ATLAS detector [68].	29

5.2	Invariant mass distribution $m_{ll\gamma}$ for events in data after all the other selections and before the Loose ID is applied is shown in the left plot while the distribution after the Loose ID is applied is shown in the right plot. The fit of this distribution to the data constructed from the $Zll\gamma$ process (red line) and background (blue dotted line) from the simulated samples is given by the solid blue line.	31
5.3	Loose photon identification efficiency for data and the Monte Carlo samples is shown here as a function of p_T for various η regions.	33
5.4	Scale factors as a function of photon p_T six different η regions. The red line corresponds to the value of 1.0 is for an easier eye guide.	34
6.1	Cartoon showing the shower shape of a photon shower in different layers of the ATLAS electromagnetic calorimeter.	38
6.2	Cartoon showing the photon pointing for a displaced photon.	38
6.3	Electron pointing resolution comparison between data (dotted lines) and simulated samples (solid lines) for $Z \rightarrow ee$ process for various η regions as a function of p_T (left) and as a function of the primary vertex z position (right).	39
6.4	Photon pointing resolution comparison between data (dotted lines) and simulated samples (solid lines) for $Z \rightarrow ll\gamma$ process for various η regions as a function of p_T (left) and as a function of the primary vertex z (right).	39
6.5	Photon pointing resolution comparison between data (squares) and simulated signal samples (circles) for various η regions as a function of photon pointing. The agreement between 0-200 mm for the barrel photons (red and black points) serves as a validation.	40
6.6	Comparison of Loose ID efficiency of the photon as a function of its pointing for different p_T ranges.	42
6.7	Timing resolution for electrons as a function of the E_{cell} energy for medium and high gains.	45
6.8	Timing profiles for electrons (blue) and photons (red) for various samples as a function of cluster energy before the cluster energy correction is applied (left) and after it is applied (right). The timing profiles for photons in the control region (magenta) and validation region (E_T^{miss}) (black) defined in Table 7.2 are also shown here for reference.	45
7.1	Comparison of leading-photon p_T for events corresponding to a luminosity of $0.33 fb^{-1}$ satisfying $ m_{e\gamma} - 91.18 < 15$ GeV in black and events that do not satisfy this requirement in red. The feature at 40 GeV in the black curve is indicative of the electrons faking photons.	47
8.1	Pointing shape normalized to the bin width is compared between the VR(t) or SR $t < 0$ region data and few signal points using 100% Higgs to NLSP branching ratio for high mass splitting or the high- Δm analysis for the 1γ channel (left) and the $\geq 2\gamma$ channel (right).	52

8.2	Pointing shape normalized to the bin width is compared between the VR(t) or SR $t < 0$ region data and few signal points using 100% Higgs to NLSP branching ratio for low mass splitting or low- Δm analysis for the 1γ channel (left) and the $\geq 2\gamma$ channel (right).	54
8.3	E_{cell} distribution for high- Δm VR(t) in red points, CR medium photons in black points, and the ratio of the reweighted CR (medium) timing to the SR ($t < 0$) in blue curve in the bottom panel. Note that the jump in the distribution is due to a change in the bin width.	54
8.4	Real-enhanced (left) and fake-enhanced (right) photon timing distribution before E_{cell} reweighting in green, after E_{cell} reweighting to high- Δm SR in blue and after the residual mean shift in red color for $ z_{ZDCA} < 50$ mm and 1γ channel.	55
8.5	Real-enhanced (left) and fake-enhanced (right) photon timing distribution before E_{cell} reweighting in green, after E_{cell} reweighting to low- Δm SR in blue and after the residual mean shift in red color for $ z_{ZDCA} < 50$ mm and 1γ channel.	55
8.6	Real-enhanced and fake-enhanced photon timing template comparison in different pointing categories in 1γ channel on the left and $\geq 2\gamma$ channel on the right. These templates use $E_{cell} > 10$ GeV and reweighted in E_{cell} to match that of high- Δm SR and templates are shifted by the mean of their timing distribution.	56
8.7	Real-enhanced and fake-enhanced photon timing template comparison in different pointing categories in 1γ channel on the left and $\geq 2\gamma$ channel on the right. These templates use $E_{cell} > 7$ GeV and reweighted in E_{cell} to match that of low- Δm SR and templates are shifted by the mean of their timing distribution.	57
8.8	Distribution of the significance for signal-plus-background fits to the high- Δm VR(t) is shown in the first row for the signal points with lifetime of 2 ns (10 ns) on the left (right). Similar distributions for the low- Δm VR(t) is shown in the second row. A positive significance suggests an excess while a negative significance suggests a deficit.	61
9.1	Plots comparing the high- Δm VR(t) region data (black) against the background-only fit without non-closure uncertainties for the 1γ channel (left) and the $\geq 2\gamma$ channel (right). Ratio of data to each of the background estimation is available in the bottom pane.	66
9.2	Signal yield for (60,0.5,2) signal point in different pointing categories with (red) and without (black) the non-pointing photon identification.	73
9.3	Comparison of pointing shapes for all signal points in the low-pileup (red) and high-pileup (blue) conditions to the nominal full pileup condition (black) in both the 1γ (left) and $\geq 2\gamma$ channel (right).	73
9.4	Nominal timing distribution for signal point (60,0.5,2) in black compared against the up (blue) and down (red) variations for 1γ channel and lowest pointing category.	74

10.1	The data yields in the high- Δm VR(t) region in two dimensions of photon pointing and timing for the 1γ channel (left) and the $\geq 2\gamma$ channel (right) in the first row. Similar plots are available in the second row for the uncertainties on these data yields. The X-axis corresponds to the photon timing and the Y-axis corresponds to the photon pointing.	79
10.2	The signal yields for the (60,0.5,2) signal point in the high- Δm VR(t) region in two dimensions of photon pointing and timing for the 1γ channel (left) and the $\geq 2\gamma$ channel (right). The X-axis corresponds to the photon timing and the Y-axis corresponds to the photon pointing.	80
10.3	Timing distribution for data and background-only fit in the high- Δm VR(t) region for different pointing categories in the 1γ channel (left) and the $\geq 2\gamma$ channel (right).	81
10.4	Comparison of the sum of the timing distribution in 5 pointing categories for data and background-only fits for the 1γ channel (left) and the $\geq 2\gamma$ channel on the right for the high- Δm VR(t) region. Note that the fit is still performed simultaneously in the 10 pointing categories, the sum of the timing distributions shown here are for display purposes only.	82
10.5	Timing distribution for data and background-only fit in the high- Δm VR(t) region for different pointing categories in the 1γ channel (left) and the $\geq 2\gamma$ channel (right).	83
10.6	Comparison of the sum of the timing distribution in 5 pointing categories for data and background-only fits for the 1γ channel (left) and the $\geq 2\gamma$ channel (right) for the low- Δm VR(t) region. Note that the fit is still performed simultaneously in the 10 pointing categories, the sum of the timing distributions shown here are for display purposes only.	84
10.7	Post-fit nuisance parameter pull plots showing the top 25 nuisance parameters with maximum impact on the fitted μ . The left plot corresponds to the high- Δm VR(t) analysis using signal point $(m_{NLSP}, m_{LSP}, \tau) = (60, 0.5, 2)$ and the right plot corresponds to the low- Δm VR(t) analysis using signal point $(m_{NLSP}, m_{LSP}, \tau) = (40, 30, 2)$. The black box corresponds to the pre-fit impact on the μ . The blue band represents post-fit impact on the μ when the Br and NP change in the same direction and green band represents the same when they change in the opposite direction. The black dot is the uncertainty on the NP pull and red band corresponds to its 1σ band.	85
10.8	Comparison for the sum of the timing distribution in 5 pointing categories for data and background-only fits for the 1γ channel (left) and the $\geq 2\gamma$ channel (right) for the high- Δm VR(E_T^{miss}) region. Note that the fit is still performed simultaneously in the 10 pointing categories, the sum of the timing distributions shown here are for display purposes only.	86

- 10.9 Comparison for the sum of the timing distribution in 5 pointing categories for data and background-only fits are compared for the 1γ channel (left) and the $\geq 2\gamma$ channel (right) for the low- Δm VR(E_T^{miss}) region. Note that the fit is still performed simultaneously in the 10 pointing categories, the sum of the timing distributions shown here are for display purposes only. 86
- 10.10 Comparison for the timing distribution for data plus injected signal from the (60,0.5,2) signal point at BR(H \rightarrow NLSP NLSP)=10% (black) against fitted background from signal-plus-background (blue) along with the signal contribution at the injected BR (red) is shown in the last pointing category for the 1γ channel (left) and the $\geq 2\gamma$ channel (right) for the high- Δm VR(E_T^{miss}) region. 87
- 10.11 Difference between the fitted BR(H \rightarrow NLSP NLSP) values from the signal-plus-background fit to data-plus-injected signal to that of the fitted BR(H \rightarrow NLSP NLSP) values for signal-plus-background fits to only the data in VR(t) region at different injected BR(H \rightarrow NLSP NLSP) values for $(m_{NLSP}, m_{LSP}) = (60, 0.5)$ in the top left plot, for (40,20) on the top right plot and (50,40) in the bottom plot. Note that the high- Δm analysis selections are used in the first row while the low- Δm analysis selections are used in the bottom row. Each plot shows the results for both lifetimes of 2 and 10 ns. 88
- 11.1 Timing distributions for the data and the estimated background, as determined by the background-only fit, for the high- Δm selection in different pointing categories for the 1γ ($\geq 2\gamma$) final state on the left (right). For comparison, the expected timing shapes for a few different signal points are superimposed, with a signal normalization corresponding to a value of BR(H \rightarrow NLSP NLSP) = 20%. The signal models are labelled by their values of the NLSP and LSP masses (in GeV) and NLSP lifetime (in ns). 91
- 11.2 Timing distributions for data and the estimated background, as determined by the background-only fit, for the low- Δm selection in different pointing categories for the 1γ ($\geq 2\gamma$) final state on the left (right). For comparison, the expected timing shapes for a few different signal points are shown superimposed, with a signal normalization corresponding to a value of BR(H \rightarrow NLSP NLSP) = 20%. The signal models are labelled by their values of the NLSP and LSP masses (in GeV) and NLSP lifetime (in ns). 92
- 11.3 Post-fit nuisance parameter pull plots showing the top 25 nuisance parameters (NPs) with the maximum impact on the fitted μ using the signal-plus-background fit to the observed data. The left plot corresponds to the high- Δm analysis using signal point $(m_{NLSP}, m_{LSP}, \tau) = (60, 0.5, 2)$ and the right plot corresponds to the low- Δm analysis using signal point $(m_{NLSP}, m_{LSP}, \tau) = (40, 30, 2)$. The black box corresponds to the pre-fit impact on the μ . The blue band represents the post-fit impact on the μ when the μ and NP change in the same direction and green band represents the same when they change in the opposite direction. The black dot is the uncertainty on the NP pull and red band corresponds to its 1σ band. 93

11.4	The 95% CL observed limits on the BR($H \rightarrow \text{NLSP NLSP}$) along with the expected limits in the brackets for different simulated signal points. The X-axis corresponds to the m_{NLSP} and the Y-axis corresponds to the m_{LSP} . The lifetime of the NLSP is 2 ns (10 ns) for the left (right) plot.	94
11.5	The 95% CL observed limits on the BR($H \rightarrow \text{NLSP NLSP}$) for the high- Δm analysis with contours indicating the various observed limits (2, 5 and 10 %) in black along with the corresponding expected limits in grey. The X-axis corresponds to the m_{NLSP} and the Y-axis corresponds to the m_{LSP} . The lifetime of the NLSP is 2 ns (10 ns) for the left (right) plot.	95
11.6	The 95% CL observed limits on the BR($H \rightarrow \text{NLSP NLSP}$) for the low- Δm analysis along with the expected limits. The X-axis corresponds to the m_{NLSP} and note that $m_{\text{LSP}} = m_{\text{NLSP}} - 10$ GeV. The lifetime of the NLSP is 2 ns (10 ns) for the left (right) plot.	96
11.7	The lifetime of the signal point $(m_{\text{NLSP}}, m_{\text{LSP}}, \tau) = (60 \text{ GeV}, 0.5 \text{ GeV}, 10 \text{ ns})$ before reweighting (black), after reweighting (green) and the ideal exponential decay time (red).	97
11.8	Comparison of 0.5 ns, 2 ns, and 5 ns parent lifetime samples reweighted to 0.3 ns target lifetime in each pointing category, for the 1γ channel (left) and the $\geq 2\gamma$ channel (right). The ratio of each reweighted distribution is taken with the reweighted 0.5 ns sample, which is the closest generated sample to the target lifetime. The X-axis corresponds to the various timing bins.	98
11.9	Comparison of 2 ns, 5 ns, 10 ns, and 20 ns parent lifetime samples reweighted to 5 ns target lifetime in each pointing category, for the 1γ channel (left) and the $\geq 2\gamma$ channel (right). The ratio of each reweighted distribution is taken with the 5 ns sample. The X-axis corresponds to the various timing bins.	99
11.10	Comparison of 2 ns, 5 ns, 10 ns, and 20 ns parent lifetime samples reweighted to the 100 ns target lifetime in each pointing category, for the 1γ channel (left) and the $\geq 2\gamma$ channel (right). The ratio of each reweighted distribution is taken with the reweighted 20 ns sample, which is the closest generated sample to the target lifetime.	100
11.11	Interpolated 95% CL limits on BR($H \rightarrow \text{NLSP NLSP}$) as a function of lifetime (X-axis) and m_{LSP} (Y-axis) for fixed $m_{\text{NLSP}} = 60$ GeV (top left), 50 GeV (top right), 40 GeV (bottom left), and 30 GeV (bottom right). Expected (grey) and observed (black) contours for limits are superimposed where possible.	101
11.12	Interpolated 95% CL limits on BR($H \rightarrow \text{NLSP NLSP}$) as a function of lifetime (X-axis) and m_{NLSP} (Y-axis). Different colors correspond to different m_{LSP}	102
11.13	Ratio of the reconstructed yields to the truth yields in the model-independent signal regions in the 1γ and $\geq 2\gamma$ channel for all signal points.	105
A.1	Short-strip module in barrel layer. The other barrel and end-cap modules have same components with different arrangement.	110
A.2	A short-strip module assembled at the Lawrence Berkeley National Laboratory.	111

A.3	Power board version 2 assembled at the Lawrence Berkeley National Laboratory.	111
A.4	Single power board test adapter.	112
A.5	Efficiency curve from the Power board specifications.	113
A.6	Test setup for power cycling test.	116
A.7	Efficiency over time for power cycling. The rise in the efficiency was because no cooling system was in place to dissipate the heat as the load drew around 4.5 W from the power board.	117
A.8	Set up for the long-term test. This includes the mass testing of 9 power boards with one resistor load each and a cooling system.	118
A.9	Current across resistor as a function of time for 3-24 October 2018 run.	119
A.10	Current across resistor as a function of time for 24 October - 12 November 2018 run.	119
A.11	Current across resistor as a function of time for 12 November 2018 - 24 January 2019 run.	120
A.12	Efficiency of the power board as a function of time for 3-24 October 2018 run.	120
A.13	Efficiency of the power board as a function of time for 24 October - 12 November 2018 run.	121
A.14	Efficiency of the power board as a function of time for 12 November 2018 - 24 January 2019 run.	121
A.15	Efficiency as a function of current output by the power board. The power board is most efficient at the lowest temperature and the efficiency drops as the temperature increases.	122
A.16	ADC counts from R1 (output current) channel on AMAC on Y-axis and output current measured from the variable load on X-axis.	123
A.17	PTAT calibration curve with PTAT ADC counts at 0A output current on Y-axis and the climate chamber temperature on X-axis.	124
A.18	Temperature of the FEAST, measured from PTAT, as a function of current drawn from the power board.	125
A.19	NTC temperature as a function of current drawn from the power board.	126
B.1	Sensor corner for silicon sensor shows the active area with individual strip implants including the surrounding bias ring, guard ring and edge ring. The AC pad in the first read-out enabled sensor is shown for reference. The X-ray beam orientations for the surface and head-on scans are also shown here.	128
B.2	Charge collection pattern when Strip 1 is incident with X-ray beams is shown here. The individual strips along with the AC pad positions are highlighted here. The X-axis corresponds to the direction along the strip and the Y-axis corresponds to the direction perpendicular to the strip.	129
B.3	Charge collection pattern when Strip 2 is incident with X-ray beams is shown here. The individual strips along with the AC pad positions are highlighted here. The X-axis corresponds to the direction along the strip and the Y-axis corresponds to the direction perpendicular to the strip.	131

B.4	Charge collection pattern when Strip 1 is incident with X-ray beams is shown here. The individual strips along with the AC pad positions are highlighted here. The X-axis corresponds to the direction along the strip and the Y-axis corresponds to the direction perpendicular to the strip.	131
B.5	Charge collection pattern when Strip 2 is incident with X-ray beams is shown here. The individual strips along with the AC pad positions are highlighted here. The X-axis corresponds to the direction along the strip and the Y-axis corresponds to the direction perpendicular to the strip.	132
B.6	Charge collection pattern in the bulk of the sensor. The X-axis corresponds to the direction across the strip and the Y-axis corresponds to the sensor depth. The individual strips are outlined here for reference. The sensor tilted here due to internal stresses as it is not held down by a vacuum.	133

List of Tables

4.1	Table of masses of the NLSP and LSP particles for simulated samples. Each of these samples was produced with associated $W/Z/t\bar{t}$ processes and simulated at two different lifetimes of 2 and 10 ns.	27
4.2	Table of masses of the NLSP and LSP particles for additional simulated samples. Each of these samples was produced with associated $W/Z/t\bar{t}$ processes and simulated at two different lifetimes of 0.5, 5 and 20 ns.	27
7.1	Table of event preselection criteria for electrons, muons and photons.	46
7.2	Summary of different selections for high-mass splitting and low-mass splitting analysis that includes the selection cuts on E_{cell} , E_T^{miss} , photon pointing and timing bins along with various control, validation and signal regions.	49
7.3	Yields for data in different regions.	50
7.4	Predicted yield for six signal samples which are labelled by $(m_{NLSP}$ GeV, m_{LSP} GeV, τ ns). Note that the yield shown here is normalized to 139 fb^{-1} assuming 20% branching ratio of Higgs decaying to a pair of neutralinos.	50
8.1	KS-test values of the real-enhanced and fake-enhanced timing shape comparisons for timing templates in each pointing category for the high- Δm and low- Δm analysis.	59
9.1	Relative uncertainties for the real-enhanced templates for the high- Δm analysis. Each column corresponds to a timing bin, and each row corresponds to a pointing category.	63
9.2	Relative uncertainties for the fake-enhanced templates for the high- Δm analysis. Each column corresponds to a timing bin, and each row corresponds to a pointing category.	63
9.3	Relative uncertainties for the real-enhanced templates for the low- Δm analysis. Each column corresponds to a timing bin, and each row corresponds to a pointing category.	64
9.4	Relative uncertainties for the fake-enhanced templates for the low- Δm analysis. Each column corresponds to a timing bin, and each row corresponds to a pointing category.	64

9.5	Relative non-closure uncertainties in each timing bin for the high- Δm analysis. Each column corresponds to a timing bin, and each row corresponds to a pointing category.	65
9.6	Relative non-closure uncertainties in each timing bin for the low- Δm analysis. Each column corresponds to a timing bin, and each row corresponds to a pointing category.	67
9.7	PDF variation and scale variation for each production mode at generator level. The total uncertainty on the predicted signal yield in SR for $(m_{NLSP}$ (GeV), m_{LSP} (GeV), τ (ns)) = (60,0.5,2) signal point due to the combined PDF and scale variation are given in the last column. Once these production modes are weighted by their cross section, the impact on the signal yield in SR for 60,0,2 signal point is around 17%.	69
9.8	Up and down experimental uncertainties related to electron, muon, E_T^{miss} , e/γ scale and resolution uncertainties for $(m_{NLSP}, m_{LSP}, \tau) = (60, 0.5, 2)$ in the 1γ and $\geq 2\gamma$ channels.	69
9.9	Up and down experimental uncertainties for various signal points in the 1γ and $\geq 2\gamma$ channel.	70
9.10	Relative uncertainty on the signal yield due to prompt photon identification scale factor in the 1γ and $\geq 2\gamma$ channel for different signal points.	71
10.1	Description of different nuisance parameters and the notations used for these in the pull plots where px defines the pointing category where p0: $0 < z_{DCA} < 50$ mm, p1: $50 < z_{DCA} < 100$ mm, p2: $100 < z_{DCA} < 200$ mm, p3: $200 < z_{DCA} < 300$ mm, p4: $300 < z_{DCA} < 2000$ mm. The photon channel is given by cy where c0: 1γ channel and c1: $\geq 2\gamma$ channel. Timing bin is denoted by ty and for the 1γ channel, it ranges from 0-6 where t0: $0 < t < 0.2$ ns, t1: $0.2 < t < 0.4$ ns, t2: $0.4 < t < 0.6$ ns, t3: $0.6 < t < 0.8$ ns, t4: $0.8 < t < 1$ ns, t5: $1.0 < t < 1.5$ ns and t6: $1.5 < t < 12$ ns. Similarly, the timing bins for the $\geq 2\gamma$ channel range from 0-5 where t0: $0 < t < 0.2$ ns, t1: $0.2 < t < 0.4$ ns, t2: $0.4 < t < 0.6$ ns, t3: $0.6 < t < 0.8$ ns, t4: $0.8 < t < 1$ ns, t5: $1.0 < t < 12$ ns.	76
11.1	The measured purity values for the real-enhanced and fake-enhanced timing templates in the fit to the observed data for the high- Δm analysis using the background-only fit for the ten different pointing categories.	89
11.2	The measured purity values for the real-enhanced and fake-enhanced timing templates in the fit to the observed data for the low- Δm analysis using background-only fit for the ten different pointing categories.	90
11.3	Table of common event preselection criteria at the truth level for analysis regions.	102
11.4	Comparison of event yields for 60,0.5,2 signal point at different stages of reconstructed level selections against the selections at truth level. The truth acceptance and the efficiency is also included here.	103

11.5	Signal yields at truth level, acceptance and efficiency in the 1γ and $\geq 2\gamma$ model-independent regions.	104
11.6	Model-independent limits using the last timing bin in the highest pointing category for the 1γ and $\geq 2\gamma$ channels separately. Limits for the combination of these two channels is presented in the last column. The table also includes the observed number of events N_{data} , background estimation N_{bkg} and the systematic uncertainty of the estimated background, N_{bkg} error.	106

Acknowledgments

First and foremost, I would like to thank my family for their unwavering love, support and confidence. I consider myself blessed for having such loving parents who have always instilled the importance of education and independence. Thanks to my sister who shaped me into the person I am today, more than she knows, and for being my role model. Thanks to Hrishu for the constant love, laughter and encouragement along with all the fun science questions you ask!

This thesis work would not have been possible without the continuous support and mentoring from Marjorie. You are the mentor and researcher I aspire to become one day. Special thanks to Haichen for guiding me to perform research day to day and always pushing me to my full potential. I would also like to thank Timon for guiding me through the qualification task and teaching me all I know about detector R&D. Thanks to all my colleagues within the ATLAS collaboration who made this thesis work possible.

I would like to extend my gratitude to all the teachers and mentors who encouraged me to pursue my dreams and helped me become the person I am today. I would like to express my thanks to Sourabh for introducing me to experimental particle physics and guiding me through my Master's thesis.

Special thanks to all my colleagues from the LBNL ATLAS group who encouraged me to become a better researcher. Thanks to Best, Tom, Byeonghee, Sam, Patrick, Greg, Cesar, Charilou and countless others for making graduate school fun and enriching experience. Thanks to Pulastya, Shubhanshu and Supraja for being my friends I can call up no matter where we are in the world.

Chapter 1

Introduction

This thesis describes a search for displaced photons using the ATLAS detector at the Large Hadron Collider [1]. This chapter provides the introduction and the signal model for this search is described in Chapter 2 followed by the description of the ATLAS detector in Chapter 3. The data and simulated samples used for this study are presented in Chapter 4. The particle reconstruction in Chapter 5. The photon pointing and timing variables are described in Chapter 6. The different selections imposed on the events are summarized in Chapter 7. The estimation of the SM background in this analysis is given in Chapter 8 followed by the description of various systematic uncertainties in Chapter 9. The statistical interpretation for the study is described in Chapter 10 and the results for this search are presented in Chapter 11 followed by summary in Chapter 12. Additional work on the High Luminosity-Large Hadron Collider upgrade of the ATLAS detector performed by the author of this thesis is summarized in Appendices A-B.

This chapter introduces the Standard Model of particle physics which provides the best description of fundamental particles and their interactions. This is followed by a discussion on the limitations of the Standard Model motivating the search for beyond Standard Model (BSM) theories. A brief discussion on supersymmetry theory is also presented in this chapter.

1.1 Standard model of particle physics

The Standard Model of particle physics (SM) [2] has been tremendously successful in accounting for most of the experimental phenomena and rightly predicted the existence of top quark, tau neutrino, W, Z and the Higgs boson. This theory includes fundamental particles and gives a prescription for their interactions. The electroweak theory in the SM was proposed by Glashow, Weinberg, and Salam describing the fundamental particles and their interactions [3][4][5]. Glashow proposed a unified theory of electromagnetic and weak interactions in 1961 and Weinberg and Salam included the Higgs mechanism into Glashow's electroweak unified theory. The strong interaction was added to this prescription in early 1970s thus completing the modern form of the Standard Model of particle physics [6]. Its

gauge theory can be described by the symmetry group $SU(3)_C \times SU(2)_L \times U(1)_Y$. The fourth fundamental force, gravity, is not included in the theory.

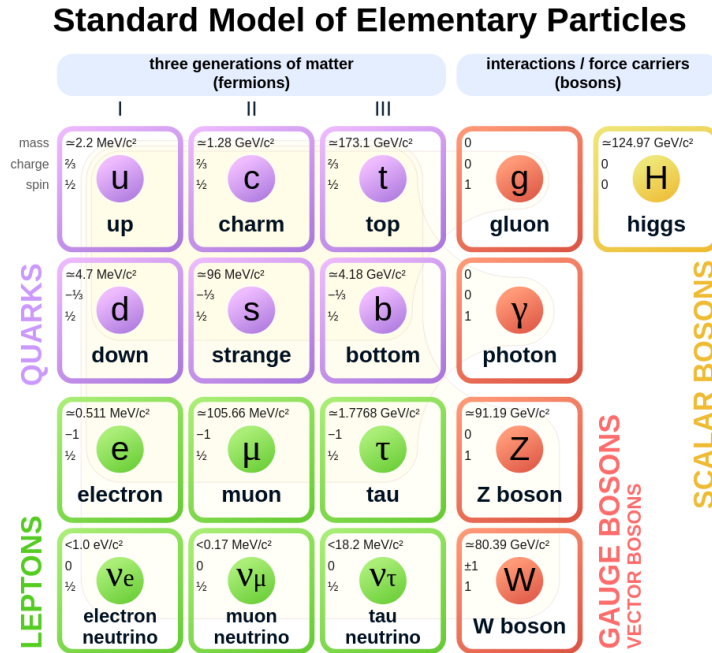


Figure 1.1: Particle content of the Standard Model [7].

1.1.1 Particle content of SM

The particle content of the Standard Model is summarized in Figure 1.1 and contains 61 fundamental particles. The matter particles include quarks and leptons, each with spin $\frac{1}{2}$, and come in three generations. Each fermion in the Standard Model has its own antiparticle. The leptons participate only through electroweak interaction while the quarks also interact through the strong interaction. There are three charged leptons: electron (e), muon (μ) and tau (τ) and three neutral neutrinos (ν_e, ν_μ, ν_τ). The charged leptons are massive and the neutrinos are massless in the Standard Model. There are a total of 12 leptons including the anti-particles. There are six types of quarks: up, down, charm, strange, top and bottom. The electric charge and mass of each of these is shown in Figure 1.1 for reference. In addition to the electric charge, a quark also carries a color charge that facilitates the strong interaction and there can be three colors that a quark can have. In total, there are 36 quarks including all the flavors and their anti-particles. The 12 vector bosons in the Standard Model are the force carriers with the photons, W^\pm and Z bosons mediate the electroweak force while the

8 types of gluons mediate the strong force. The Higgs boson, a scalar, arises due to the spontaneous symmetry breaking of the electroweak interaction and is responsible for masses of the fermions and bosons in the Standard Model. With the discovery of the Higgs boson in 2012 by the ATLAS and CMS collaborations[8][9], all the 61 fundamental particles proposed by the theory have now been observed in nature and their precise properties are continuously studied at particle collisions at high energies.

1.1.2 Strong interaction

The strong interaction is described by Quantum Chromodynamics (QCD) which is an $SU(3)_C$ gauge theory describing quarks and gluons, and their interactions. The Lagrangian of QCD is given by

$$\mathcal{L}_{QCD} = \sum_q \bar{\psi}_{q,a} (i\gamma^\mu \partial_\mu \delta_{ab} - g_s \gamma^\mu t_{ab}^C A_\mu^C - m_q \delta_{ab}) \psi_{q,b} - \frac{1}{4} F_{\mu\nu}^A F^{A\mu\nu} \quad (1.1)$$

where the summation is over different quark flavors q , $\psi_{q,a}$ are quark-field spinors, m_q is the mass of the quarks, γ^μ are the Dirac γ -matrices, A_μ^C are gluon fields with C iterating over the 8 gluons. t_{ab}^C refers to the eight generators of the $SU(3)$ group. This term is responsible for quarks changing color charge upon interaction with a gluon. Here, g_s corresponds to the strong interaction coupling constant and the $F_{\mu\nu}^A$ corresponds to the field tensor.

Quarks and gluons are not observed as free particles [2]. The color-singlet combinations of quarks and gluons, called hadrons, are experimentally observed. Protons and neutrons are examples of such hadrons.

In proton-proton collisions, the partons (quarks and gluons) within the incoming protons participate in the hard scatter interaction. The remaining partons interact with each other resulting in lower energy hadronic activity known as the underlying event. An example Feynman diagram of the proton-proton collision event is shown in Figure 1.2. The partons in the incoming protons and their momenta are described by parton distribution functions (PDFs). The complete proton-proton cross section is given by convoluting the hard scatter cross section calculated at the parton level with the PDFs for the incoming partons. The cross section of the hard scatter interaction is calculated to a fixed order in perturbation theory. The cross section depends on the factorization scale which separates the perturbative and non-perturbative regimes in QCD. Above the factorization scale, strong coupling is small to allow the cross section to be calculated at fixed order using perturbation theory. This scale is typically chosen to be around the momentum transfer in the interaction. The running of the strong coupling depends on a renormalization scale which is also set around the momentum transfer.

1.1.3 Electroweak interaction and spontaneous symmetry breaking

The Lagrangian for the electroweak theory before symmetry breaking can be written as

$$\mathcal{L}_{EW} = -\frac{1}{4}W_a^{\mu\nu}W_{\mu\nu}^a - \frac{1}{4}B^{\mu\nu}B_{\mu\nu} + \mathcal{L}_f + \mathcal{L}_h + \mathcal{L}_y \quad (1.2)$$

where the first two terms describe the interactions between $W^{a\mu\nu}$ for $a=1,2,3$ and $B^{\mu\nu}$ vector bosons which are the field strength tensors for the weak isospin and hypercharge gauge fields. The third term, \mathcal{L}_f describes the kinetic term for the SM fermions that include the interaction of gauge bosons and fermions. The next term, \mathcal{L}_h , describes the Higgs field and its interactions with gauge bosons and the last term, \mathcal{L}_y , refers to the Yukawa interactions of the fermions.

The Higgs mechanism describes the spontaneous symmetry breaking of the electroweak unification and is responsible for generating masses of the particles in the SM. The scalar potential of the Higgs field is given by

$$V(\phi) = \mu^2\phi^2 + \lambda\phi^4 \quad (1.3)$$

where ϕ is the Higgs field which is an $SU(2)_L$ complex doublet with four degrees of freedom.

The corresponding Lagrangian is given by

$$\mathcal{L}_H = (D_\mu\phi)^*(D^\mu\phi) - \mu^2\phi^2 - \lambda\phi^4 \quad (1.4)$$

The first term represents the kinetic energy of the scalar particle, the second term represents the mass of the particle and the third term corresponds to the self interaction of the scalar field. When μ is real and $\mu^2 < 0$, the minima of the potential is non-zero and the resulting scalar field has non-zero vacuum expectation value v given by:

$$\phi = \pm v = \pm \left| \sqrt{\frac{-\mu^2}{\lambda}} \right| \quad (1.5)$$

The choice of the vacuum state between $+v$ and $-v$ is referred to as the process of spontaneous symmetry breaking as this breaks the symmetry of the Lagrangian. This symmetry breaking indicates the existence of three massless Goldstone bosons. The Higgs field couples to the gauge fields W_μ and B_μ from the electroweak theory and results in the longitudinal components of the Z and W bosons that are measured experimentally. These bosons acquire mass through this interaction. The fourth remaining degree of freedom of the Higgs field results in the physical Higgs boson. The photon however remains massless as it corresponds to the conserved $U(1)_{em}$ gauge symmetry. Similarly, the gluons associated with the conserved $SU(3)_C$ symmetry group also remains massless. The fermions acquire their mass in the SM through interactions with the Higgs field.

1.2 Limitations of the Standard Model

The SM, however successful, is not a complete theory of particle physics as it doesn't account for certain experimental observations and phenomena. The neutrino oscillation phenomenon was experimentally observed establishing that at least two neutrinos are massive [10][11]. The neutrinos in the Standard Model are massless and unable to account for this observation. The evidence from the galaxy rotation curves establishes the existence of dark matter in the universe [12] and there is no dark-matter candidate in the SM. The observed universe is composed mainly of matter rather than anti-matter and this visible matter-antimatter asymmetry is also not explained in the SM. In addition, gravitational interaction is not included in the theory.

The Standard Model also doesn't provide an explanation to the hierarchy problem. The Higgs mass in the SM gets corrections from all the fermions and bosons that interact with it. For example, the top loop contributes a correction to Higgs mass proportional to a product of coupling and $|\Lambda_{UV}|^2$ scale where $|\Lambda_{UV}|$ is the energy scale at which new physics matters. If there is no beyond Standard Model (BSM) theory at lower energy than the Planck scale, then the Higgs mass gets a contribution of 30 orders in magnitude from this interaction. The bosons give a similar contribution but with a negative sign. These many orders of magnitude in corrections can be suppressed if these loops are made to cancel each other very precisely. If there is in fact new physics then the corrections to the mass terms depend on its energy scale and also the mass spectrum of its particles. To allow exact cancellations, the couplings need to be tuned. This fine tuning of parameters to obtain the observed finite mass of the Higgs boson around 125 GeV is what is referred to as the hierarchy problem and the SM doesn't provide a good explanation for this.

There are many BSM theories that resolve one or more of these inadequacies. One such class of BSM models is Supersymmetry (SUSY) [13] which provides a good explanation for the hierarchy problem. Some SUSY theories also provide a viable dark matter candidate. The next section introduces the supersymmetry theory briefly.

1.3 Supersymmetry

SUSY introduces a new fundamental symmetry between fermions and bosons [14]. Each SM fermion now gets a supersymmetric boson partner and each SM boson gets a supersymmetric fermion partner. Each of the SM particles and their superpartners form a supermultiplet and have same mass, other quantum numbers under $SU(3)_C \times SU(2)_L \times U(1)_Y$ symmetry group and number of degrees of freedom [15].

1.3.1 Particle content

The smallest possible particle content of the SUSY models is described in the context of the Minimal Supersymmetric Standard Model (MSSM) [16]. The notation used here follows

the reference [17]. The left-handed leptons in the SM form $SU(2)_L$ doublets:

$$\begin{pmatrix} \nu_{eL} \\ e_L \end{pmatrix}$$

and its superpartners form an equivalent doublet of spin-0 particles:

$$\begin{pmatrix} \tilde{\nu}_{eL} \\ \tilde{e}_L \end{pmatrix}$$

where the $\tilde{\nu}$ is a scalar partner of neutrino called sneutrino and the \tilde{e} refers to the scalar partner of the electron called the selectron. Analogous to this, there are smuons, staus and sneutrinos $\tilde{\nu}_{\mu L}$ and $\tilde{\nu}_{\tau L}$. Similarly, the left-handed quarks in the SM form the $SU(2)_L$ doublets

$$\begin{pmatrix} u_L \\ d_L \end{pmatrix}$$

and its superpartners form an equivalent doublet containing

$$\begin{pmatrix} \tilde{u}_L \\ \tilde{d}_L \end{pmatrix}$$

The right-handed fermions in the SM are singlets under $SU(2)_L$ and so are their scalar right-handed superpartners.

The gluons in the SM are singlets under $SU(3)$ symmetry and their superpartners called the gluinos (\tilde{g}) form a new octet of $SU(3)$ fermions. Similarly, the superpartners of the electroweak force carriers from the SM are a part of $SU(2)_L$ triplet of fermions called winos ($\tilde{W}^\pm, \tilde{W}^0$) and a $U(1)$ bino (\tilde{B}).

The scalar Higgs field in the SM has an equivalent fermionic superpartners, higgsinos, that form chiral supermultiplets. There are two independent Higgs chiral supermultiplets one which interacts with up-type quarks and another that interacts with the down-type quarks and the charged leptons:

$$H_u : \begin{pmatrix} H_u^+ \\ H_u^0 \end{pmatrix}, \begin{pmatrix} \tilde{H}_u^+ \\ \tilde{H}_u^0 \end{pmatrix}$$

and

$$H_d : \begin{pmatrix} H_d^0 \\ H_d^- \end{pmatrix}, \begin{pmatrix} \tilde{H}_d^0 \\ \tilde{H}_d^- \end{pmatrix}$$

where the superpartners with tildes have spin 1/2. The higgsinos, winos and binos can mix so that the physics states are combinations of these.

1.3.2 R-parity

Supersymmetry introduces many new particles and interactions; an additional symmetry, R-parity, is necessary to ensure that Baryon number (B) and Lepton number (L) violating terms in the Lagrangian are small enough that they have not been measured. This is important to avoid consequences like proton decay [18]. The R-parity symmetry of a particle is defined as:

$$P_R = (-1)^{3(B-L)+2s}$$

where s is the spin of the particle. The SM particles have even R-parity with $P_R = +1$ and their SUSY partners have odd R-parity with $P_R = -1$. There are three important phenomenological consequences of R-parity conservation. The first consequence is that the lightest supersymmetric particle (LSP) is absolutely stable. Given this, the LSP can be a viable dark-matter candidate. The second consequence is that each SUSY particle with mass higher than the LSP decays into odd number of SUSY particles. The third consequence of the R-parity conservation is that the SUSY particles are always produced in pairs in collisions and decays of SM particles.

1.3.3 SUSY breaking and mass eigenstates

Note that if SUSY exists in nature, it needs to be broken. If not, there would be SUSY particles with same mass as their SM counterparts differing in spin. For example, there would be a scalar stop particle \tilde{t} with mass around the top quark mass of 173 GeV and it would have been discovered experimentally. Given the absence of evidence for all SUSY particles at the same mass as their superpartners, the supersymmetry is a broken symmetry and there are multiple mechanisms to achieve this in different SUSY models.

In soft SUSY breaking, the SUSY Lagrangian is decomposed into two parts, one consists of the gauge, Yukawa, and dimensionless scalar couplings, and this part preserves exact SUSY while the other contains only mass terms and couplings with positive mass dimension which violate SUSY. Such soft SUSY breaking decouples SUSY breaking from its phenomenological consequences and ensures that there are no quadratic divergences to SM particles' masses. Note that once SUSY is broken, the corrections to the Higgs boson mass, Δm_H are of the order

$$\Delta m_H^2 = m_{soft}^2 \left[\frac{\lambda}{16\pi^2} \ln \left(\frac{\Lambda_{UV}}{m_{soft}} \right) + \dots \right] \quad (1.6)$$

where m_{soft} is the largest mass scale in the SUSY violating part of the Lagrangian, λ represents dimensionless couplings and the Λ_{UV} refers to the Planck scale. To ensure that the Higgs mass is finite and SUSY still provides a solution to the hierarchy problem, the m_{soft} needs to be around the electroweak breaking scale, around 174 GeV. In Gauge Mediated Supersymmetry Breaking (GMSB) models, the SUSY breaking happens in some hidden sector, this is mediated by messengers, the Standard Model gauge interactions, to the remaining SUSY sector in which the SUSY breaking scale is around 10-100 TeV [19].

Given that SUSY is a broken symmetry, its particle content described earlier may not be their observable mass eigenstates. Analogous to the consequences of the electroweak symmetry breaking in the SM, after the symmetry breaking and the mixing of the higgsino gauge eigenstates, five higgsino mass eigenstates are produced. Two of these are CP-even and neutral, h^0 and H^0 , one is CP-odd and neutral, A^0 , and two are charged H^\pm . The higgsinos, winos and binos mix together to produce four neutralinos ($\tilde{\chi}_1^0, \tilde{\chi}_2^0, \tilde{\chi}_3^0, \tilde{\chi}_4^0$), two oppositely charged chargino pairs ($\tilde{\chi}_1^\pm, \tilde{\chi}_2^\pm$). The gluinos have identical gauge and mass eigenstates. The squarks and slepton sectors also mix, resulting in different mass eigenstates for the third generation particles compared to their gauge eigenstates while the mixing is negligible for the first and second generation.

1.3.4 GMSB SUSY model

Given the many particles, couplings and interactions introduced by SUSY, some of its models can have more than 100 parameters making this a complex theory. The GMSB SUSY models have a very interesting and simpler phenomenology [14]. The mass spectrum of all the SUSY particles can be predicted in terms of a few fundamental parameters. Another common feature of this set of models is that the gravitino, \tilde{G} , is the LSP and it is stable given the R-parity conservation. Given that it only interacts through gravity, if produced in a proton-proton collision event, it would fly through the detector without any interaction. The next-to-lightest supersymmetric particle (NLSP) typically is the lightest neutralino $\tilde{\chi}_1^0$. The NLSP has to decay into LSP and a SM particle respecting the R-parity symmetry. Given the NLSP is produced from mixing of wino, bino and Higgsino components, its SM decay particle can be the neutral γ , Z bosons. In certain scenarios, the NLSP can have a non-zero lifetime if the coupling between the NLSP and LSP is small.

Note that most of the GMSB phenomenology is driven by the properties of the NLSP and LSP particles. For this thesis, a GMSB signal model is considered where the parameters of interest are the mass, lifetime of NLSP and the mass of LSP. One advantage of using this simplified model is that the results presented here can be interpreted for a wide variety of models where the other SUSY particles can have very different properties. This can also be used to interpret results for non-SUSY signal models that have similar phenomenology. The particular signal model used in this thesis is described in detail in Chapter 2.

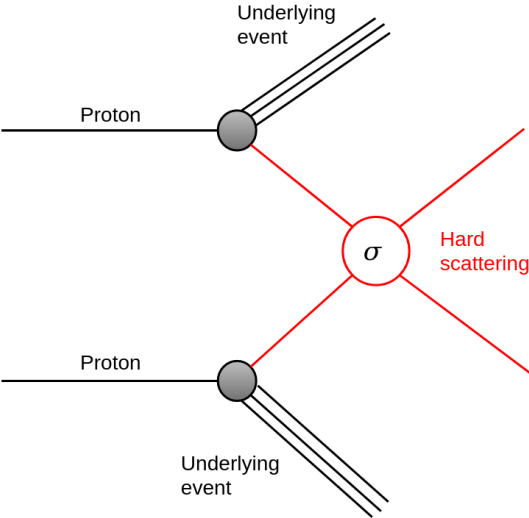


Figure 1.2: Feynman diagram of an example proton-proton collision event. The hard scatter interaction with cross section σ is shown here along with the underlying event.

Chapter 2

Signal model and phenomenology

The ATLAS and CMS collaborations have searched for Supersymmetry in a myriad of ways but have not found any evidence for it [20]. In models where SUSY particles have non-zero lifetimes, new experimental signatures exist that are not constrained in searches for prompt production. This thesis searches for one such signature featuring exotic decay of the standard model Higgs boson into a pair of long-lived SUSY particles. This is well motivated given that the best constraints on the $\text{BR}(H \rightarrow \text{undetected})$ particles is around 21% leaving room for such a signature to exist in nature [21].

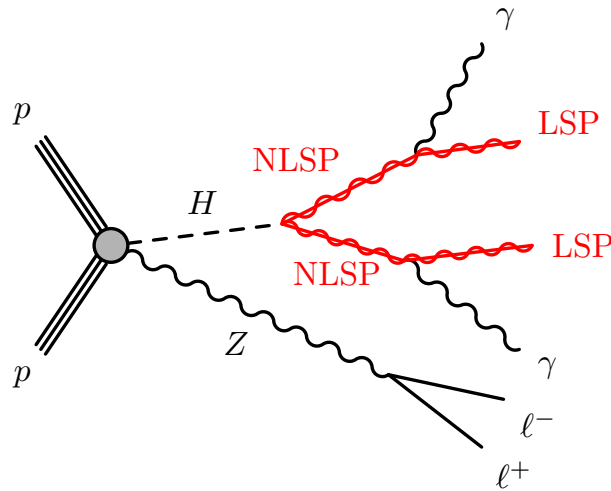


Figure 2.1: Example Feynman diagram for the exotic decay of the Higgs boson produced in association with a Z boson. The Higgs boson decays into a pair of long-lived particles (NLSPs) which each decay into a photon and a stable LSP. The Z boson decays into leptons which are used to trigger the event.

In this signal model, the Higgs boson decays into a pair of long-lived NLSP particles which each decay into a photon and a stable LSP. In the GMSB models, the NLSP typically is a neutralino ($\tilde{\chi}_1^0$) while the LSP is the Gravitino (\tilde{G}). The phenomenology of this signal is driven by three parameters: mass of the NLSP particle (m_{NLSP}), mass of the LSP particle (m_{LSP}) and the lifetime of the NLSP particle (τ). Note that the branching ratio of the NLSP decay into a photon and a LSP is assumed to be 100%. The Higgs boson is produced in association with a W or a Z boson or a $t\bar{t}$ process. The leptons produced from this associated process decay is used to trigger on these events. An example Feynman diagram showing this decay with the associated production of the Z boson is shown in Figure 2.1. Such a signature has never been explored before, making this an important and relevant analysis.

In these models, the long-lived NSPs are produced promptly (at the collisions point) and travel a certain distance and then decay into photons resulting in displaced photons. The direction of flight of such photons, calculated using the ATLAS electromagnetic calorimeter, will not point back to the interaction point when extrapolated to the beam pipe, making them non-pointing photons. These signal photons also arrive later at the electromagnetic calorimeter compared to the prompt photons produced at the primary vertex making them delayed photons. This unique signature of the non-pointing and delayed nature of the signal photons are utilized to search for it.

Note that the ATLAS collaboration has searched for a prompt version of this signature where the NLSP has zero lifetime and no significant excess was found beyond the standard model expectation [22]. The prompt version of the analysis only explored the two dimensional phase space given by m_{NLSP} and m_{LSP} while this thesis explores an additional dimension of the lifetime of the NLSP particle τ .

2.1 Status of displaced photon searches

Although this particular signature involving non-pointing and delayed photons has not been searched before, the ATLAS and CMS collaborations have searched for displaced photons with very high energies in the context of another GMSB signal model. The ATLAS collaboration searched for high-energy delayed photons using proton-proton collisions at center-of-mass energy of 7 TeV and found the data agreed with the background expectation [23]. This signal model was explored again using the non-pointing and delayed photons using collisions at center-of-mass energy of 8 TeV and no excess was found [24]. The CMS collaboration performed this search again using collisions at center-of-mass energy of 13 TeV without seeing an evidence for the signal [25].

The signal model probed in this thesis is completely different in model phenomenology compared to these earlier searches. The key difference is in the photon kinematics resulting from the exotic decays of the Higgs boson. The photons used here typically have energies around 15-30 GeV while the earlier displaced photon searches involved photons at much higher energies. This presents unique challenges to understand the photon identification, pointing and timing performance at low energies, making this a novel project.

Chapter 3

ATLAS experiment

The Large Hadron Collider (LHC) is a state-of-the art proton-proton collider located at CERN in Geneva, Switzerland. The ATLAS detector is one of the multipurpose detectors located at the LHC for studying various aspects of particle physics using data from these collisions. This chapter summarizes the LHC in the first section, the ATLAS detector along with its various sub-detector systems and triggers used to record the data are described in the second section.

3.1 The Large Hadron Collider

The Large Hadron Collider (LHC) is a high-energy particle accelerator with a circumference of 27 km [26] [27] . It is located at CERN on the border between Switzerland and France. The CERN accelerator complex is shown in Figure 3.1 [28] and LHC is the last stage of proton acceleration. The protons are produced by ionizing hydrogen atoms using an electric field. The linear accelerator, Linac 2, accelerates the protons to 50 MeV before entering the Proton Synchrotron Booster (BOOSTER) where they are accelerated to 25 GeV. The protons are then injected into the Super Proton Synchrotron (SPS) which accelerates them to 450 GeV. These energetic protons enter LHC where they are accelerated to the final energy of the order of several TeV.

LHC accelerates protons to the desired energy in bunches separated by 50 ns during Run-1 and 25 ns during Run-2 operations using Radio Frequency cavities. Superconducting dipole magnets bend the proton beams to keep them in a circular path while quadrupole magnets keep the beam focused. LHC is composed of two beam pipes that circulate proton beams in the opposite directions of the collider and these beams pass through the same twin-bore magnets. The two beams are separated from each other in the entire collider except at the four interaction points where the protons collide. The interactions are observed by different particle detectors, ATLAS [29], CMS [30], LHCb[31] and ALICE[32], one at each location.

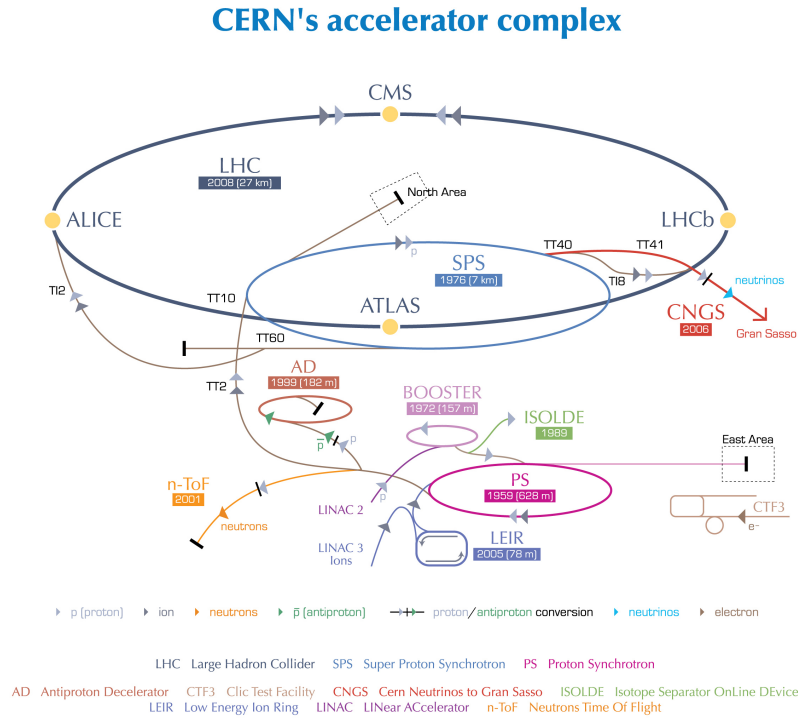


Figure 3.1: Layout of the CERN accelerator complex [28].

Luminosity The expected number of events per second at the LHC is proportional to the cross section for the event (σ_e) and the proportionality constant is the machine instantaneous luminosity, \mathcal{L} . The relation can be written as

$$\frac{dN}{dt} = \sigma_e \mathcal{L} \quad (3.1)$$

The instantaneous luminosity of two beams with Gaussian profiles colliding head-on is given by

$$\mathcal{L} = \frac{N^2 N_b f}{4\pi \sigma_x \sigma_y} \quad (3.2)$$

where N is the number of protons per bunch, N_b is the number of bunches, f is the revolution frequency, and σ_x and σ_y correspond to the beam resolutions in the transverse plane of the beam [33]. At the interaction point of the LHC, the beams are not head-on and have a crossing angle of $O(100 \mu\text{rad})$; additional corrections are applied to correct for this effect.

The total luminosity delivered by the LHC during time T is given by

$$\mathcal{L}_{int} = \int_0^T \mathcal{L} dt \quad (3.3)$$

The ATLAS detector measured the delivered luminosity using LUCID-2 detectors during Run-2 (LUCID detector during Run-1). These detectors are located on the beam pipe on either side of the ATLAS detector [34].

LHC had two successful proton-proton collider runs so far and the third run began in early 2022. During Run-1 of LHC between 2009 and 2012, protons were collided at center-of-mass energy of 7 and 8 TeV delivering total integrated luminosity of 5.5 fb^{-1} [35] and 23 fb^{-1} [36] of data respectively. During Run-2 of LHC between 2015-2018, protons were collided at a higher center-of-mass energy of 13 TeV, delivering total integrated luminosity of 156 fb^{-1} [37] of data. This year (2022) marks the beginning of Run-3 at an even higher center-of-mass energy of 13.6 TeV.

3.2 The ATLAS detector

The ATLAS detector is the largest multipurpose particle detector located at the LHC. The detector is 46 m long, 25 m in diameter, weighs more than 6000 tons and is located 100 m underground. The ATLAS collaboration's physics interests are broad and include discovery of the Higgs boson, precision measurements of Standard Model of particle physics and search for a wide range of BSM phenomena. The detector design is cylindrical, hermetic, layered and consists of many sub-detector subsystems to enable particle detection and reconstruction for a wide variety of particles and energies.

ATLAS coordinate system ATLAS uses a right-handed coordinate system with origin at the proton-proton collision point with the X-axis pointing to the center of the LHC tunnel, Y-axis points vertically upwards and Z-axis is along the tunnel. The radius, r , is defined as the distance in the X-Y plane from the origin. The azimuthal angle, ϕ , is defined around the Z-axis and the ATLAS detector is symmetric in ϕ . The polar angle, θ , is defined as the angle from the Z-axis. Pseudo-rapidity, η , defined as $\eta = -\ln \tan(\theta/2)$, is more convenient to use instead of the polar angle.

Figure 3.2 shows a detailed diagram of the ATLAS detector including different sub-detectors [38]. The ATLAS detector comprises of four main sub-detector systems: Inner Detector, Electromagnetic Calorimeter, Hadronic Calorimeter and Muon Spectrometer. Each of these systems is described in the following sections.

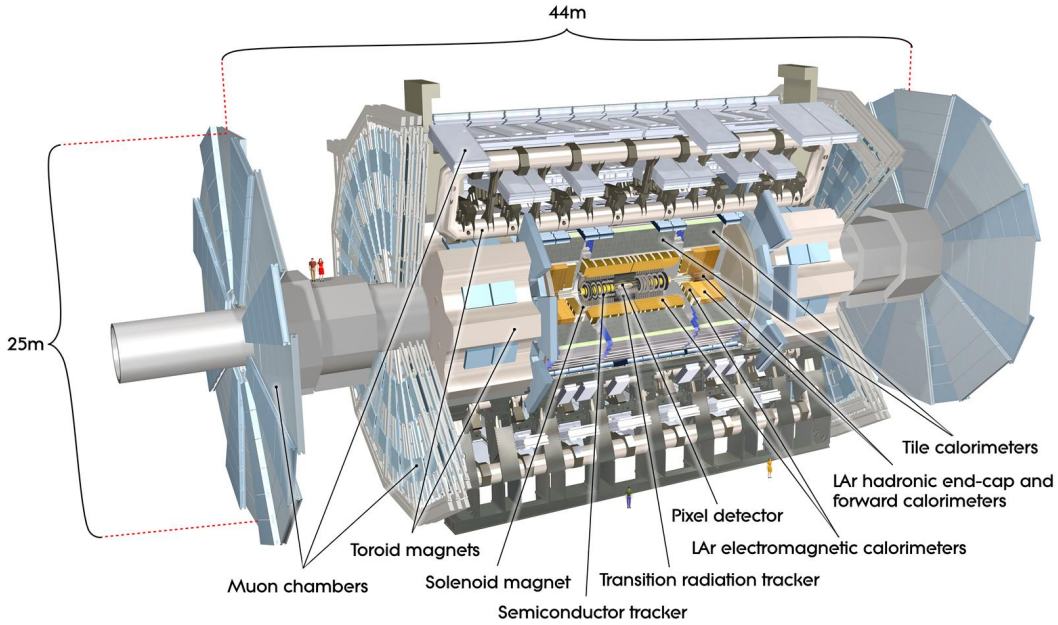


Figure 3.2: Diagram of the ATLAS detector including different sub-detector systems [38].

3.2.1 Inner detector

The ATLAS inner detector [39] is the first sub-detector system from the proton-proton collision point and provides charged-particle tracking at high efficiency. It is composed of four components: Insertable B -Layer (IBL), Pixel detector, Semiconductor Tracker (SCT) detector and Transition Radiation Tracker (TRT). These subdetector systems are enclosed in a solenoidal magnetic field with a central field of 2 T. The resulting curvature of the charged-particle tracks as they traverse through the inner detector provides their momentum information up to $|\eta| < 2.5$. The layout of the ATLAS inner detector (before adding IBL) is available in Figure 3.3.

Insertable B -Layer (IBL) The IBL [40] is the first layer of detector system located at a radius of $r = 3.3$ cm. This layer is composed of radiation-hard, highly granular semiconductor pixel detectors made out of silicon sensors (with pixel size of $50 \times 250 \mu\text{m}^2$). The silicon detectors measure the ionization energy deposited by the charged particles that pass through the sensors. The IBL was added to the ATLAS detector between Run-1 and Run-2 and is now considered as part of the pixel detector system. The IBL, as the name suggests, was added to improve the b-tagging efficiency (b tagging refers to the probability of identifying a jet resulting from b-quark hadronization and relies on the reconstruction of secondary

vertices resulting from B-hadron decays). Given the proximity to the collision point, IBL improves vertexing and the tracking performance and robustness.

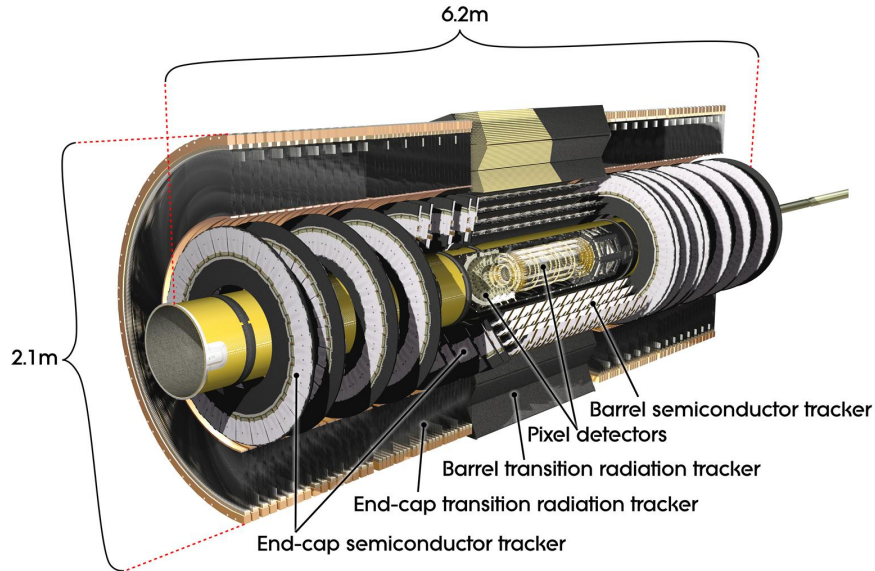


Figure 3.3: Layout of the ATLAS Inner Detector [41].

Pixel detector The ATLAS pixel detector [42], like the IBL, is made of semiconductor pixel detectors (with pixel size $50 \times 400 \mu\text{m}^2$). The pixel detector is composed of 3 barrel layers (*B*-Layer, Layer 1 and Layer 2) between radii of 5 and 12 cm, and two endcaps with three disks on each side, between radii of 11 and 20 cm. The number of layers and their position is optimized to ensure high tracking performance and low material budget. Barrel pixel layers contain 1456 modules and the endcap is composed of 288 disk modules. Each module has 46,080 pixels and the entire barrel detector has approximately 67 million pixels while the endcap detector has 13 million pixels.

Semiconductor Tracker (SCT) Semiconductor Tracker [43] is made of silicon strip sensors (barrel has strip pitch of $80 \mu\text{m}$ and the endcap has a strip pitch ranging from 57 to $94 \mu\text{m}$). It is composed of four cylindrical barrel layers and two endcaps consisting of nine disks on each side. SCT is 5.6 m long with inner radius of 27 cm and outer radius of 56 cm. Each SCT layer is made out of modules which have 1536 channels, each. The barrel region has 2112 modules and the endcap has 1976 modules and has around 6 million channels.

Transition Radiation Tracker (TRT) Transition Radiation Tracker [44] is made out of straw drift tubes with 4 mm diameter filled with Xenon and Argon gas with a 0.03 mm diameter gold-plated tungsten wire cathode in the center. The TRT measures transition-radiation photons and provides discrimination between electrons and pions. Barrel region consists of 50000 straws and each straw is 144 cm long and aligned parallel to the beam axis. The endcap region has 250000 straws and each straw is 39 cm long and positioned radially from the z axis. In total, the TRT contains 350,000 read-out channels.

3.2.2 Calorimeters

The ATLAS calorimeters surround the Inner Detector and are designed to measure the energy of the particles and stop most of the incoming particles. The ATLAS calorimeters are sampling calorimeters with a heavy material as an absorber, which interacts with the particles and creates a particle shower, and an active material where the energy of the shower is sampled and measured. The calorimeter is composed of two subdetector systems: Electromagnetic Calorimeter (ECAL) and Hadronic Calorimeter (HCAL). The layout of calorimeter system is given in Figure 3.5.

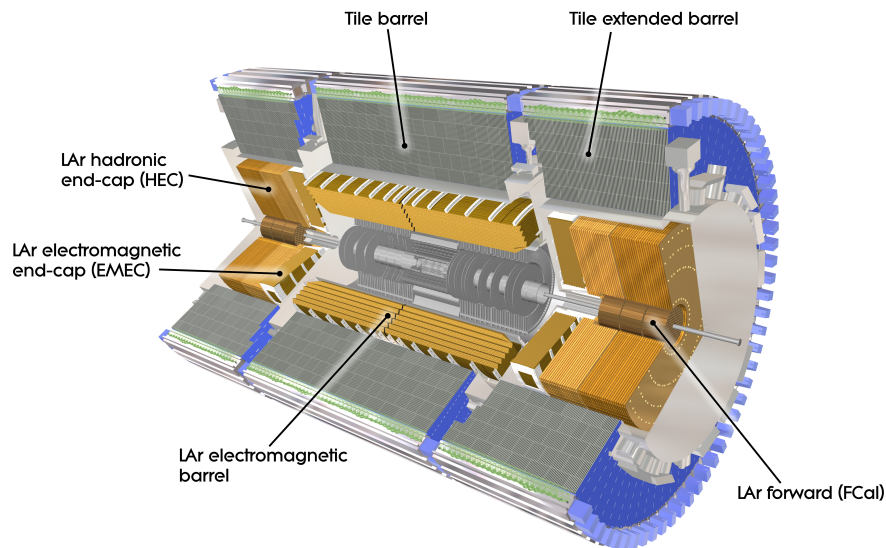


Figure 3.4: Layout of the ATLAS calorimeters [45].

Electromagnetic Calorimeter The ATLAS Electromagnetic Calorimeter [46][47] surrounds the Inner Detector and measures the energy of electrons and photons. The ECAL

is a sampling calorimeter with Liquid Argon as active material and lead as an absorber. A pre-sampler system is located between the inner detector and the ECAL to provide corrections due to the material before ECAL. The barrel ECAL is made of three longitudinally segmented layers at different radii ranging from 1.5 to 1.97 m. The $\eta \times \phi$ segmentations for each layer in the central-detector region is as follows: 0.003×0.1 for the first layer, 0.025×0.025 for the second layer and 0.5×0.025 for the third layer. The fine granularity of the first layer helps differentiate between photons and neutral pions, π^0 . Note that the granularity becomes coarser for $|\eta| > 1.4$ region. The endcap ECAL has two sides and each side consists of two concentric wheels perpendicular to the beam pipe with radius ranging from 302 to 2077 mm. The accordion geometry of the ECAL ensures the hermeticity of the detector. However, the electrons and photons in the transition region between the barrel and endcap ($1.37 < |\eta| < 1.52$) are not considered due to the presence of large material before the ECAL in this region. The thickness of ECAL is around 25 radiation lengths. The energy resolution of the ECAL (GeV) for an object which deposits energy E (GeV) is parametrized by

$$\sigma(E) = \frac{10\%}{\sqrt{E}} \oplus \frac{170 \text{ MeV}}{E} \oplus 0.7\% \quad (3.4)$$

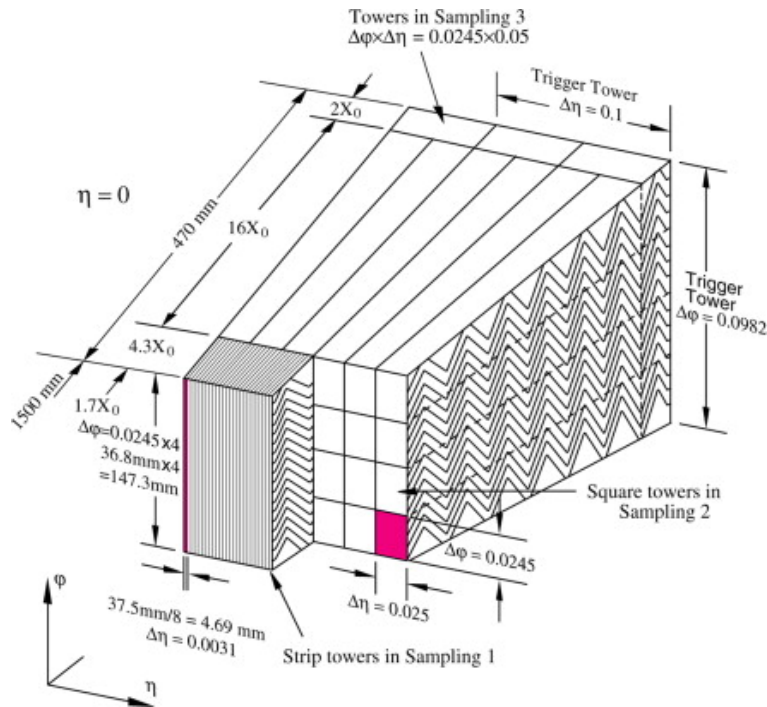


Figure 3.5: Sketch of the ATLAS electromagnetic calorimeter.

Tile Calorimeter The Tile Calorimeter [48] is a sampling tile calorimeter with 14 mm thick steel absorbers and 3 mm thick scintillating plastic tiles. This component measures and stops almost all the particles that pass through the ECAL, typically hadrons, except muons. The Tile calorimeter consists of four components: two barrels (each 5.6 m long) and two extended barrels (each 2.6m long) which provide coverage up to $|\eta| < 1.7$ and is segmented in ϕ . Each component contains 64 modules and three longitudinal layers A, BC, D are defined inside the module with cell size $\Delta\eta \times \Delta\phi$ of 0.1×0.1 in the first two layers and 0.2×0.1 in the last layer, as shown in Figure 3.6. In total, the Tile Calorimeter contains 420,000 scintillating tiles, 5182 cells and 9852 channels. The tile calorimeter ranges extends from radii of 2.28 to 4.25 m, which corresponds to 9.7 nuclear interaction lengths.

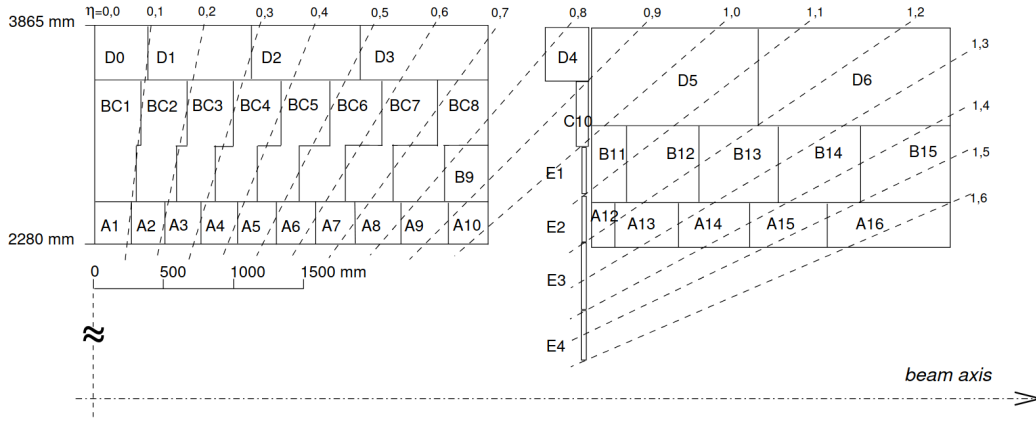


Figure 3.6: Segmentation of the Tile Calorimeter modules in radius and η shown for barrel on the left side and extended barrel on the right side.[49]

Hadronic Endcap Calorimeters (HEC) The Hadronic Endcap Calorimeter [46] is also a sampling calorimeter made of copper absorber and Liquid Argon active material. It contains two wheels which are placed behind the ECAL endcaps and extends the coverage up to $|\eta| < 3.1$. The HEC is around 10 nuclear interaction length thick [50].

Forward Calorimeters (FCAL) The Forward Calorimeter is the calorimeter system that extends the coverage of the calorimeter system in $3.1 < |\eta| < 4.9$. FCAL contains three layers on each side which have Liquid Argon as active material and the first layer uses copper as the absorber while the other two layers use Tungsten. The forward calorimeter thickness corresponds to around 9 nuclear interaction lengths [50].

3.2.3 Muon spectrometer

The ATLAS muon spectrometer (MS) [51] is the final sub-detector system of the detector. It is the largest sub-detector system and identifies muons (which are not stopped by the detectors upstream) in conjunction with the inner detector. The muon spectrometer has four subsystems: Monitored Drift Tubes, Cathode Strip Chambers, Resistive Plate Chambers and Thin Gap Chambers. The layout of the muon spectrometer is given in Figure 3.7 and consists of one barrel extending up to $|\eta| < 1.05$ and two endcap sections covering $1.05 < |\eta| < 2.7$. The muon spectrometer is immersed in a magnetic field provided by air-core toroidal magnet systems, providing a bending integral of up to 2.5 Tm and 6 Tm in barrel and endcaps, respectively. The momentum resolution for muons with $5 < p_T < 100$ GeV is around 2.3% and 2.9% for regions with $|\eta| < 2.2$ and $|\eta| > 2.2$ respectively.

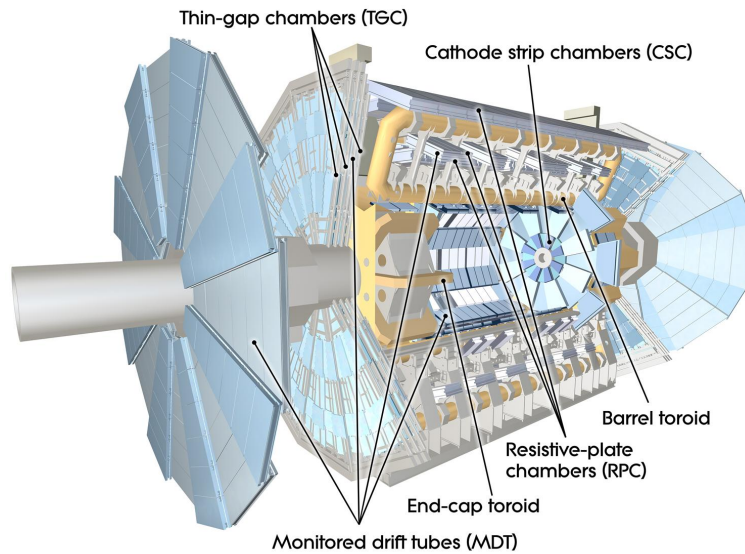


Figure 3.7: Layout of the ATLAS muon spectrometer system [52].

Monitored Drift Tubes (MDT) The Monitored Drift Tubes provide precision measurement of muon momentum up to $|\eta| < 1.7$. Each MDT is an aluminium tube (with a diameter of 3 cm and length of 0.85 - 6.5 m) filled with MDT gas made of 93% Ar and 7% CO₂ plus a few hundred ppm of water vapour at 3 bar pressure. The aluminium tube contains a cathode wire in the center. The barrel region contains three MDT chambers and are situated in radii ranging from 5 to 10 m. Each endcap contains four disk-shaped MDT layers. In total, there are 1171 chambers with 354,240 MDTs.

Cathode Strip Chambers (CSC) The Cathode Strip Chambers provide precision measurement of muon momentum at the ends of the detector in region $2.0 < |\eta| < 2.7$. CSCs are multiwire proportional chambers and they are arranged in 2×4 layers. There are 70,000 channels in the CSC in ATLAS detector.

Resistive Plate Chambers (RPC) Resistive Plate Chambers (RPC) provides up to six position measurements for the muon track and allow triggering in barrel region with $|\eta| < 1.05$. Each RPC contains two parallel resistive plates made of bakelite placed 2 mm apart and filled with gas mixture made of $C_2H_2F_4(94.7\%)$ - $C_4H_{10}(5\%)$ - $SF_6(0.3\%)$. There are a total of 354,000 RPC channels.

Thin Gap Chambers (TGC) Thin gas chambers are similar to multiwire proportional chambers but the anode wire pitch here is larger than the separation between cathode and anode. The TGCs allow triggering on muons in region with $1.05 < |\eta| < 2.4$. There are about 440,000 TGC channels.

3.3 Trigger and data acquisition system (TDAQ)

The collision rate at the LHC is 40 MHz and it is not possible to read out all collisions with the existing technology. ATLAS employs a two-stage trigger system that selects the events of interest to the physics program and reduces the readout rate to about 1 kHz [53]. The sketch of the ATLAS TDAQ system along with the event rate and bandwidth at each step is present in Figure 3.8.

3.3.1 Level-1 trigger (L1)

The first level of the trigger system is based on hardware that utilizes the information from the calorimeter and muon sub-detectors. The L1 calorimeter (L1Calo) trigger uses the energy deposits over cells in regions called the calorimeter towers. After digitization and calibration, the Cluster Processor (CP) identifies electron, photon, τ lepton candidates and the Jet/Energy-sum Processor (JEP) identifies jet candidates and gives additional information such as the total and missing transverse energy of the event. The L1 muon (L1Muon) trigger utilizes hits from the RPCs in the barrel region and the TGCs in the endcap region in addition to information in the upstream sub-detectors to identify muons.

Based on this information, the L1 trigger selects events that satisfy certain conditions such as the multiplicity of objects above thresholds, total energy deposited in the calorimeters, the missing transverse energy of the event, etc. The event rate is reduced from 40 MHz to about 100 kHz after the L1 trigger which has a latency of $2.5 \mu s$. The L1 trigger system also identifies Regions of Interest (RoIs) in the detector which are later used in the second stage of trigger system.

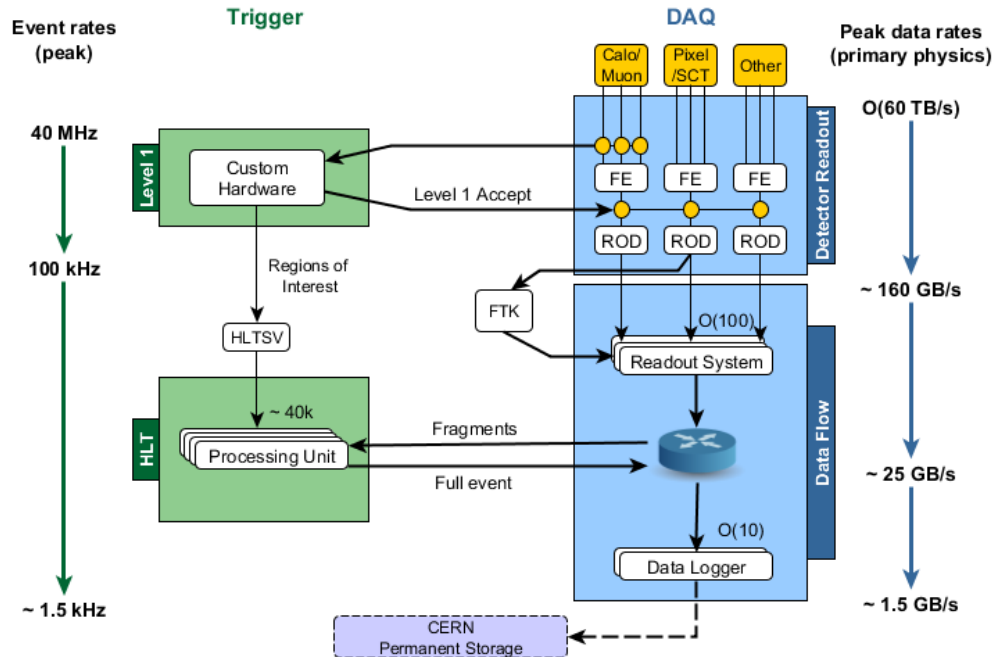


Figure 3.8: ATLAS trigger and data acquisition system showing the peak event rate and bandwidth at each step [54].

An example of the event rate after L1 trigger grouped by the trigger signature for a particular data-taking period in October 2015 is available in Figure 3.9. Given that an event can satisfy two different trigger signatures, the total L1 event rate is lower than the sum of the individual triggers. From this figure, it is clear that the single-electron and single-muon triggers contribute to a large fraction of the total event rate.

3.3.2 High-Level trigger (HLT)

HLT is a software-based trigger that runs on events that pass the L1 trigger. This stage utilizes information from the entire detector. There are fast trigger algorithms that provide early rejection followed by detailed reconstruction algorithms in the ROI identified in the L1 stage for the other events. If the event satisfies the required thresholds, the event is accepted and passed on to permanent storage. The average event rate passing the HLT trigger is about 1.2 kHz.

The event rate after the HLT system for the same data-taking period shown in Figure 3.9

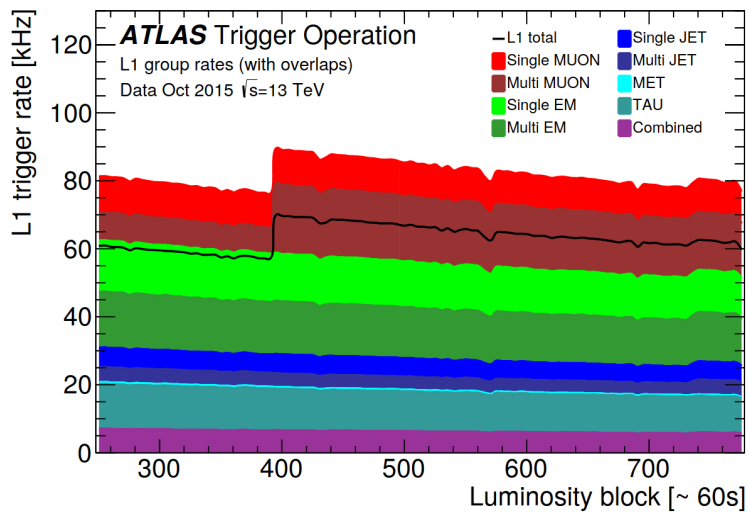


Figure 3.9: Event rate after the L1 trigger is shown for different trigger signatures for a given data-taking period in October 2015. The X-axis is time with one unit corresponding to $\tilde{60}$ s [55].

is available in Figure 3.10. Given that an event can satisfy two different trigger signatures, the total HLT event rate is lower than the sum of the individual triggers.

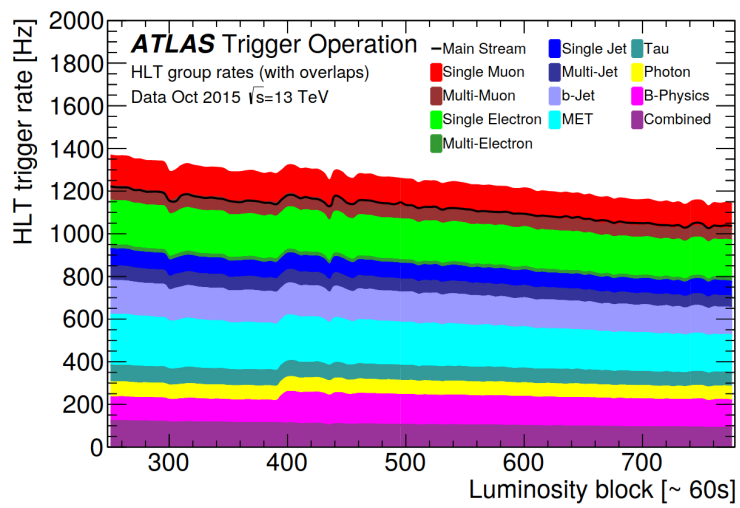


Figure 3.10: Event rate after the HLT trigger is shown for different trigger signatures for a given data-taking period in October 2015 [55].

Chapter 4

Data and simulated signal samples

This chapter describes the data and Monte Carlo simulated samples used for the thesis.

4.1 Data samples

This thesis uses the full Run-2 proton-proton collision data at center-of-mass energy of $\sqrt{s} = 13$ TeV collected with the ATLAS detector. The cumulative luminosity delivered to the ATLAS detector, recorded by the detector and the luminosity that is good for physics analysis are shown in Figure 4.1. The full dataset used for this thesis corresponds to a total integrated luminosity of $139 \pm 2.4 \text{ fb}^{-1}$. The mean number of interactions per bunch crossing is shown in Figure 4.2 for each year of data taking; it is 33.7 for the entire Run-2.

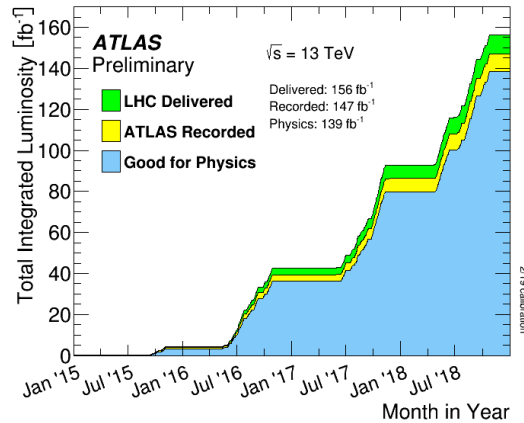


Figure 4.1: Cumulative luminosity for pp collisions delivered to ATLAS with stable operation during Run-2 along with the luminosity recorded and the luminosity that is good for physics analysis.[56]

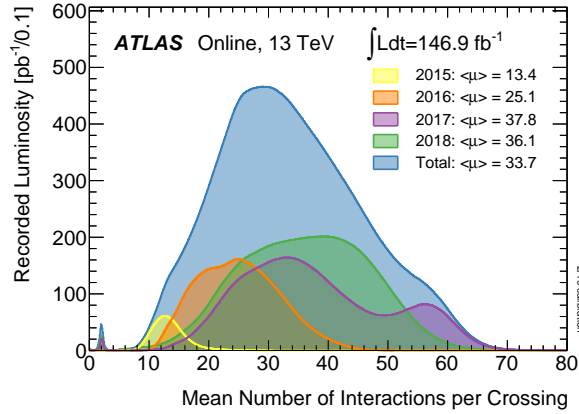


Figure 4.2: Mean number of interactions per bunch crossing for datasets recorded per year during Run-2.[56]

The dataset used for this analysis employs the lowest unrescaled single-electron and single-muon triggers [57][58]. The lowest p_T requirement on the electrons(muons) is 24(20) GeV during 2015 and 26(26) GeV during 2016-2018. The trigger efficiency is higher than 60% for leptons with p_T above 27 GeV which are used in this thesis.

4.2 Simulated signal samples

The signal Monte Carlo samples containing the associated production of the Higgs boson along with the leptonic decays of the associated process were generated at Leading Order using MadGraph 2.6.2 [59] and NNPDF2.3LO PDF set [60]. The simulated signal samples are normalized to the cross sections from Reference [61]. Separate signal samples were generated for Higgs production in associate with a W, Z and a top quark pair. These generated events are then interfaced with Pythia 8 [62] that handled the decay of the Higgs boson to the pair of long-lived NLSPs and their subsequent decay into a photon and LSP. These events are simulated with A14 tune [63] of Pythia 8 that employs the NNPDF2.3LO PDF set [60].

In order to compare to the data sample, the generated events were passed through a complete simulation of the ATLAS detector using GEANT4 [64] and the same ATLAS reconstruction algorithms used on the data samples [65]. Note that all of the simulated samples included effect of pile-up. The Monte Carlo samples (which were produced before the end of the data taking and therefore did not fully reproduced the luminosity profile) were reweighted to reproduce the observed pile-up in the data.

The signal samples are simulated with masses of the NLSP ranging from 30 to 60 GeV with a mass difference of 10 GeV between the samples. For each NLSP mass, the masses of the LSP range from 0.5 to $m_{NLSP}-10$ GeV. Each signal sample is simulated at two different

NLSP mass [GeV]	LSP mass [GeV]
30	0.5
30	10
30	20
40	0.5
40	10
40	20
40	30
50	0.5
50	10
50	20
50	30
50	40
60	0.5
60	10
60	20
60	30
60	40
60	50

Table 4.1: Table of masses of the NLSP and LSP particles for simulated samples. Each of these samples was produced with associated $W/Z/t\bar{t}$ processes and simulated at two different lifetimes of 2 and 10 ns.

NLSP mass [GeV]	LSP mass [GeV]
30	0.5
40	20
60	0.5

Table 4.2: Table of masses of the NLSP and LSP particles for additional simulated samples. Each of these samples was produced with associated $W/Z/t\bar{t}$ processes and simulated at two different lifetimes of 0.5, 5 and 20 ns.

lifetimes of 2 and 10 ns and separately for associated production of $W/Z/t\bar{t}$ processes. These signal samples are listed in Table 4.1 for reference. In addition to these samples, a few signal points were produced at alternate lifetimes of 0.5, 5 and 20 ns that enabled the extrapolation of results in lifetimes ranging from 250 ps to 100 ns. These additional samples are listed in Table 4.2.

4.3 Simulated background samples

The background Monte Carlo samples corresponding to $Z \rightarrow l\gamma$ process are simulated using the Sherpa [66] generators and are passed through the full ATLAS detector simulation implemented in GEANT4 [64] to take the detector effects into account. The pile-up effects are also included in these simulated samples. Alternate simulated samples generated using Powheg [67] and interfaced with Pythia 8 [62] are used to evaluate systematic uncertainties.

Chapter 5

Object reconstruction

The ATLAS detector identifies different particles passing through it using various sub-detectors. A sketch of different particles' paths in the detector is available in Figure 5.1. The charged-particle momentum is provided by the inner detector, electrons and photons leave the energy deposits in the electromagnetic calorimeter, jets produced from quarks and gluon hadronization leaves signature in the hadronic calorimeter while muons are measured using both the inner detector and the muon spectrometer. Neutrinos do not interact with the ATLAS detector but their presence is inferred using missing transverse energy.

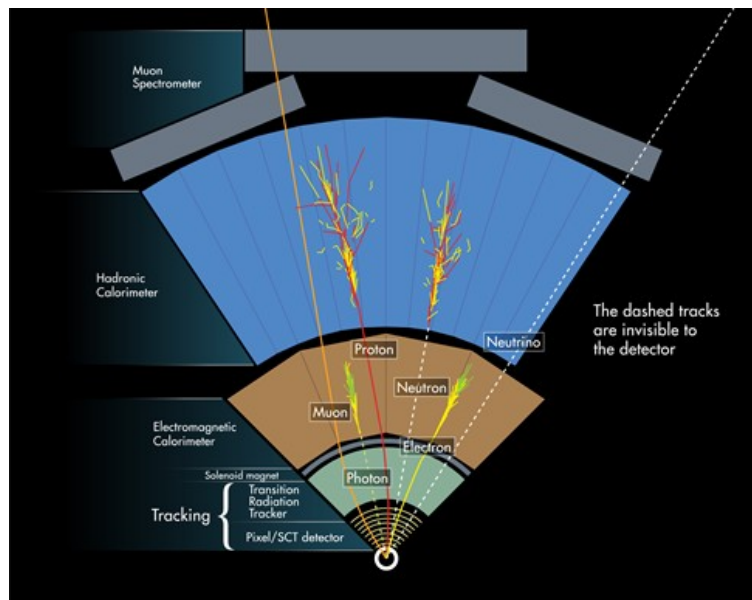


Figure 5.1: Sketch of particle paths for different objects passing through the ATLAS detector [68].

The following sections provide a description for the detection of charged particles, electrons, photons, jets, muons, missing transverse momentum.

5.1 Tracking and vertexing

Charged particles leave a trail (hits) as they pass through different layers of the inner detector and the curvature of their track due to the magnetic field is used to measure their momentum. The hits in different layers of the inner detector are combined in a multi-stage algorithms to give tracks [69]. The transverse momentum of a particle is defined as the component of the momentum in the plane perpendicular to the Z-axis. Tracks are required to have transverse momentum, p_T , greater than 500 MeV and $|\eta| < 2.5$.

Vertices are determined using an iterative fitting procedure [70] on the selected tracks. Vertices are required to have at least two tracks compatible with them. Due to pileup (multiple collisions in one beam crossing), the readout from a single trigger contains multiple vertices and the primary vertex is identified as the vertex with the highest sum of the p_T^2 values of the associated tracks.

5.2 Photons

Photons are reconstructed using energy deposits in the ECAL that are combined into topological clusters [71]. These clusters are obtained by grouping together the ECAL cells with energy in each of them above a threshold. The topological clusters that are not associated with any tracks in the inner detector are designated as photon candidates.

5.2.1 Photon identification

The photon identification and its performance during Run-2 are detailed in Reference [72]. This analysis searches for displaced photons which might have a different shower shape in the electromagnetic calorimeter. In order to maintain a high signal acceptance, the Loose identification working point, which is defined by applying the least stringent requirements on the shower shape, to identify photon candidates is utilized in this analysis. This selection places cut-based selections on the following variables: R_{had} , R_{had_1} , R_η , and w_{η_2} shower shape variables defined below.

- R_{had} : Ratio of the energy in the transverse plane to the Z-axis (transverse energy) in the hadronic calorimeter to that of the electromagnetic cluster. This variable is used in the region with $0.8 < |\eta| < 1.37$ and the variable R_{had_1} is used in other regions.
- R_{had_1} : Ratio of the transverse energy in the first layer of the hadronic calorimeter to that of the electromagnetic cluster.

- R_η : Ratio of the sum of the energies of the cells contained in a $3 \times 7 \eta \times \phi$ rectangle (measured in cell units) to that in a 7×7 rectangle, both centered around the most energetic cell.
- w_{η_2} : Measure of the lateral width of the shower, $\sqrt{(\sum E_i \eta_i^2)/(\sum E_i) - ((\sum E_i \eta_i)/(\sum E_i))^2}$, where E_i is the energy and η_i is the pseudorapidity of cell i and the sum is calculated within a window of 3×5 cells.

The Loose photon identification (Loose ID) performance is studied in two contexts for this thesis. The first one corresponds to the identification for prompt photons and the second one is the identification efficiency as a function of photon pointing. These studies are described in detail below.

5.2.1.1 Prompt-photon identification efficiency

The Loose photon identification efficiency is defined as the ratio of the number of photons satisfying the Loose identification compared to the total number of photons in the sample. Prompt photons from radiative Z boson decays ($Z \rightarrow ll\gamma$) are used for this study. The simulated Monte Carlo background samples for $Z \rightarrow ll\gamma$ process used for this study are described in detail in Section 4.3.

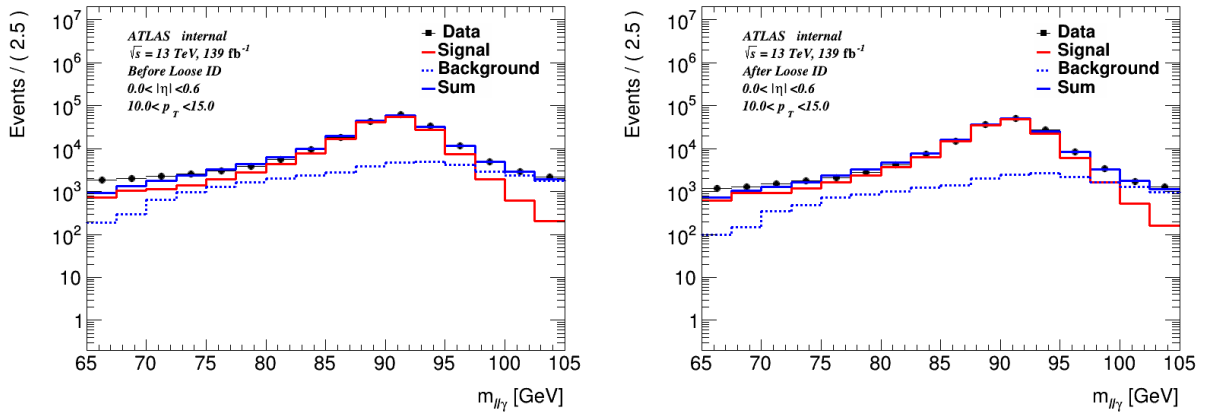


Figure 5.2: Invariant mass distribution $m_{ll\gamma}$ for events in data after all the other selections and before the Loose ID is applied is shown in the left plot while the distribution after the Loose ID is applied is shown in the right plot. The fit of this distribution to the data constructed from the $Zll\gamma$ process (red line) and background (blue dotted line) from the simulated samples is given by the solid blue line.

The selected events are required to have two oppositely charged same-flavor leptons and a photon candidate with transverse energy more than 10 GeV. The invariant mass of the

dilepton system m_{ll} is required to be below 83 GeV to reject photons from the initial-state radiation. In order to select photons from the final-state radiation, the three-body invariant mass is required to be $65 < m_{ll\gamma} < 105$ GeV.

A template fit is performed to the $m_{ll\gamma}$ distribution in data using the $Z \rightarrow ll\gamma$ process and background distributions obtained from the simulated samples. The backgrounds primarily arise from Standard Model processes such as the diboson process with electrons or jets misidentified as photons. The sum of the $Z \rightarrow ll\gamma$ process and background PDFs with floating normalization is fit to the data mass distribution. Two such fits are performed, one before the Loose ID is applied for photons and another after. Both fits are shown in Figure 5.2 and it can be seen that the resulting fit describes the data very well. The efficiency is calculated as the ratio of the number of photons satisfying the Loose ID to the total number of photons within $80 < m_{ll\gamma} < 100$ GeV.

The efficiency as a function of photon p_T is shown in Figure 5.2.1.1 for various η regions. The photon Loose ID efficiency increases with p_T and the efficiency is above 80% for photons with $p_T > 10$ GeV and 95% for photons with $p_T > 20$ GeV. The data and simulated $Z \rightarrow ll\gamma$ process sample efficiencies agree well and the ratio of the efficiency measured in data to that in the simulated samples is defined as the scale factor which is around 1 with small variation. The resulting scale factors are computed and presented in Figure 5.2.1.1 and the scale factors are very close to 1.0 and the maximum difference is around 2%. The alternate Monte Carlo sample, defined in Section 4.3, are also used to determine the scale factor and the difference was found to be less than 0.1%. Note that a small uncertainty is applied to take into account differences in the efficiency as a function of the shower shape variable R_η while the efficiency as a function of the other shower shape variables used in the Loose ID definition was found to be negligible.

This scale factor and the corresponding uncertainty is applied to the Monte Carlo displaced photon signal samples to account for differences in prompt-photon behavior in the simulated samples and data. The photon candidates also need to satisfy an isolation requirement based on $\Delta R = \sqrt{\Delta\eta^2 + \Delta\phi^2}$ variable. The FixedCutLoose isolation is used here which is defined by the requirements that the sum of the energy deposit in the ECAL around the photon within $\Delta R < 0.2$ is required to be less than 6.5% of the photon's p_T and the sum of transverse momenta within $\Delta R < 0.2$ is required to be less than 5% of the photon's p_T . This requirement is necessary to select the isolated signal photons.

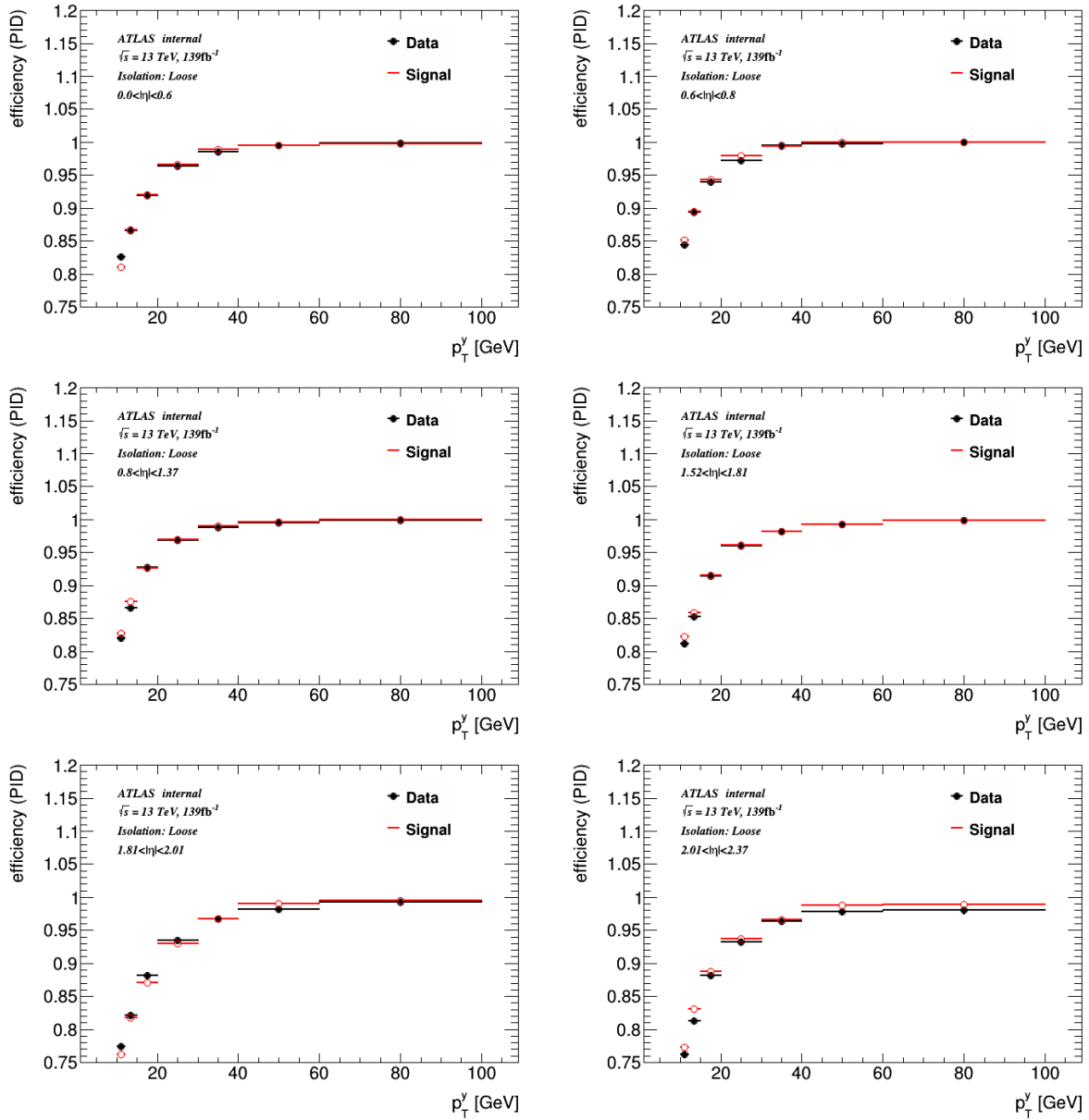


Figure 5.3: Loose photon identification efficiency for data and the Monte Carlo samples is shown here as a function of p_T for various η regions.

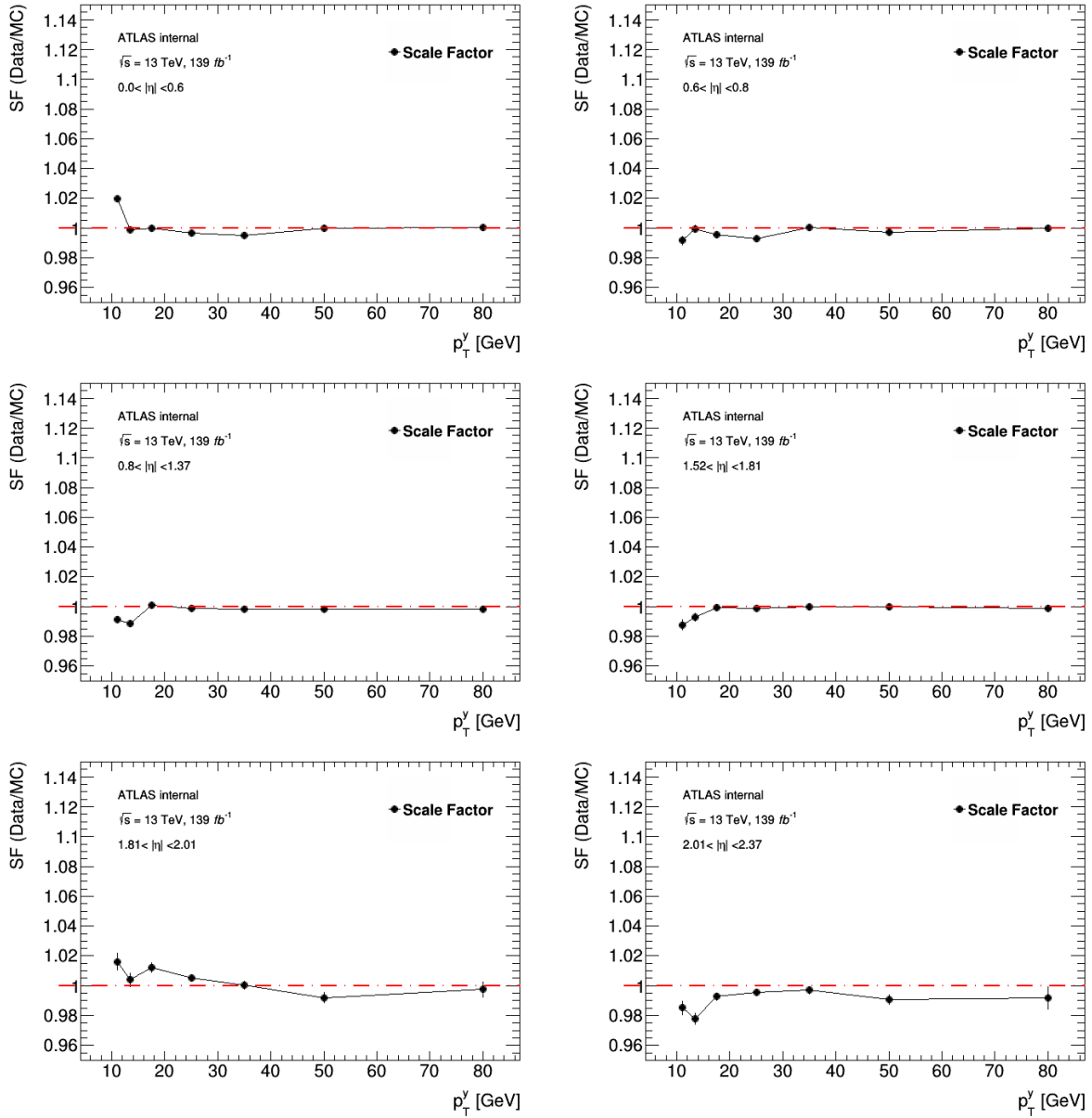


Figure 5.4: Scale factors as a function of photon p_T six different η regions. The red line corresponds to the value of 1.0 is for an easier eye guide.

5.3 Electrons

The topological cluster in the ECAL that has an associated single charged-particle track in the inner detector is designated as an electron candidate. The electron candidates are required to have $p_T > 10$ GeV and $|\eta| < 2.47$ excluding the transition region $1.37 < |\eta| < 1.52$ and satisfying the Medium identification criteria that utilizes the shower shape of energy deposits in different layers of ECAL and track parameters [72]. In addition, the electron candidates must satisfy (FCTight isolation working point) both the track-based and calorimeter-based isolation requirements.

5.4 Jets

Jets are collimated cone of hadrons and other particles which result from quarks and gluons that are produced in the collision event. Hadronic jets in the ATLAS detector are reconstructed using particle flow algorithm [73] that run on topological clusters in the calorimeter [74] using anti- k_t clustering algorithm [75] with a radius of 0.4. In this research, jets are indirectly used in the overlap removal described in Section 5.6 and in the determination of missing transverse energy. Jets are required to have a minimum p_T of 25 GeV and absolute rapidity less than 4.4.

5.5 Muons

Muons leave a track in both the inner detector and muon spectrometer and both these sub-detector systems are used for muon reconstruction [76]. Section 4.1 described their reconstruction in the inner detector while in the MS the tracks are formed by grouping hit patterns in each layer together into straight segments. In the central region with $|\eta| < 0.1$, hits are required in at least one MDT layer and there shouldn't be holes larger than one MDT layer. In the region with $0.1 < |\eta| < 2.5$, tracks are required to have at least three hits in the MDT layers. Muons in the region $2.5 < |\eta| < 2.7$ are required to have hits in at least three MDT or CSC layers. A track is accepted if the χ^2 for the fit performed on its hits passes the selection criteria. The tracks in the two sub-detector systems is obtained by performing a global fit to the muon tracks using hits in both the inner detector and MS. Note that in the region $2.5 < |\eta| < 2.7$, muons without an inner detector track but whose MS track is compatible with the interaction point are also considered.

Muons are required to have $p_T > 10$ GeV and $|\eta| < 2.7$ and satisfy the Medium identification requirement [76][77]. In addition to this, muon candidates are required to pass the calorimeter-based and track-based isolation requirements which are 95-97% efficient for muons with p_T below 60 GeV and 99% efficient for muons with higher p_T .

5.6 Overlap removal

In order to avoid double counting of objects, an overlap procedure, described here, is applied to the selected objects by placing requirements on the $\Delta R = \sqrt{\Delta\eta^2 + \Delta\phi^2}$ variable. Electrons within $\Delta R < 0.4$ of a photon are removed. Jets overlapping with photons and electrons within $\Delta R < 0.4$ and $\Delta R < 0.2$ respectively are removed. Any electrons overlapping with jets within $\Delta R < 0.4$ are then removed. Finally, muons overlapping with photons or jets within $\Delta R < 0.4$ are also removed.

5.7 Missing transverse energy

Missing transverse energy or E_T^{miss} is calculated as the negative vector sum of transverse momenta of all the objects defined above, such as electrons, photons, jets, taus and muons. Tracks that are not assigned to any of these high- p_T objects are included as part of a soft-energy term that accounts for particles from the underlying event and pileup [78]. Missing transverse energy allows the inference of particles that do not interact with the ATLAS detector, for example, neutrinos in the SM, potential dark-matter particles and stable SUSY LSPs. This is because momentum must be conserved in the plane transverse to the Z-axis before and after the collision. There is no contribution to the transverse momentum before the collision thus forcing the genuine transverse momentum after the collision to be zero excluding the detector resolution effects.

Chapter 6

Photon pointing and timing

This chapter describes the photon pointing and timing variables that are important for this thesis. The photon identification efficiency for non-pointing photons is also presented here.

6.1 Photon pointing

The ATLAS electromagnetic calorimeter is segmented longitudinally and is shown in Figure 3.5. The photon shower in the electromagnetic calorimeter spans different layers as shown in Figure 6.1 and the photon's direction of flight can be obtained by drawing a straight line between the centroids of the photon shower in the first and the second layer of the calorimeter and extrapolating it back to the Z-axis. For the prompt photons produced at the proton-proton collision point, this direction of flight points back to the primary vertex of the collision. For displaced photons that originate from the decay of a long-lived particle, this points back to a point on the Z-axis away from the primary vertex. The distance between this point and the primary vertex is defined as the photon pointing, z_{ZDCA} . This is illustrated using the cartoon in Figure 6.2.

The pointing performance is studied for electrons using $Z \rightarrow ee$ data and Monte Carlo $Z \rightarrow ll\gamma$ samples simulated using Powheg [67] interfaced with Pythia 8 [62]. The events are required to have two oppositely charged electrons with $p_T > 10$ GeV and their invariant mass satisfying $|m_{ll} - 91.18| < 10$ GeV. Here, the primary-vertex z position is used as a proxy for pointing information. The leading electron pointing distribution is obtained in the data sample and an iterative fit is performed to the core of this distribution starting with the range within $\text{Mean} \pm 2 * \text{RMS}$. For the next nine iterations, a fit is performed using the range within $\text{Mean} \pm 1.5 * \text{RMS}$ where the Mean and the RMS of the fit from the previous iteration step is used. This procedure yields a robust fit after a total of 10 iterations and the RMS of the final fit is taken as the electron pointing resolution. The same procedure is repeated for the simulated displaced photon samples.

The pointing resolution of the data and Monte Carlo samples for this process for various

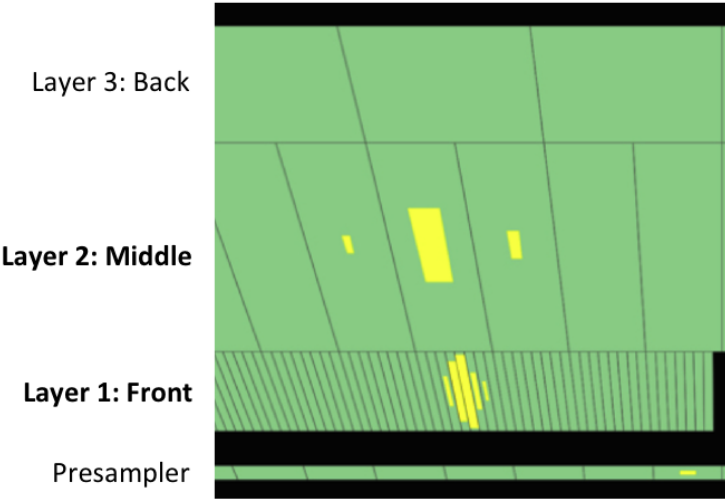


Figure 6.1: Cartoon showing the shower shape of a photon shower in different layers of the ATLAS electromagnetic calorimeter.

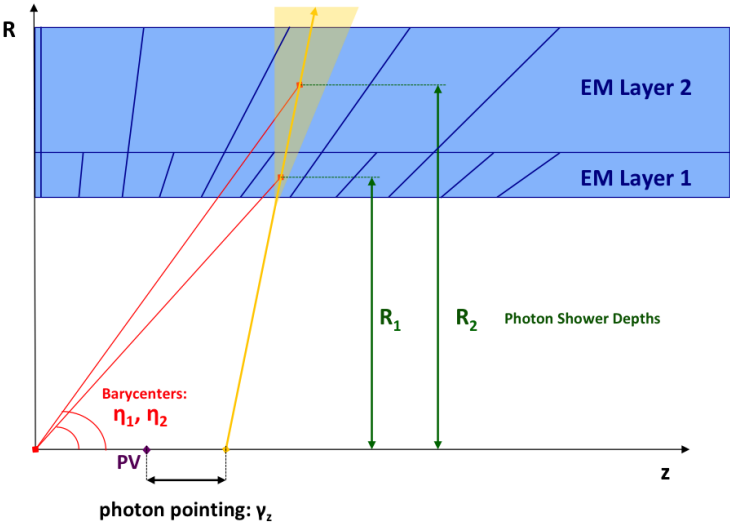


Figure 6.2: Cartoon showing the photon pointing for a displaced photon.

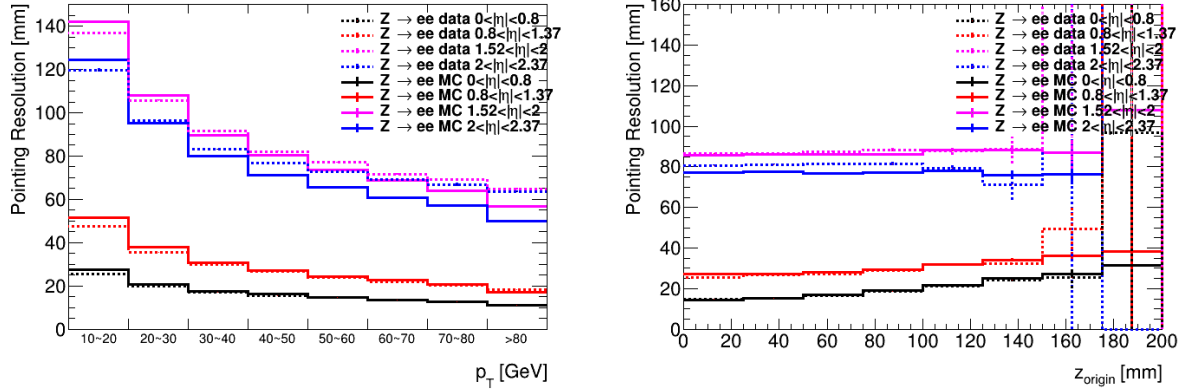


Figure 6.3: Electron pointing resolution comparison between data (dotted lines) and simulated samples (solid lines) for $Z \rightarrow ee$ process for various η regions as a function of p_T (left) and as a function of the primary vertex z position (right).

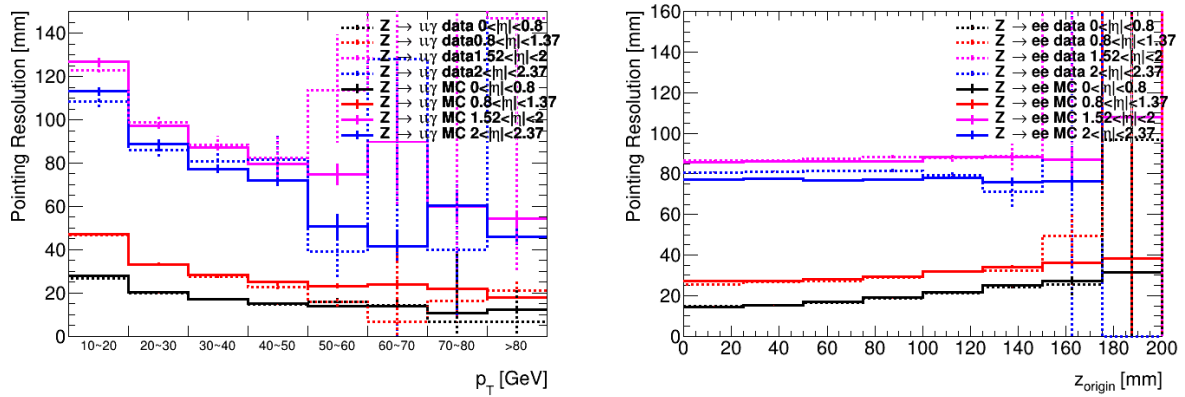


Figure 6.4: Photon pointing resolution comparison between data (dotted lines) and simulated samples (solid lines) for $Z \rightarrow ll\gamma$ process for various η regions as a function of p_T (left) and as a function of the primary vertex z (right).

η regions as a function of electron p_T on the left and pointing on the right is shown in Figure 6.3. The electrons in the barrel region have a much better pointing resolution than the electrons in the endcap. The pointing resolution gets better as the electron p_T increases and the best resolution is around 10 mm for high- p_T electrons in the central-most region. The pointing resolution becomes worse as the electron's pointing increases and the central η regions perform better than the endcaps.

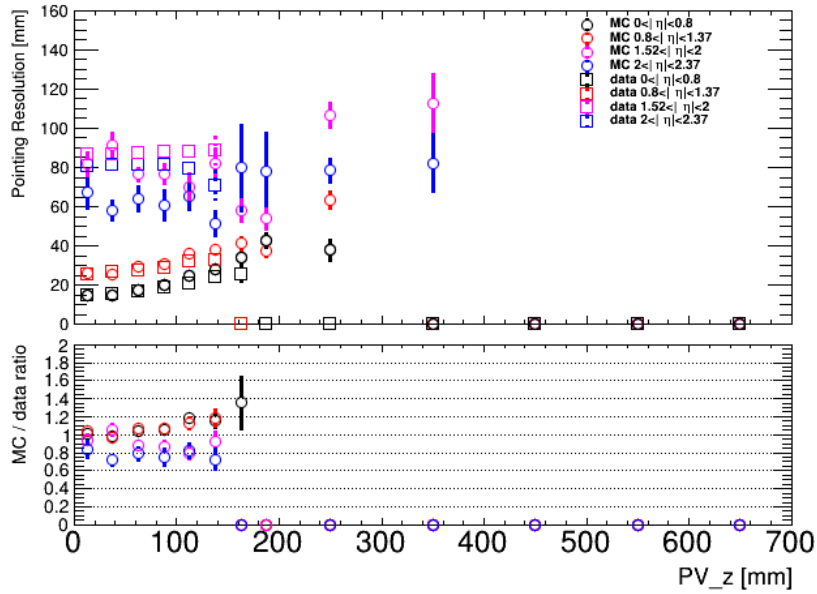


Figure 6.5: Photon pointing resolution comparison between data (squares) and simulated signal samples (circles) for various η regions as a function of photon pointing. The agreement between 0-200 mm for the barrel photons (red and black points) serves as a validation.

The performance of photon pointing is measured using the radiated $Z \rightarrow ll\gamma$ samples described in the previous section. The event selection here requires two oppositely charged same flavor leptons with the leading lepton $p_T > 27$ GeV and the subleading lepton $p_T > 10$ GeV, a photon with $p_T > 10$ GeV and the invariant mass $|m_{ll\gamma} - 91.18| < 10$ GeV. The iterative procedure described earlier is used here on the photon pointing variable. The pointing resolution for the data and Monte Carlo samples of this process for various η regions as a function of photon p_T on the left and pointing on the right is shown in Figure 6.4. Conclusions similar to the electron's pointing can be drawn here and the photon pointing performance is consistent with the electron's performance. Given the much better performance of photon pointing for the barrel photons compared to the endcap, this analysis uses only the barrel photon's pointing information.

Both of these studies provide an estimate of the photon pointing resolution as a function of photon pointing up to 200 mm. The simulated displaced photon signal provides photons with much larger values of pointing and can be used to get an estimate of the pointing resolution beyond 200 mm. The photon pointing for data samples is derived from the $Z \rightarrow ll\gamma$ study. For this study, a few Monte Carlo signal samples are selected and the comparison between photon pointing of the simulation and data is provided in Figure 6.5. The agreement between data and the simulated samples between 0-200 mm for the barrel photons (red and black points) serves as a validation. Hence, the pointing resolution beyond pointing of 200 mm is directly used from the simulated samples.

6.1.1 Non-pointing photon identification efficiency

This section summarizes the Loose photon ID efficiency as a function of photon pointing. As the photon pointing increases, its shower shape differs from that expected for a prompt photon considerably; this leads to a lower probability of it being reconstructed as a photon in the detector, hence lowering the Loose ID efficiency. This efficiency as a function of photon pointing is studied using simulated samples and is presented in Figure 6.6. The photon identification efficiency as a function of photon pointing is studied using simulated displaced photon signal and background radiative Z boson decay samples. These efficiencies obtained from simulation are compared to the efficiency obtained for data region defined for radiative Z boson decay. The Standard Model background only populates the photon pointing up to 200 mm and the efficiencies calculated for the background processes in data and Monte Carlo samples agrees with the Monte Carlo signal samples in this region. Therefore, the photon identification efficiency beyond 200 mm in pointing is taken directly from the simulated signal samples. The resulting systematic uncertainty is estimated as a function of the photon p_T and pointing. It is found to be below 15%.

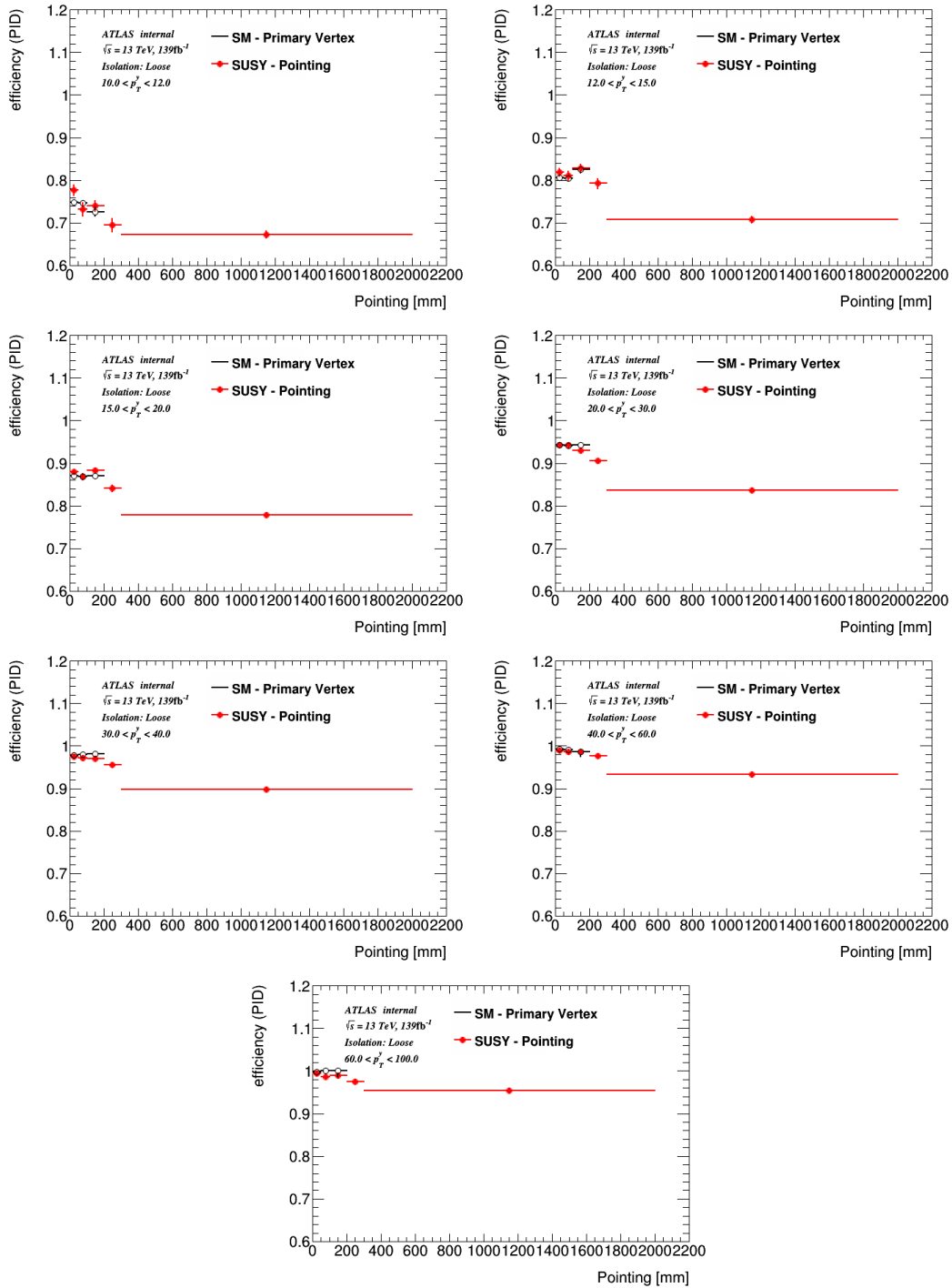


Figure 6.6: Comparison of Loose ID efficiency of the photon as a function of its pointing for different p_T ranges.

6.2 Photon timing

The ionization pulse shape for every electron and photon is recorded by sampling the shape at four different time intervals in each calorimeter cell. The deposited energy and the time of arrival of the electromagnetic object in each cell is recovered from the sampled ionization pulse shape using an optimal filtering technique [79]. A prompt photon is a photon produced at the interaction point. It is identified as such by calculating the time travelled by a photon from the interaction point to the ECAL cell (the position information of the primary vertex and the ECAL cell is available) and comparing it against the arrival time of the photon. The photon timing is officially defined as the difference in its time of arrival in an ECAL cell to that of the prompt photon. There are three distinct readout gains: low, medium and high gains in the increasing order of energy scale and each is treated separately for timing calculation.

The photon timing is defined as the arrival time of the photon in the highest energy cell, E_{cell} , in the second layer of the electromagnetic calorimeter. This energy deposited in this particular cell is a significant fraction of the entire photon's cluster energy, typically around 15-40%. The cells in the second layer also have minimal cross-talk compared to the front layer cells which are much more granular making the use of the second layer an optimum choice.

The timing for the electromagnetic objects is calibrated using the electrons from $W \rightarrow e\nu$ process and electrons from the $Z \rightarrow ee$ process is used as validation. The calibrations are obtained separately for high and medium gains which are relevant for this thesis as the signal photons from the exotic decay of the Higgs boson typically have low energy.

The calibration procedure for timing involves an iterative application of the following corrections in a sequential manner. First correction is applied to correct for the time-of-flight of the electron from the primary vertex to the E_{cell} using geometric calculations. Then, an offset is determined per Front End Board by taking the difference in the mean photon timing for the energy cluster and that recorded by each Front End Board. This is followed by an offset per channel. The timing variations are removed using a smoothing function based on the E_{cell} in the next step. The corrections related to cross-talk within the second layer are determined followed by the corrections related to the cross-talk across different layers. After this, another correction to take into account the residual channel differences is applied. This iterative procedure of corrections is applied for each run in the data and the final timing performance after this is utilized in the analysis.

The calibration procedure is validated using the electrons from $Z \rightarrow ee$ process and the timing resolution of the electron as a function of E_{cell} is shown in Figure 6.7 for medium and high gains. The online timing resolution for the ATLAS electromagnetic calorimeter is around 1 ns and the best offline timing resolution is around 220 ps.

In addition to the above procedure, additional correction is required for photons to take into account minor differences between electrons and photons. This correction is based on the cluster energy and the timing profile comparisons between the electrons and photons before and after this correction is shown in Figure 6.8. The timing profiles for electrons

and photons agree better after this correction, particularly for cluster energy below 60 GeV, where the signal photons populate. The difference is less than 50 ps for electrons and photons with cluster energy above 60 GeV.

The Monte Carlo simulated samples do not model the timing distribution appropriately. For example, the timing spread from the beam is not included here. In order to get the timing from simulated samples closer to what is observed in data, a timing smearing is applied to the simulated samples. The timing resolution can be decomposed into a correlated component resulting from the beam spread and an uncorrelated component. In the $Z \rightarrow ee$ process, both electrons are produced at the same primary vertex and they share the same collision time. The correlated and the uncorrelated components are determined by using the sum and the difference between the measured time of both the electrons. The contribution from the correlated part is around 190 ps which can be attributed to the beam spread. This is the major contribution to the overall timing resolution. This correction is implemented in the Monte Carlo samples using a Gaussian distribution. An additional uncorrelated smearing is applied as the quadrature difference between the timing in this sample and the $Z \rightarrow ll\gamma$ processes.

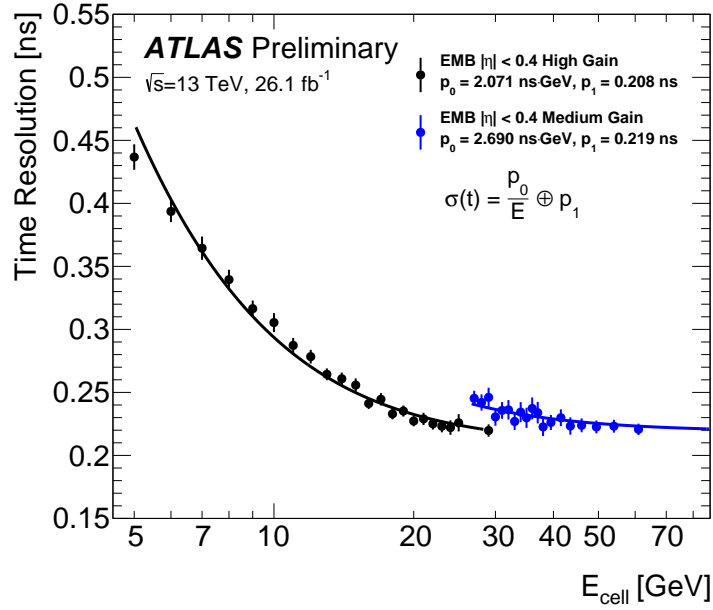


Figure 6.7: Timing resolution for electrons as a function of the E_{cell} energy for medium and high gains.

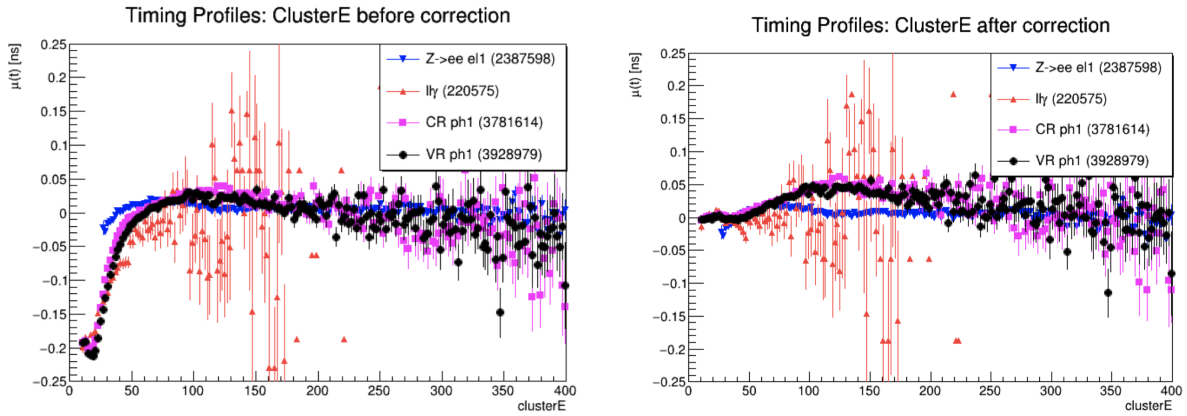


Figure 6.8: Timing profiles for electrons (blue) and photons (red) for various samples as a function of cluster energy before the cluster energy correction is applied (left) and after it is applied (right). The timing profiles for photons in the control region (magenta) and validation region (E_T^{miss}) (black) defined in Table 7.2 are also shown here for reference.

Chapter 7

Event selection

This chapter summarizes the preselection requirements on the events followed by optimization of the final event selection and classification of different regions in the data. The event yields for data and predicted signal yields for signal points obtained from the Monte Carlo samples are also presented here. The search looks for at least one non-pointing and delayed photon in the event along with at least one isolated high- p_T lepton coming from the decay of the associated $W/Z/t\bar{t}$ process. The lepton from the associated process decay is used to trigger the event.

7.1 Event preselection

All the selected events need to satisfy a single-electron and/or single-muon trigger. Electrons are required to satisfy medium identification criteria, FCTight isolation and $|\eta| < 1.37$ or $1.52 < |\eta| < 2.47$. Muons are required to satisfy the medium identification criteria, PflowLoose.FixedRad isolation working point and $|\eta| < 2.7$. The leading (subleading) lepton is required to have $p_T > 27$ GeV ($p_T > 10$ GeV). Photons in the event are required to have loose identification, FixedCutLoose isolation working point, $p_T > 10$ GeV and $|\eta| < 1.37$ or $1.52 < |\eta| < 2.37$. The preselection criteria for electrons, muons and photons are summarized in Table 7.1. All the events are required to have at least one lepton and photon satisfying the above requirements.

	Electron	Muon	Photon
Identification	Medium	Medium	Loose
Isolation	FCTight	PflowLoose.FixedRad	FixedCutLoose
Leading p_T [GeV] (subleading)	> 27 (> 10)	> 27 (> 10)	> 10
$ \eta $	< 1.37 or $[1.52, 2.47]$	< 2.7	< 1.37 or $[1.52, 2.37]$

Table 7.1: Table of event preselection criteria for electrons, muons and photons.

The events that pass the above preselection and have at least one electron and a photon are required to satisfy $|m_{e\gamma} - 91.18| > 15$ GeV to remove electrons that fake photons. The photon p_T for events satisfying $|m_{e\gamma} - 91.18| < 15$ GeV in black and the events that do not satisfy this requirement in red are shown in Figure 7.1. The feature in the black curve justifies vetoing the mass window in $m_{e\gamma}$ to reduce fake photons in the selected events.

Photons in the barrel region have better pointing and timing performance compared to those in the endcap region as can be seen from Figure 6.4. Hence, the events are required to have at least one barrel photon with $|\eta| < 1.37$. Photons in the event are required to have pointing $|z_{ZDCA}| < 2000$ mm. The photon timing is required to have $|t_\gamma| < 12$ ns to avoid events from bunch crossings before and after the particular collision event under consideration.

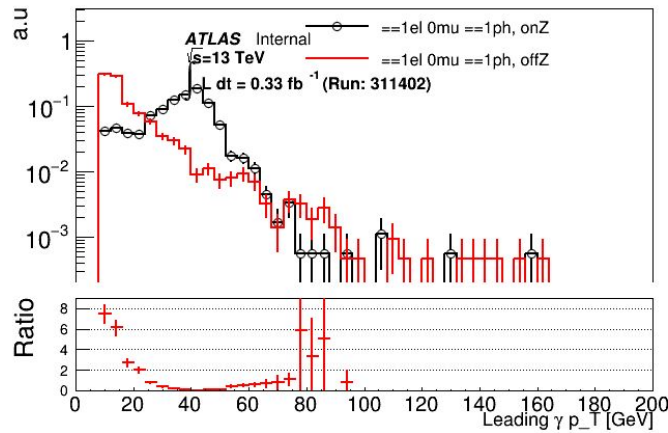


Figure 7.1: Comparison of leading-photon p_T for events corresponding to a luminosity of 0.33 fb^{-1} satisfying $|m_{e\gamma} - 91.18| < 15$ GeV in black and events that do not satisfy this requirement in red. The feature at 40 GeV in the black curve is indicative of the electrons faking photons.

7.2 Selection optimization procedure

For the signal points where $\Delta m = m_{NLSP} - m_{LSP}$ is small or the NLSP lifetime is large, there is high probability that only one photon from the signal might be reconstructed; the 1γ channel provides sensitivity to such signal points. For signal points with high δm or where the NLSP lifetime is small, there is high probability that both the signal photons are reconstructed; the lower SM background in the $\geq 2\gamma$ channel allows for much better sensitivity to such signal points. Hence, the selected events are divided into 1γ and $\geq 2\gamma$

channels to improve the signal sensitivity reach for a wide variety of signal points. For events in $\geq 2\gamma$ channel, the leading photon in p_T in barrel region is considered to be the selected photon and its timing and pointing distributions are used for the remainder of the analysis.

The displaced photon signature can be distinguished from the SM background using the following variables that require optimization of their selection cuts:

- E_{cell} : The photon timing resolution and performance depends on this variable
- E_T^{miss} : The signal final state has E_T^{miss} contribution due to the two LSPs in the event along with any neutrinos from $W/t\bar{t}$ decays. It is important to optimize the selection cuts on this variable to increase the signal sensitivity.
- Bin boundaries for photon pointing and timing: The displaced photons have high photon pointing and timing compared to background photons. The binning of the pointing and timing distributions is important to optimize the signal-to-background ratio.

A study optimizing each of these selections and identifying the signal region (SR) was performed using all the simulated signal samples. For each signal point, each of the variables described above was optimized to maximize the signal-to-background ratio using data control regions for background and predicted signal yields from the Monte Carlo samples. The signal samples with $\Delta m > 10$ GeV are best targeted using the selections $E_{cell} > 10$ GeV and $E_T^{miss} > 50$ GeV and this selection is referred to as the high-mass splitting analysis or the high- Δm analysis. In contrast, the signal samples with $\Delta m = 10$ GeV are best targeted using the selections $E_{cell} > 7$ GeV and $E_T^{miss} > 80$ GeV and this selection is referred to as the low-mass splitting analysis or the low- Δm analysis. The E_{cell} requirement for low-mass splitting analysis was lowered to increase the signal acceptance given that low Δm results in softer photons and the E_T^{miss} cut was increased to increase the signal-to-background ratio. These two analysis are treated separately in this project.

In addition to the signal region, a low E_T^{miss} control region (CR) is identified to allow the data-driven background estimation and two validation regions (VRs) are identified to validate the background estimation, one with intermediate $30 < E_T^{miss} < 50$ GeV, $VR(E_T^{miss})$, and another with signal region selections described above but with negative photon timing, $VR(t)$.

For each of the selections, the optimized binning for the photon pointing and timing along with the different analysis regions is given in Table 7.2.

7.3 Signal and background yields

Data and Monte Carlo predicted signal yields for the sequence of event selection cuts are shown in Table 7.3 and 7.4 respectively. Note that the branching ratio of Higgs to NLSP pair is assumed to be 20% which is around the upper limit imposed by the Higgs to undetected

Parameter	Low- Δm selection ($\Delta m = 10$ GeV)				High- Δm selection ($\Delta m > 10$ GeV)											
	CR	VR(E_T^{miss})	VR(t)	SR	CR	VR(E_T^{miss})	VR(t)	SR								
E_{cell} [GeV]	> 7				> 10											
E_T^{miss} [GeV]	< 30	30–50	> 80	> 80	< 30	30–50	> 50	> 50								
t_γ [ns]	> 0	> 0	< 0	> 0	> 0	> 0	< 0	> 0								
$ z_{ZDCA} $ bins [mm]	[0, 50, 100, 200, 300, 2000]															
t_γ bins [ns]																
1 γ channel									[0, 0.2, 0.4, 0.6, 0.8, 1.0, 1.5, 12.0]							
$\geq 2\gamma$ channel									[0, 0.2, 0.4, 0.6, 0.8, 1.0, 12.0]							

Table 7.2: Summary of different selections for high-mass splitting and low-mass splitting analysis that includes the selection cuts on E_{cell} , E_T^{miss} , photon pointing and timing bins along with various control, validation and signal regions.

particle searches. This table provides an estimate for the highest signal yields consistent with this result.

The signal point with (m_{NLSP} GeV, m_{LSP} GeV, τ ns) of (60,0.5,2) has the highest predicted yield in the Signal Region (SR) among all the signal points. Comparing the signal points with same m_{NLSP} and m_{LSP} but different τ shows that the signal points with lower lifetime have higher yield due to higher photon acceptance. Comparing the signal points with same τ but different Δm shows that the signal point with higher Δm has higher photon acceptance and more events populate in the $\geq 2\gamma$ channel as there is higher probability that both the signal photons satisfy the selection criteria.

Selection	Number of events
Total	119017973
Events passing trigger + ≥ 1 lepton	111664787
Events passing trigger + ≥ 1 lepton + $\geq 1\gamma$	13852973
1γ	13731614
$\geq 2\gamma$	121359
CR region	955591
1γ CR region	940707
$\geq 2\gamma$ CR region	14884
1γ low- Δm SR region	85983
$\geq 2\gamma$ low- Δm SR region	1235
1γ high- Δm SR region	205537
$\geq 2\gamma$ high- Δm SR region	2817

Table 7.3: Yields for data in different regions.

Selections / (m_{NLSP} GeV, m_{LSP} GeV, τ ns)	(60,0.5,2)	(30,0.5,2)	(50,20,2)	(60,0.5,10)	(30,0.5,10)	(50,20,10)
Total yield before selections	15105.45	15105.45	15105.45	15105.45	15105.45	15105.45
Events passing trigger + ≥ 1 lepton	6994.984	6957.499	7037.954	6955.48	7023.664	7016.068
Events passing trigger + ≥ 1 lepton + $\geq 1\gamma$	3269.706	2935.154	3163.726	1609.433	1128.328	1457.546
Events passing trigger + ≥ 1 lepton + 1γ	1948.963	2159.161	2133.148	1339.953	1026.825	1271.615
Events passing trigger + ≥ 1 lepton + $\geq 2\gamma$	1320.743	775.993	1030.578	269.480	101.503	185.931
high- Δm SR	1303.949	1172.796	1192.774	594.6473	432.0876	499.2941
1γ high- Δm SR	745.080	869.816	799.151	492.165	397.112	433.623
$\geq 2\gamma$ high- Δm SR	558.870	302.980	393.624	102.483	34.975	65.671

Table 7.4: Predicted yield for six signal samples which are labelled by (m_{NLSP} GeV, m_{LSP} GeV, τ ns). Note that the yield shown here is normalized to 139 fb^{-1} assuming 20% branching ratio of Higgs decaying to a pair of neutralinos.

Chapter 8

Background estimation

Background events passing the selection criteria from Chapter 7 can arise both from electroweak and QCD multijet processes. Such background processes are characterized as those where the reconstructed objects are properly identified (i.e. cases where the events have real charged leptons and neutrinos) and cases where one or more of the objects are misidentified. Sources of the photons in the background can be from prompt photons and electrons or jets that are misidentified as photons. The background photons are an admixture of real photons and fake photons.

8.1 Analysis strategy

This thesis uses a completely data-driven estimation method for its background. As mentioned in Chapter 7, the events in the signal region are divided into 10 categories based on the number of photons and the photon pointing. The events are categorized into 1γ and $\geq 2\gamma$ channel and into 5 pointing categories given by bin boundaries of $\{0, 50, 100, 200, 300, 2000\}$ mm in each channel. The timing distribution in each category is used to distinguish the signal and background. A simultaneous fit to the data timing distribution is performed in each of the 10 categories including the signal component from the simulated Monte Carlo signal samples and data-driven background timing templates. The fit procedure is described in detail in Chapter 10. The data in the signal region is a combination of signal and background. The timing distribution for the signal is directly taken from the simulated Monte Carlo samples. The timing distribution for the background is obtained from data and must include both components for real photons and for fake photons. This is achieved by constructing real-enhanced and fake-enhanced timing templates described in Section 8.2. The timing probability density function (PDF) used in the fit in each of the pointing categories can be modeled by

$$N_b[\alpha f_\gamma(t) + (1 - \alpha) f_{fake}(t)] + \mu N_s f_{signal}(t) \quad (8.1)$$

where N_b is the normalization parameter which is a free parameter in the fit, α is the mixing fraction for the real-enhanced and fake-enhanced templates, often referred to as purity, f_γ

refers to the real-enhanced photon timing template, f_{fake} refers to the fake-enhanced photon timing template, μ is the BR($H \rightarrow \text{NLSP NLSP}$) which is the parameter of interest in the fit, N_s and $f_{signal}(t)$ are the signal normalization and signal photon timing shape obtained from the Monte Carlo signal samples. Note that all the systematic uncertainties described in Chapter 9 are added to the background fit as a nuisance parameters. This chapter describes the details of the real-enhanced and fake-enhanced photon templates used for the background fit.

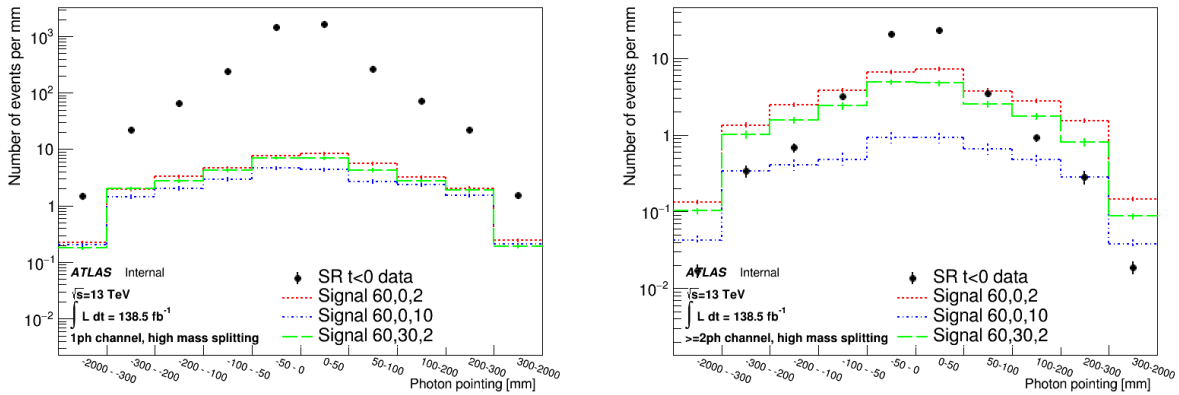


Figure 8.1: Pointing shape normalized to the bin width is compared between the $VR(t)$ or SR $t < 0$ region data and few signal points using 100% Higgs to NLSP branching ratio for high mass splitting or the high- Δm analysis for the 1γ channel (left) and the $\geq 2\gamma$ channel (right).

The pointing distribution comparing the data in the validation region $VR(t)$ and various signal points is shown in Figure 8.1 and 8.2 for the high- Δm and low- Δm analysis respectively. The signal has a broader pointing distribution compared to the $VR(t)$ region data. Statistics in the 1γ channel are much higher than the $\geq 2\gamma$ channel and it can be seen that the signal-to-background ratio is higher in the $\geq 2\gamma$ channel. The signal points with longer lifetime have broader photon pointing compared to the ones with lower lifetime as these two variables are correlated for displaced photons.

8.2 Background timing templates

The real-enhanced and fake-enhanced photon timing distributions are obtained from the low- E_T^{miss} control region. Several options for defining the background templates have been studied and summarized in Section 8.4 and the final choice of templates is:

- Real-enhanced photon timing template: This is defined as the sum of two different data regions to increase signal statistics. The first is from the radiative $Z \rightarrow ll\gamma$ decay photons where the events are required to satisfy all the event preselection mentioned in Chapter 7 and to contain two leptons of opposite-sign same flavor and a photon which satisfy $m_{ll} < 83$ GeV and $|m_{ll\gamma} - 91.18| < 10$ GeV. The second timing template is from photons that pass medium (tight) identification for the 1γ ($\geq 2\gamma$) channel in the $E_T^{miss} < 30$ GeV region.
- Fake-enhanced photon timing template: This template is also derived from the $E_T^{miss} < 30$ GeV region with photons that pass the loose identification and fail the medium (tight) identification for 1γ ($\geq 2\gamma$) channel.

These two background templates are orthogonal to each other and form a complete basis to model any photon's timing distribution including in the signal region. These two timing templates are determined separately for the high- Δm and low- Δm analysis by placing E_{cell} greater than 10 and 7 GeV respectively.

In order to model the timing distribution in the SR, these templates are reweighted in the E_{cell} variable to its distribution in the SR. This reweighting ensures that the templates have similar photon kinematics as the signal region photons since the photon timing performance depends critically on the E_{cell} variable. The reweighting is performed by assigning event weights to the template distributions based on the bin-by-bin ratio of E_{cell} between the target distribution in the SR and the control region. The uncertainties associated with this reweighting are much smaller than the statistical uncertainties on this distribution. The E_{cell} distribution for the high- Δm VR(t) and CR medium photons before and after E_{cell} reweighting are shown in Figure 8.3. The bins used for E_{cell} are the ones shown in this Figure. Weights are determined separately for each background template in the 1γ channel and $\geq 2\gamma$ channel. Note that reweighting in additional dimensions in several other variables such as η , p_T , f_1 (ratio of the energy in the first layer to the total photon cluster) was also explored but the statistics were limited to perform reweighting in multiple dimensions and the difference in the resulting timing distributions was negligible compared to the ones obtained just after E_{cell} reweighting. After the templates are reweighted in E_{cell} , the timing templates have a small residual timing means of around 50 ps. These timing templates are shifted by this residual mean to avoid the timing asymmetry between the $t < 0$ and $t > 0$ regions.

The real-enhanced and fake-enhanced photon timing distributions before and after E_{cell} reweighting to the high- Δm SR along with the mean shift are shown on the left and right side of Figure 8.4 respectively. Similar timing distributions for templates reweighted to the low- Δm SR are shown in Figure 8.5.

The comparison between the final real-enhanced and fake-enhanced photon timing templates for the high- Δm SR and low- Δm analysis are shown in Figure 8.6 and 8.7 respectively. The fake-enhanced photons have a broader timing distribution compared to the real-

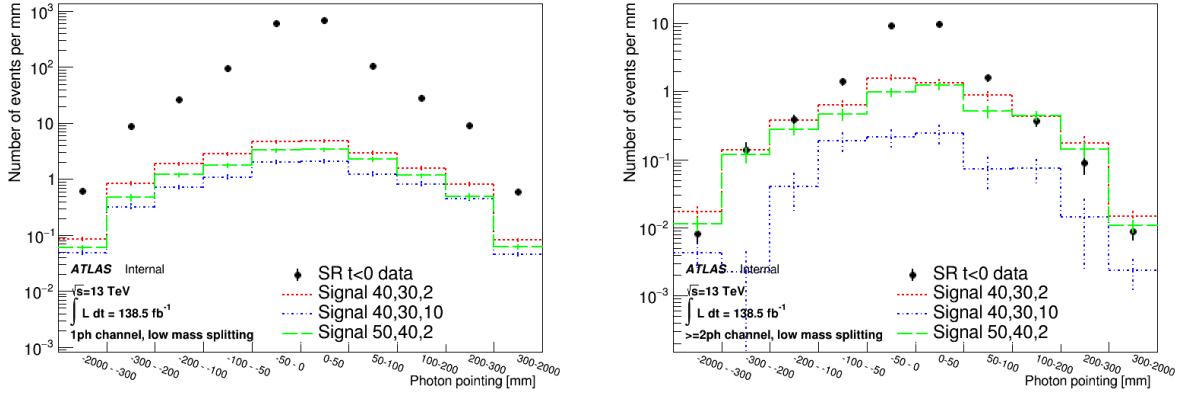


Figure 8.2: Pointing shape normalized to the bin width is compared between the $VR(t)$ or SR $t < 0$ region data and few signal points using 100% Higgs to NLSP branching ratio for low mass splitting or low- Δm analysis for the 1γ channel (left) and the $\geq 2\gamma$ channel (right).

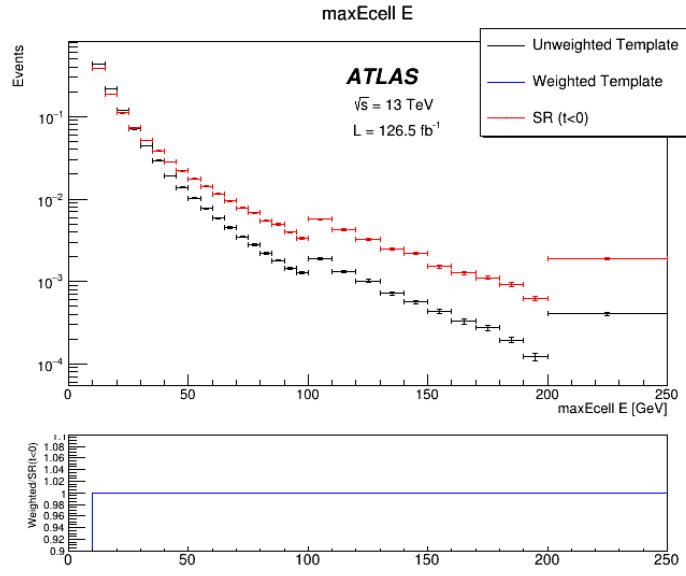


Figure 8.3: E_{cell} distribution for high- Δm $VR(t)$ in red points, CR medium photons in black points, and the ratio of the reweighted CR (medium) timing to the SR ($t < 0$) in blue curve in the bottom panel. Note that the jump in the distribution is due to a change in the bin width.

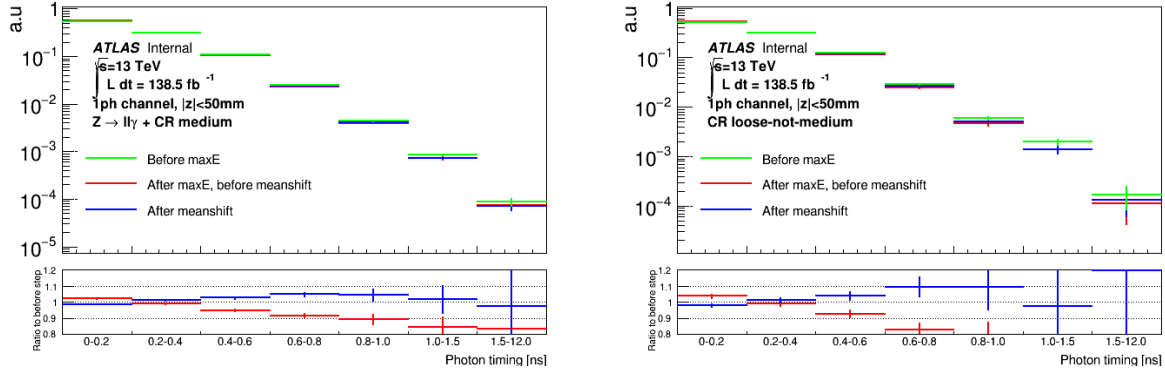


Figure 8.4: Real-enhanced (left) and fake-enhanced (right) photon timing distribution before E_{cell} reweighting in green, after E_{cell} reweighting to high- Δm SR in blue and after the residual mean shift in red color for $|z_{DCA}| < 50$ mm and 1γ channel.

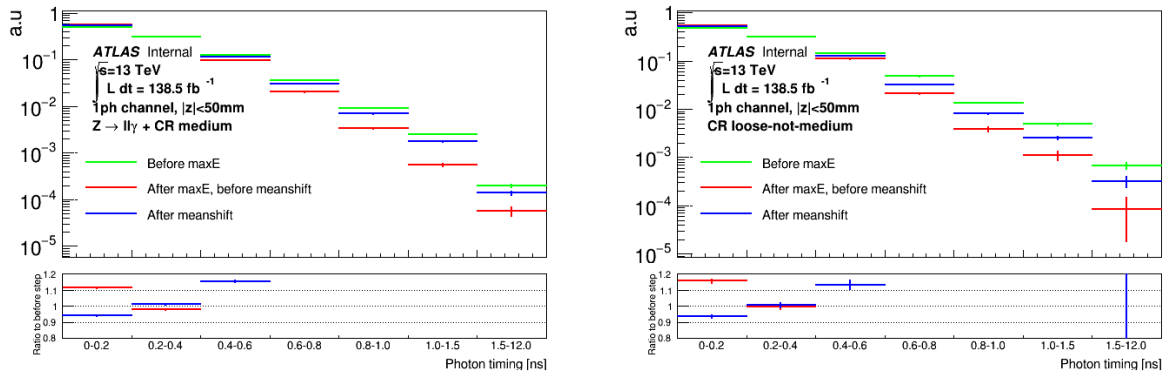


Figure 8.5: Real-enhanced (left) and fake-enhanced (right) photon timing distribution before E_{cell} reweighting in green, after E_{cell} reweighting to low- Δm SR in blue and after the residual mean shift in red color for $|z_{DCA}| < 50$ mm and 1γ channel.

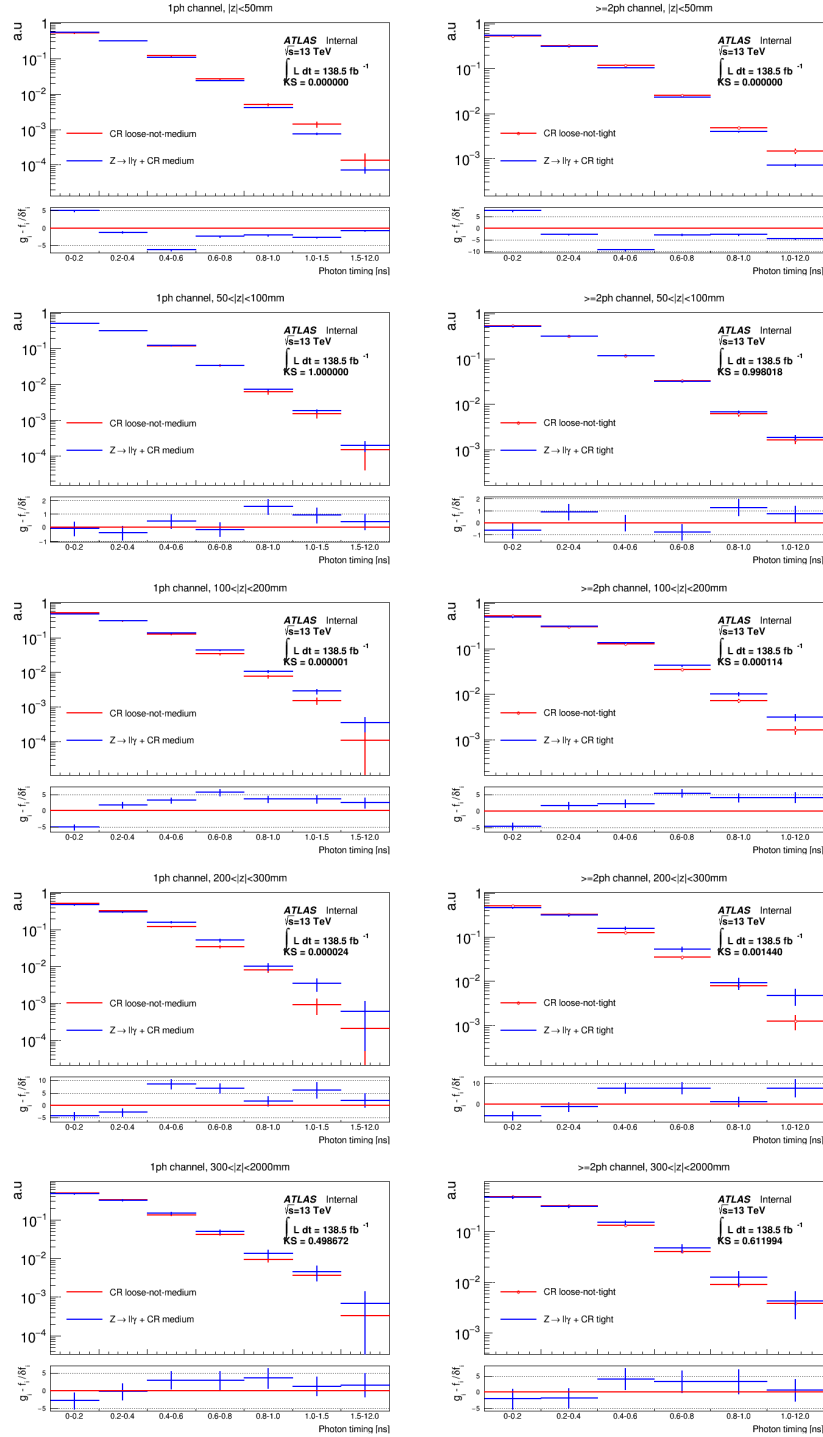


Figure 8.6: Real-enhanced and fake-enhanced photon timing template comparison in different pointing categories in 1γ channel on the left and $\geq 2\gamma$ channel on the right. These templates use $E_{cell} > 10$ GeV and reweighted in E_{cell} to match that of high- Δm SR and templates are shifted by the mean of their timing distribution.

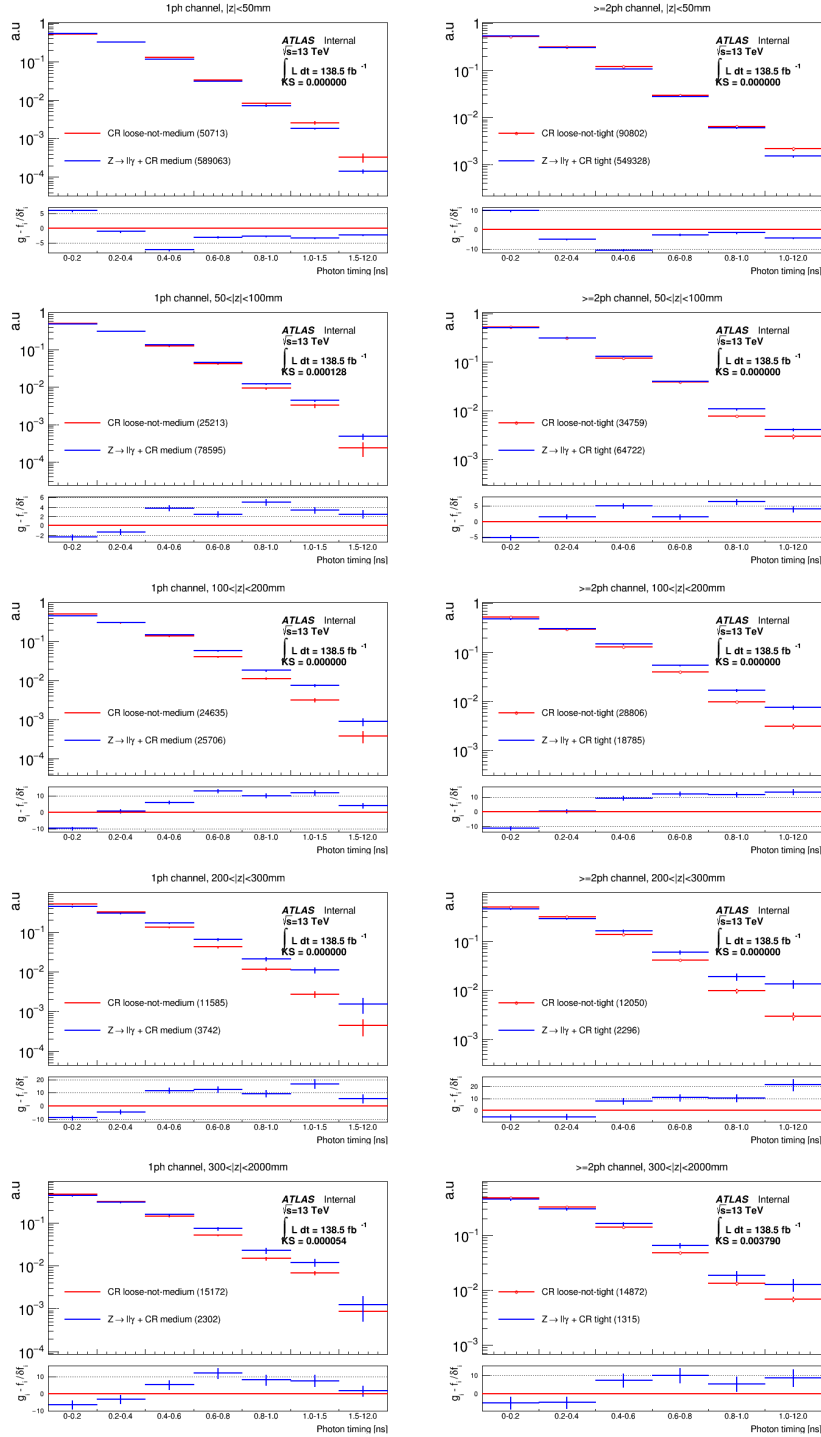


Figure 8.7: Real-enhanced and fake-enhanced photon timing template comparison in different pointing categories in 1γ channel on the left and $\geq 2\gamma$ channel on the right. These templates use $E_{cell} > 7$ GeV and reweighted in E_{cell} to match that of low- Δm SR and templates are shifted by the mean of their timing distribution.

enhanced photons as most of the real-enhanced photons are derived primarily from prompt sources.

8.3 KS-tests for background templates

The linear combination of the real-enhanced and fake-enhanced photon timing templates through the mixing fraction, a free parameter in the fit, is used to provide a description for the background timing distribution in the SR. This fit is only viable when the two templates are distinguishable. In the instances where the templates are indistinguishable, the mixing fraction is fixed to 0.5 to avoid issues with the fit instability. A Kolmogorov-Smirnov (KS) test is used to determine if the background templates are distinguishable in each pointing category. The KS-test value in each pointing category is provided on the plots in Figures 8.6 and 8.7. A summary of the KS-test is presented in Table 8.1. If the KS-test value is lower than 0.9, then the templates are considered distinguishable and the mixing fraction is allowed to float in the fit. If the KS-test value is higher than 0.9, then the templates are considered indistinguishable and the mixing fraction is set to 0.5 to optimally use the statistics in the templates. The mixing fraction is fixed for two pointing categories in the high- Δm analysis and for none of the pointing categories in the low- Δm analysis.

Category	high- Δm SR		low- Δm SR	
	Medium	Tight	Medium	Tight
$ z_{DCA} < 50$ mm, 1γ	0.000	0.000	0.000	0.000
$50 < z_{DCA} < 100$ mm, 1γ	0.945	1.000	0.001	0.000
$100 < z_{DCA} < 200$ mm, 1γ	0.000	0.000	0.000	0.000
$200 < z_{DCA} < 300$ mm, 1γ	0.000	0.000	0.000	0.000
$300 < z_{DCA} < 2000$ mm, 1γ	0.744	0.602	0.093	0.004
$ z_{DCA} < 50$ mm, $\geq 2\gamma$	0.000	0.000	0.000	0.000
$50 < z_{DCA} < 100$ mm, $\geq 2\gamma$	0.703	0.999	0.003	0.000
$100 < z_{DCA} < 200$ mm, $\geq 2\gamma$	0.000	0.000	0.000	0.000
$200 < z_{DCA} < 300$ mm, $\geq 2\gamma$	0.000	0.000	0.000	0.000
$300 < z_{DCA} < 2000$ mm, $\geq 2\gamma$	0.853	0.511	0.075	0.002

Table 8.1: KS-test values of the real-enhanced and fake-enhanced timing shape comparisons for timing templates in each pointing category for the high- Δm and low- Δm analysis.

8.4 Selection of the background timing templates

Three different sets of definitions for the background timing templates were explored before making the final selections described in the previous section. This section outlines the various choices and the procedure to make the final choice. The three definitions explored are defined below

- Medium templates: Real-enhanced photon timing distribution is a sum of the radiative Z-decays and photons from the CR that pass the medium identification. The fake-enhanced photon timing distribution is defined using the photons that pass loose identification and fail the medium identification (loose-not-medium). Same definition is used in the 1γ and $\geq 2\gamma$ channels.
- Tight templates: Real-enhanced photon timing distribution is a sum of the radiative Z-decays and photons from the CR that pass the tight identification. The fake-enhanced photon timing distribution is defined using the photons that pass loose identification and fail the tight identification (loose-not-tight). Same definition is used in 1γ and $\geq 2\gamma$ channels.
- Mixed templates: Real-enhanced photon timing distribution is a sum of the radiative Z-decays and photons from the CR that pass the medium (tight) identification for the 1γ ($\geq 2\gamma$) channel. The fake-enhanced photon timing distribution is defined using the photons that pass loose-not-medium (loose-not-tight) for 1γ ($\geq 2\gamma$) channel. Same definition is used in the 1γ and $\geq 2\gamma$ channels. (This is the final selection of the templates.)

The procedure to determine the final selection of the background templates is to use each set of these templates to perform a simultaneous photon timing distribution fit in all the 10 pointing categories in the $VR(t)$ and the $VR(E_T^{miss})$ regions and make a choice based on the templates that describe each of these validation regions the best. In this test, signal-plus-background timing PDF is used to fit a given VR and the signal strength is a free parameter in the fit. For the optimized templates, the background templates should provide the best, as defined using the strategy described here, description of the VR datasets and the significance of the signal should be close to zero. Given that the pointing and timing distributions for all the 36 signal points are different, signal-plus-background fits are performed for all of them and the template choice that results in the significance of most of the signal points close to zero is chosen.

The significance for the signal-plus-background fits to the $VR(t)$ region using 3 set of templates is shown in Figure 8.8. For the high- Δm $VR(t)$ region, the best description is provided by medium-template and mixed-template choices with the mixed-template choice having the significance closest to zero for most of the signal points. For the low- Δm $VR(t)$, the best description is provided by the medium-template choice. The study performed using $VR(E_T^{miss})$ also provided similar results. Hence, the mixed template choice is used for the analysis. This choice of templates also resulted in the lowest negative log likelihood values for the fits which further supports this decision.

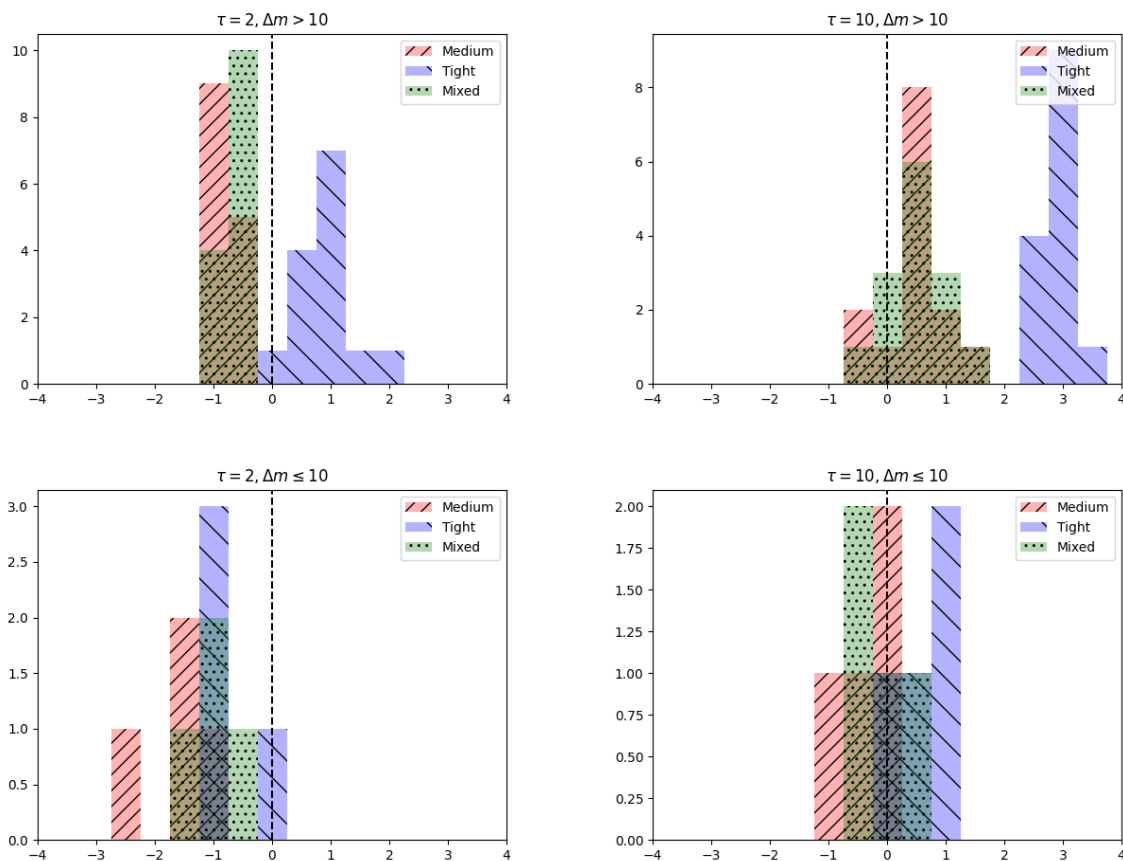


Figure 8.8: Distribution of the significance for signal-plus-background fits to the high- Δm $VR(t)$ is shown in the first row for the signal points with lifetime of 2 ns (10 ns) on the left (right). Similar distributions for the low- Δm $VR(t)$ is shown in the second row. A positive significance suggests an excess while a negative significance suggests a deficit.

Chapter 9

Systematic uncertainties

This chapter details the various systematic uncertainties which are included in this analysis. The systematic uncertainties are divided into two separate categories: one affecting the background estimation and the other affecting the signal samples.

9.1 Background systematic uncertainties

The statistical uncertainties for the real-enhanced and fake-enhanced photon timing templates are obtained directly from the statistics of the data control regions in each pointing category. These uncertainties are calculated in each individual timing bin and are considered uncorrelated in the fit.

9.1.1 Template shape systematics

The shape uncertainty related to the background templates is calculated in each pointing category using the alternate definition of templates described in Section 8.4. The shape uncertainty for the real-enhanced and fake-enhanced templates is taken as the difference in the timing shape distribution between the medium and tight templates defined in Chapter 8. The medium real-enhanced template comprises of the photons from radiative Z boson decays and those that pass medium identification in the CR and tight real-enhanced template consists of the photons from radiative Z boson decays and those that pass tight identification in the CR in each pointing category. The medium fake-enhanced template comprises of photons that pass loose but fail medium identification. The tight fake-enhanced template consists of the photons that pass loose but fail tight identification in the CR. These uncertainties for each background template are correlated between different timing bins in each individual pointing category and a single nuisance parameter is implemented in the fit per pointing category.

The relative systematic uncertainties of the real-enhanced template and fake-enhanced template are summarized in Table 9.1 and 9.2 respectively for the high- Δm analysis. Similar

tables are available for the low- Δm analysis in Table 9.3 and 9.4. Note that one nuisance parameter is implemented for the real-enhanced template and one for the fake-enhanced template per pointing category.

Pointing category	0-0.2 ns	0.2-0.4 ns	0.4-0.6 ns	0.6-0.8 ns	0.8-1 ns	1-1.5 ns	1.5-12 ns
0-50mm, 1γ	0.002	-0.002	0.001	-0.024	-0.007	0.053	-0.346
50-100mm, 1γ	-0.003	0.001	0.009	-0.018	0.076	0.035	0.431
100-200mm, 1γ	-0.013	0.014	0.007	0.045	0.004	0.085	1.164
200-300mm, 1γ	-0.011	-0.005	0.052	0.020	0.004	-0.168	1.390
300-2000mm, 1γ	-0.006	0.004	0.000	0.035	0.014	0.018	0.224
Pointing category	0-0.2 ns	0.2-0.4 ns	0.4-0.6 ns	0.6-0.8 ns	0.8-1 ns	1-12 ns	
0-50mm, $\geq 2\gamma$	-0.002	0.003	-0.008	0.033	0.004	-0.025	
50-100mm, $\geq 2\gamma$	0.010	-0.022	0.013	0.035	-0.064	-0.057	
100-200mm, $\geq 2\gamma$	0.014	-0.015	-0.014	-0.032	0.015	-0.144	
200-300mm, $\geq 2\gamma$	0.008	0.011	-0.059	0.000	-0.001	-0.062	
300-2000mm, $\geq 2\gamma$	0.014	-0.017	0.004	-0.039	-0.009	-0.030	

Table 9.1: Relative uncertainties for the real-enhanced templates for the high- Δm analysis. Each column corresponds to a timing bin, and each row corresponds to a pointing category.

Pointing category	0-0.2 ns	0.2-0.4 ns	0.4-0.6 ns	0.6-0.8 ns	0.8-1 ns	1-12 ns	
0-50mm, 1γ	0.002	0.000	-0.007	-0.008	-0.011	-0.064	0.003
50-100mm, 1γ	0.001	0.000	-0.002	-0.010	0.009	-0.017	-0.185
100-200mm, 1γ	-0.001	-0.005	0.014	0.002	-0.004	0.060	-0.229
200-300mm, 1γ	-0.017	0.004	0.016	0.054	0.073	0.483	-1.000
300-2000mm, 1γ	0.013	-0.030	0.035	-0.015	-0.039	0.054	-1.000
Pointing category	0-0.2 ns	0.2-0.4 ns	0.4-0.6 ns	0.6-0.8 ns	0.8-1 ns	1-12 ns	
0-50mm, $\geq 2\gamma$	-0.002	0.000	0.008	0.008	0.014	0.065	
50-100mm, $\geq 2\gamma$	-0.002	0.003	-0.001	0.008	-0.004	0.033	
100-200mm, $\geq 2\gamma$	0.002	0.000	-0.009	0.000	-0.005	-0.023	
200-300mm, $\geq 2\gamma$	0.030	-0.026	0.009	-0.095	-0.091	-0.261	
300-2000mm, $\geq 2\gamma$	-0.035	0.059	-0.017	0.034	0.050	0.039	

Table 9.2: Relative uncertainties for the fake-enhanced templates for the high- Δm analysis. Each column corresponds to a timing bin, and each row corresponds to a pointing category.

Pointing category	0-0.2 ns	0.2-0.4 ns	0.4-0.6 ns	0.6-0.8 ns	0.8-1 ns	1-1.5 ns	1.5-12 ns
0-50mm, 1γ	-0.002	0.007	0.002	-0.026	-0.066	-0.057	-0.285
50-100mm, 1γ	-0.010	0.011	0.012	-0.001	0.022	0.024	0.220
100-200mm, 1γ	-0.016	0.017	0.004	0.039	0.023	0.080	0.318
200-300mm, 1γ	-0.016	-0.008	0.062	0.042	0.029	0.048	0.605
300-2000mm, 1γ	-0.011	0.003	0.004	0.040	0.058	0.065	0.107
Pointing category	0-0.2 ns	0.2-0.4 ns	0.4-0.6 ns	0.6-0.8 ns	0.8-1 ns	1-12 ns	
0-50mm, $\geq 2\gamma$	0.007	-0.010	-0.014	0.038	0.071	0.065	
50-100mm, $\geq 2\gamma$	0.025	-0.054	0.035	0.030	0.024	-0.009	
100-200mm, $\geq 2\gamma$	0.007	-0.006	-0.006	-0.028	-0.008	-0.093	
200-300mm, $\geq 2\gamma$	0.020	0.005	-0.067	-0.035	-0.056	-0.109	
300-2000mm, $\geq 2\gamma$	0.020	-0.014	-0.008	-0.047	-0.058	-0.068	

Table 9.3: Relative uncertainties for the real-enhanced templates for the low- Δm analysis. Each column corresponds to a timing bin, and each row corresponds to a pointing category.

Pointing category	0-0.2 ns	0.2-0.4 ns	0.4-0.6 ns	0.6-0.8 ns	0.8-1 ns	1-12 ns	
0-50mm, 1γ	0.002	-0.001	-0.005	-0.004	-0.004	-0.018	0.011
50-100mm, 1γ	0.001	0.000	-0.005	-0.001	0.028	0.017	-0.007
100-200mm, 1γ	-0.003	-0.013	0.021	0.025	0.024	0.076	-0.060
200-300mm, 1γ	-0.015	-0.009	0.028	-0.011	0.078	0.357	-0.135
300-2000mm, 1γ	0.008	-0.026	0.024	0.022	-0.132	0.203	-0.237
Pointing category	0-0.2 ns	0.2-0.4 ns	0.4-0.6 ns	0.6-0.8 ns	0.8-1 ns	1-12 ns	
0-50mm, $\geq 2\gamma$	-0.002	0.000	0.007	0.004	0.006	0.022	
50-100mm, $\geq 2\gamma$	-0.004	0.007	0.000	0.000	-0.028	-0.018	
100-200mm, $\geq 2\gamma$	0.005	0.010	-0.019	-0.030	-0.028	-0.064	
200-300mm, $\geq 2\gamma$	0.017	0.008	-0.017	-0.015	-0.087	-0.249	
300-2000mm, $\geq 2\gamma$	-0.026	0.039	0.002	-0.008	0.161	-0.134	

Table 9.4: Relative uncertainties for the fake-enhanced templates for the low- Δm analysis. Each column corresponds to a timing bin, and each row corresponds to a pointing category.

9.1.2 Non-closure uncertainty

A non-closure uncertainty is added to take into account any residual differences in the background-only fit to the $VR(t)$ region and the data in this region. This additional uncertainty is necessary to ensure closure in the background-only fit and the data in this region. The non-closure uncertainty is estimated in each timing bin in every pointing category. The signal contamination in this region is negligible as demonstrated in Section 10.2.1 and the background-only fit should agree with the data in this region. The comparison between the data and background-only fit before the non-closure uncertainty is shown in Figure 9.1. The residual differences between the data and background-only fit after considering the statistical uncertainty are taken as non-closure uncertainties in each timing bin.

Pointing category	0-0.2 ns	0.2-0.4 ns	0.4-0.6 ns	0.6-0.8 ns	0.8-1 ns	1-1.5 ns	1.5-12 ns
0-50 mm, 1γ	0	0.00011	0.0047	0.017	0	0.074	0.86
50-100 mm, 1γ	0	0	0	0	0.12	0	0
100-200 mm, 1γ	0	0	0	0	0	0	0
250-300 mm, 1γ	0	0	0	0	0.087	0	0
300-2000 mm, 1γ	0	0	0	0.0020	0	0	0
Pointing category	0-0.2 ns	0.2-0.4 ns	0.4-0.6 ns	0.6-0.8 ns	0.8-1 ns	1-12 ns	
0-50 mm, $\geq 2\gamma$	0	0	0	0	0	0	
50-100 mm, $\geq 2\gamma$	0	0.0040	0.25	0	0	0	
100-200 mm, $\geq 2\gamma$	0	0	0	0	0	0	
200-300 mm, $\geq 2\gamma$	0	0.080	0	0	0	0	
300-2000 mm, $\geq 2\gamma$	0	0	0	0	0	0	

Table 9.5: Relative non-closure uncertainties in each timing bin for the high- Δm analysis. Each column corresponds to a timing bin, and each row corresponds to a pointing category.

The final non-closure uncertainties in each timing bin for every pointing category for the high- Δm and low- Δm analysis are shown in Table 9.5 and 9.6 respectively. Most of the timing bins have no non-closure uncertainty assigned, as the background-only fit agrees with the $VR(t)$ data for these bins.

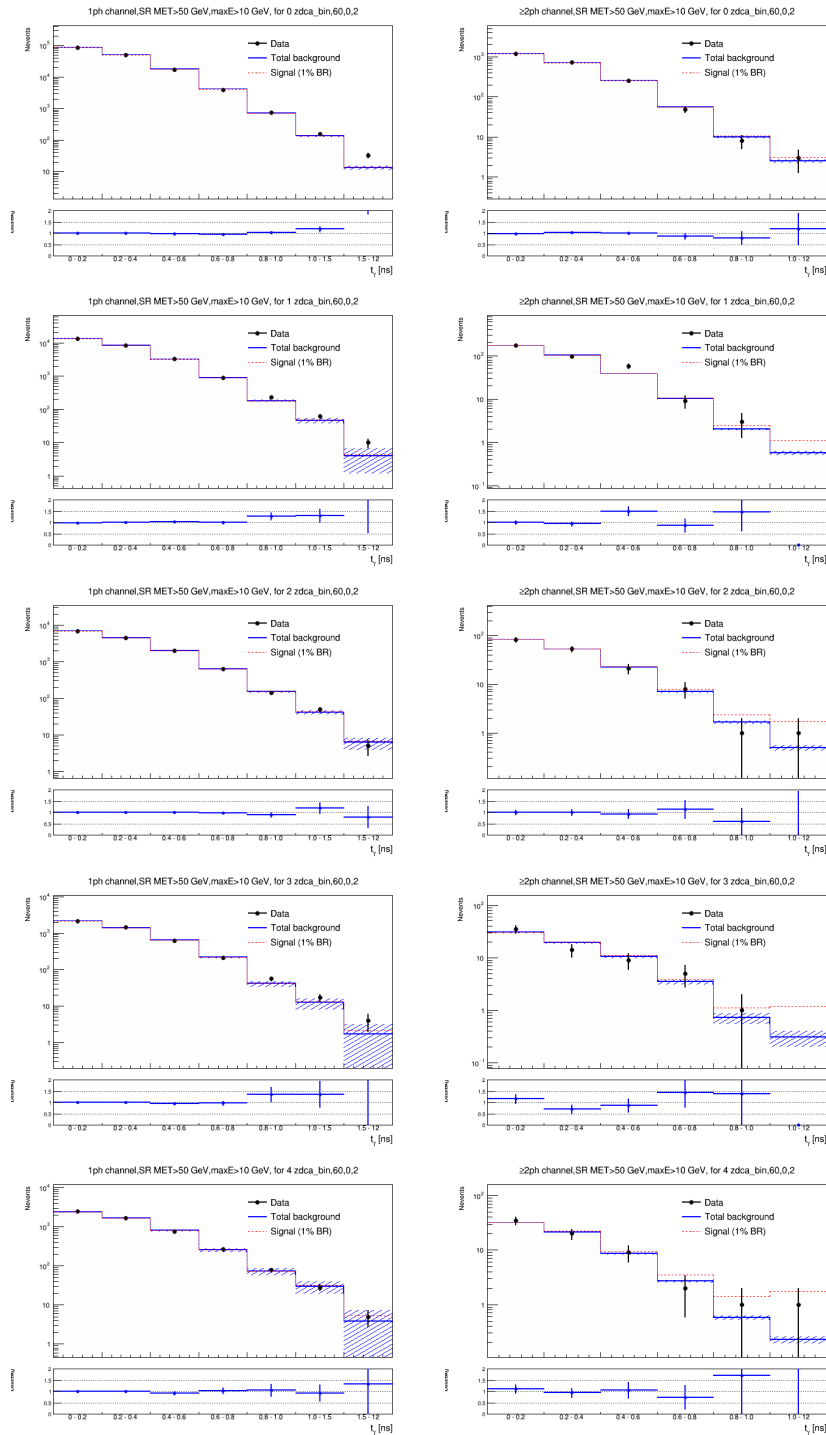


Figure 9.1: Plots comparing the high- Δm VR(t) region data (black) against the background-only fit without non-closure uncertainties for the 1γ channel (left) and the $\geq 2\gamma$ channel (right). Ratio of data to each of the background estimation is available in the bottom pane.

Pointing category	0-0.2 ns	0.2-0.4 ns	0.4-0.6 ns	0.6-0.8 ns	0.8-1 ns	1-1.5 ns	1.5-12 ns
0-50 mm, 1γ	0.042	0	0.096	0.20	0.32	0.27	0.99
50-100 mm, 1γ	0.0040	0	0	0.075	0.059	0.022	0
100-200 mm, 1ph	0	0	0	0	0.058	0.035	0
200-300 mm, 1γ	0.0043	0	0.0034	0	0	0	0
300-2000 mm, 1γ	0	0	0	0	0.090	0.17	0
Pointing category	0-0.2 ns	0.2-0.4 ns	0.4-0.6 ns	0.6-0.8 ns	0.8-1 ns	1-12 ns	
0-50 mm, $\geq 2\gamma$	0	0	0	0.044	0	0.31	
50-100 mm, $\geq 2\gamma$	0	0.044	0	0	0	0.19	
100-200 mm, $\geq 2\gamma$	0	0	0	0	0	0.19	
200-300 mm, $\geq 2\gamma$	0	0	0	0	0	0.19	
300-2000 mm, $\geq 2\gamma$	0	0	0	0	0	0.19	

Table 9.6: Relative non-closure uncertainties in each timing bin for the low- Δm analysis. Each column corresponds to a timing bin, and each row corresponds to a pointing category.

9.2 Signal systematic uncertainties

Several systematic uncertainties related to the signal Monte Carlo samples and the signal timing and pointing are studied here. Note that the statistical uncertainty on signal is directly obtained from the simulated signal samples and is the largest uncertainty on the simulated samples.

9.2.1 Theoretical uncertainties

The theoretical uncertainties for the simulated signal samples related to the factorization scale, renormalization scales and the parton distribution functions (PDFs) are calculated and applied.

The scales used in the analysis are varied separately by factors of 0.5 and 2.0 compared to their nominal values of 1.0. The maximum difference between the nominal yield and the yields from these scale variations is considered to be the scale uncertainty. Similarly, the uncertainty due to the variations in the parton distribution functions is also considered.

The variations at the generator level for each production mode and the resulting uncertainty in the yield in the Signal Region for $(m_{NLSP} \text{ (GeV)}, m_{LSP} \text{ (GeV)}, \tau \text{ (ns)}) = (60, 0.5, 2)$ signal point are given in Table 9.7. The uncertainties due to the PDF and scale variations are combined in quadrature and propagated to different signal points and the resulting total uncertainty on the signal yield in the SR is evaluated. The uncertainty on the signal yield for the high-mass splitting analysis and the low-mass splitting analysis is around 17%. This total uncertainty is included as a single nuisance parameter in the fit.

9.2.2 Experimental systematics

The following experimental uncertainties are applied to the signal normalization. The instrumental uncertainties arise from different types of experimental variations related to the photon, lepton reconstruction efficiencies, E_T^{miss} reconstruction, integrated luminosity measurement. The uncertainty on the integrated luminosity for the Run-2 data is 1.7% [80] and is applied to the signal normalization. This uncertainty is included as a single nuisance parameter and is correlated in all the pointing categories. The other experimental uncertainties on the total event yield for each signal point are determined in the 1γ and $\geq 2\gamma$ channels separately. Breakdown of various uncertainties for one signal point $(m_{NLSP}, m_{LSP}, \tau) = (60, 0.5, 2)$ is shown in Table 9.8. Note that the muon trigger related systematics are found to have negligible impact on the total event yield. Each of these uncertainties is considered uncorrelated and added in quadrature to obtain the total uncertainty. A summary of the total uncertainty for all signal points is shown in Table 9.9. The impact of these uncertainties on the 95% CL limit is found to be minimal ($<1\%$) across the signal grid.

9.2.3 Prompt-photon identification uncertainty

Prompt-photon identification, efficiency and scale factors that take into account the differences between data and Monte Carlo signal samples are described in Section 5.2.1.1. The systematic uncertainties on the total signal yield in the 1γ and $\geq 2\gamma$ channel due to this scale factor are shown in Table 9.10 for all signal points. The largest such uncertainty is 1.8% and the impact on the sensitivity due to this uncertainty is negligible ($<1\%$).

9.2.4 Non-pointing photon identification uncertainty

The non-pointing photon identification and efficiency is described in detail in Section 6.1.1. Scale factors and uncertainties that depend on photon pointing are applied to the simulated signal points. The impact depends on the signal photon pointing and is shown for signal point $(60, 0.5, 2)$ in Figure 9.2. The maximum uncertainty is around 10% in the last photon pointing bin. Such uncertainties are determined and applied to the signal normalization in each photon pointing category for every signal point.

9.2.5 Pointing related uncertainties

Signal photon pointing shape dependence is studied as a function of pileup observed in the data. Due to low signal statistics, this systematic is studied by adding all the signal points and comparing the cumulative photon pointing distribution in the nominal, low- μ and high- μ pileup conditions to determine the maximum variations to be applied. The effect of the uncertainty across all the pointing bins is shown in Figure 9.3. The 1γ channel shows good agreement between the low- μ and high- μ pointing distributions while the $\geq 2\gamma$ channel

Production mode	PDF variation (%)	Scale variation (%)	Total uncertainty (%)
WH	1.5	2.7	3.1
ZH	1.5	2.4	2.8
ttH	1.6	30	16

Table 9.7: PDF variation and scale variation for each production mode at generator level. The total uncertainty on the predicted signal yield in SR for $(m_{NLSP} \text{ (GeV)}, m_{LSP} \text{ (GeV)}, \tau \text{ (ns)}) = (60, 0.5, 2)$ signal point due to the combined PDF and scale variation are given in the last column. Once these production modes are weighted by their cross section, the impact on the signal yield in SR for 60,0,2 signal point is around 17%.

Systematic	1γ up(%)	1γ down(%)	$\geq 2\gamma$ up(%)	$\geq 2\gamma$ down(%)
e/ γ resolution	-0.0757	0.0163	-0.1531	0.3326
e/ γ scale variation	-0.2416	-0.1073	0.8533	-0.6288
μ isolation statistics	0.1262	-0.5830	0.1242	-0.6159
μ isolation systematics	0.2034	-0.1827	0.2096	-0.1819
μ reconstruction	0.1385	-0.1385	0.1431	-0.1422
μ efficiency statistics	0.0213	-0.0214	0.0222	-0.0222
μ efficiency systematics	0.0267	-0.0246	0.0258	-0.0242
μ identification	-0.0584	-0.0067	-0.0028	0.0673
μ MS related uncertainties	0.0823	-0.0047	0.0145	-0.0338
μ tracking related uncertainties	0.0004	0.0004	0.0000	0.0272
μ scale variation	-0.0237	0.0372	-0.0093	0.0269
e identification efficiency	0.3410	-0.3404	0.3040	-0.3037
e isolation systematics	0.0235	-0.0235	0.0174	-0.0174
e reconstruction	0.0699	-0.0699	0.0634	-0.0634
e trigger efficiency	0.0001	-0.0001	0.0000	-0.0000
e trigger	0.0823	-0.0823	0.0770	-0.0770
E_T^{miss} resolution	-0.7479	-0.7479	-0.0899	-0.0899
E_T^{miss} perpendicular resolution	-0.3325	-0.3325	0.3150	0.3150
E_T^{miss} scale	-0.3572	0.0760	0.0451	0.1317

Table 9.8: Up and down experimental uncertainties related to electron, muon, E_T^{miss} , e/ γ scale and resolution uncertainties for $(m_{NLSP}, m_{LSP}, \tau) = (60, 0.5, 2)$ in the 1γ and $\geq 2\gamma$ channels.

Signal point	1γ up(%)	1γ down(%)	$\geq 2\gamma$ up(%)	$\geq 2\gamma$ down(%)
30,0.5,2	0.8976	1.1248	1.7354	1.3212
30,0.5,10	1.8743	1.8273	5.2496	3.3563
30,10,2	1.0886	1.1955	0.8127	1.1315
30,10,10	0.7413	1.2422	2.8041	2.9418
30,20,2	1.0609	1.2301	2.2978	1.5612
30,20,10	0.9129	1.1998	0.4600	6.9142
40,0.5,2	1.2652	1.3309	0.9688	0.9680
40,0.5,10	1.0854	1.8231	1.8558	1.9328
40,10,2	0.8242	1.0002	1.2993	1.1979
40,10,10	0.9388	0.9212	3.8438	3.1647
40,20,2	1.0239	1.2495	1.9616	1.7563
40,20,10	1.7058	1.7465	3.8228	3.9436
40,30,2	1.0276	1.2897	2.0206	2.4505
40,30,10	1.1670	2.0812	5.2568	4.4529
50,0.5,2	0.8870	0.9002	1.1145	1.0498
50,0.5,10	1.0388	1.0938	2.5465	2.5672
50,10,2	0.6612	0.8480	1.1230	1.1174
50,10,10	0.9617	1.2669	2.3155	2.8744
50,20,2	0.7501	1.0317	1.3794	1.2160
50,20,10	0.7667	1.1258	1.8204	1.2783
50,30,2	1.3467	1.2920	1.5181	2.5479
50,30,10	0.6282	0.8803	1.9654	1.5110
50,40,2	1.1358	1.0403	1.4871	2.2509
50,40,10	0.6527	0.9115	4.4983	6.1468
60,0.5,2	1.0385	1.1002	1.0222	1.0835
60,0.5,10	0.8198	0.9598	1.1569	1.0629
60,10,2	0.7214	0.8007	0.9307	0.9833
60,10,10	1.0634	1.1853	4.1294	3.5456
60,20,2	0.8075	0.8179	1.1742	1.2599
60,20,10	0.8558	1.3810	1.7361	1.9278
60,30,2	0.5754	0.7346	0.7577	0.8192
60,30,10	0.6643	1.2395	1.0464	1.2954
60,40,2	0.8025	1.0467	0.9593	1.0462
60,40,10	0.9983	1.1979	0.8966	1.2287
60,50,2	1.0067	0.9575	2.1071	1.3599
60,50,10	0.9113	1.6053	14.8767	9.7937

Table 9.9: Up and down experimental uncertainties for various signal points in the 1γ and $\geq 2\gamma$ channel.

m_{NLSP} [GeV]	m_{LSP} [GeV]	τ [ns]	1γ uncertainty (%)	$\geq 2\gamma$ uncertainty (%)
30	0.5	2	0.27	0.99
30	0.5	10	0.29	1.0
30	10	2	0.29	1.1
30	10	10	0.33	1.2
30	20	2	0.51	1.5
30	20	10	0.56	1.5
40	0.5	2	0.27	0.97
40	0.5	10	0.29	1.1
40	10	2	0.27	0.97
40	10	10	0.30	1.1
40	20	2	0.33	1.1
40	20	10	0.38	1.3
40	30	2	0.58	1.5
40	30	10	0.59	1.6
50	0.5	2	0.26	0.91
50	0.5	10	0.27	0.99
50	10	2	0.27	0.92
50	10	10	0.27	1.0
50	20	2	0.29	1.0
50	20	10	0.31	1.1
50	30	2	0.35	1.2
50	30	10	0.39	1.2
50	40	2	0.62	1.6
50	40	10	0.69	1.7
60	0.5	2	0.27	0.81
60	0.5	10	0.26	0.92
60	10	2	0.27	0.85
60	10	10	0.26	0.94
60	20	2	0.29	0.92
60	20	10	0.28	0.96
60	30	2	0.33	0.97
60	30	10	0.32	1.1
60	40	2	0.40	1.2
60	40	10	0.42	1.3
60	50	2	0.74	1.7
60	50	10	0.74	1.8

Table 9.10: Relative uncertainty on the signal yield due to prompt photon identification scale factor in the 1γ and $\geq 2\gamma$ channel for different signal points.

has a maximum uncertainty of 1.7% which is negligible compared to the other uncertainties on the signal.

9.2.6 Timing smearing uncertainty

The timing resolution uncertainty is assigned to the Monte Carlo signal samples to account for the difference in the photon timing distribution between data and the simulated samples. This resolution uncertainty is fully correlated between different pointing categories and timing bins, hence it is included as a single nuisance parameter in the statistical fit. The estimation of this uncertainty is performed by using alternate smearing of the signal photon timing. The resulting up and down variations in the photon timing for the (60,0.5,2) signal point for the 1γ channel and lowest pointing category is shown in Figure 9.4. The uncertainty is negligible and the impact on the final limits is $<1\%$.

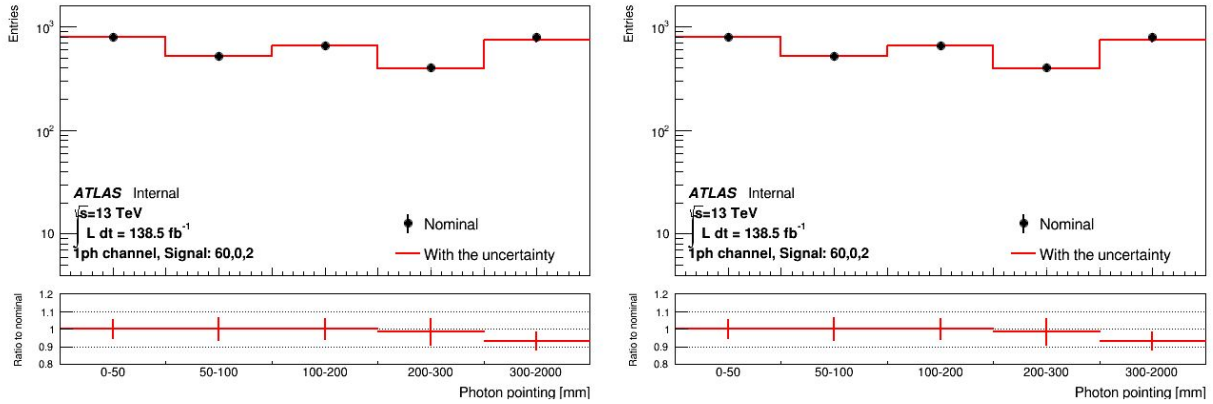


Figure 9.2: Signal yield for (60,0.5,2) signal point in different pointing categories with (red) and without (black) the non-pointing photon identification.

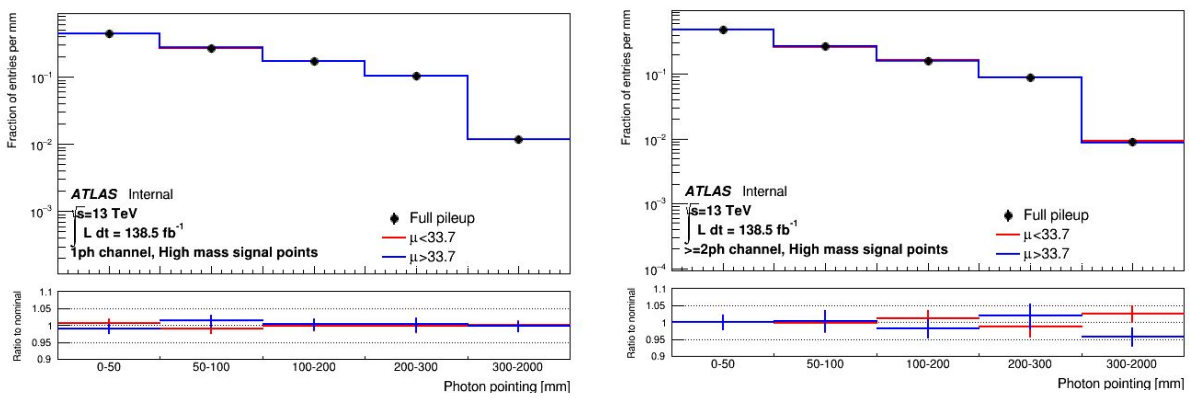


Figure 9.3: Comparison of pointing shapes for all signal points in the low-pileup (red) and high-pileup (blue) conditions to the nominal full pileup condition (black) in both the 1γ (left) and $\geq 2\gamma$ channel (right).

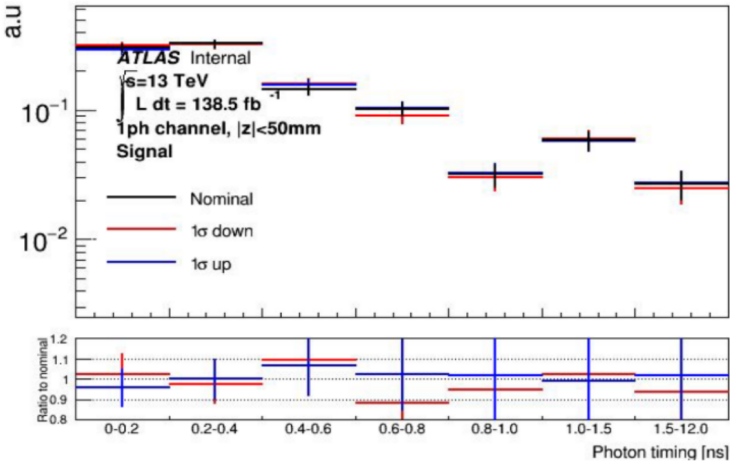


Figure 9.4: Nominal timing distribution for signal point (60,0.5,2) in black compared against the up (blue) and down (red) variations for 1 γ channel and lowest pointing category.

Chapter 10

Statistical analysis and background validation

10.1 Statistical analysis

A binned-likelihood fit is performed to the timing distributions of the data simultaneously in all the 10 pointing categories to test the background-only and signal-plus-background hypotheses. The details of the ten pointing categories and the bin boundaries for the timing distribution are available in Chapter 7.

A simultaneous likelihood fit is performed in all the categories using

$$L = \prod_i F_i(t_i, \alpha_i) \quad (10.1)$$

where i is the category index for each of the 10 pointing categories, $F_i(t_i, \alpha_i)$ is the likelihood function in the category i which includes the timing PDFs for the background which depend on the mixing fraction, α_i , in the category i and the signal. The timing PDF in each category is given in Equation 8.1. The fits of the individual categories is performed simultaneously and the signal strength parameter, $\mu = \text{BR}(H \rightarrow \text{NLSP NLSP})$ is a free parameter in the fit and is correlated among the different categories. The background normalization in each category is treated as an independent, unconstrained nuisance parameter in the fit which will be determined by the number of observed events in the category. The mixing fraction or purity is also a free parameter in the fit in categories where the real-enhanced and fake-enhanced templates are distinguishable as explained in Section 8.3, and in others it is fixed at 0.5. All the systematic uncertainties described in Chapter 9 are included as nuisance parameters in the fit. A summary description and the notation for the different nuisance parameters is given in Table 10.1.

Description	Notation	Total number of nuisance parameters of this type in the fit
Statistical uncertainty on genuine photon template in each timing bin	STAT_genuine_NPP_px_ty_cz	65
Statistical uncertainty on fake photon template in each timing bin	STAT_fake_NPP_px_ty_cz	65
Correlated shape systematics for genuine template in each pointing category	SHAPE_gen_corr_px_cz	10
Correlated shape systematics for fake template in each pointing category	SHAPE_fake_corr_px_cz	10
Nonclosure uncertainty in each timing bin	SHAPE_bkg_corr_NPP_px_ty_cz	65
Statistical uncertainty on signal photon template in each timing bin	STAT_sig_NPP_px_ty_cz	65
Experimental uncertainty on the total signal yield	EXP_signal_uncertainty	1
Prompt photon identification uncertainty on the total signal yield	PromptID_signal_uncertainty	1
Loose photon identification correlated for different pointing categories	PointingID_signal_uncertainty	1
Timing smearing uncertainty on the signal timing	Timesmear_signal_uncertainty	1
Luminosity uncertainty	ATLAS_lumi_run2	1
Theory uncertainty	ATLAS_signal_eff	1

Table 10.1: Description of different nuisance parameters and the notations used for these in the pull plots where px defines the pointing category where p0: $0 < |z_{DCA}| < 50$ mm, p1: $50 < |z_{DCA}| < 100$ mm, p2: $100 < |z_{DCA}| < 200$ mm, p3: $200 < |z_{DCA}| < 300$ mm, p4: $300 < |z_{DCA}| < 2000$ mm. The photon channel is given by cy where c0: 1γ channel and c1: $\geq 2\gamma$ channel. Timing bin is denoted by ty and for the 1γ channel, it ranges from 0-6 where t0: $0 < t < 0.2$ ns, t1: $0.2 < t < 0.4$ ns, t2: $0.4 < t < 0.6$ ns, t3: $0.6 < t < 0.8$ ns, t4: $0.8 < t < 1$ ns, t5: $1.0 < t < 1.5$ ns and t6: $1.5 < t < 12$ ns. Similarly, the timing bins for the $\geq 2\gamma$ channel range from 0-5 where t0: $0 < t < 0.2$ ns, t1: $0.2 < t < 0.4$ ns, t2: $0.4 < t < 0.6$ ns, t3: $0.6 < t < 0.8$ ns, t4: $0.8 < t < 1$ ns, t5: $1.0 < t < 12$ ns.

10.2 Background estimation validation

A background-only fit is performed using the background-only part of the PDF applied in the validation region $\text{VR}(t)$ and $\text{VR}(E_T^{miss})$ regions for both the high- Δm and low- Δm analysis. The goal is to determine how well the background-only fit describes the data in each of these regions. The real-enhanced and fake-enhanced photon timing templates are reweighted in the E_{cell} variable to each of the VR and mean shifted. The KS-test is performed in each pointing category to determine if the mixing fraction needs to be fixed, the resulting templates are used in the PDF fit.

10.2.1 High- Δm $\text{VR}(t)$ region

This region can be used as a validation region as the signal contamination in this region is negligible. The data yields in this region as a function of photon pointing and timing for each channel is available in Figure 10.1. Comparing the uncertainty on the data yields in each bin to the signal yields for the (60,0.5,2) signal point shown in Figure 10.2, it can be seen that the signal yield is less than the uncertainty associated with the data yields, verifying that the signal contamination in this region is negligible.

The data and background-only fit comparison in each pointing category is shown in Figure 10.3 for the high- Δm analysis. In each of the pointing category, the data agrees with the background-only fit. A summary of these results obtained by adding data in the five pointing categories in the 1γ ($\geq 2\gamma$) channel and comparison to the sum of background-only fit in these categories is shown in the left (right) side of Figure 10.4. Note that the fit is still performed in the 10 pointing categories simultaneously. Plots in Figure 10.4 serve as a summary of the validation in each channel.

10.2.2 Validation in low- Δm $\text{VR}(t)$ region

The data and background-only fit comparison in each pointing category is available in Figure 10.5. Summary plots comparing the data against the background-only fit in sum of the 5 pointing categories in each channel is performed for the low- Δm $\text{VR}(t)$ region and is shown in Figure 10.6. Good agreement between the data and the background fit is observed.

The goodness of the fit is also demonstrated in the post-fit nuisance parameter pull plots shown in Figure 10.7. The description and the notation for different nuisance parameters was given in Table 10.1. The pulls corresponding to the nuisance parameters with the highest impact on the fitted $\text{BR}(\text{H} \rightarrow \text{NLSP NLSP})$ are well behaved.

10.2.3 Validation in $\text{VR}(E_T^{miss})$ region

Similar agreement can be seen for the high- Δm $\text{VR}(E_T^{miss})$ and the low- Δm $\text{VR}(E_T^{miss})$ analysis in Figures 10.8 and 10.9 respectively.

10.3 Signal injection studies

Another validation test to verify the goodness of the fit framework is to add signal at a particular $\text{BR}(\text{H} \rightarrow \text{NLSP NLSP})$ to the data in the $\text{VR}(t)$ region and check if the fitted $\text{BR}(\text{H} \rightarrow \text{NLSP NLSP})$ agrees with that of the injected signal. For this study, signal from six different signal points $(60, 0.5, 2)$, $(40, 20, 2)$, $(50, 40, 2)$, $(60, 0.5, 10)$, $(40, 20, 10)$ and $(50, 40, 10)$ is injected on top of the $\text{VR}(t)$ data and a signal-plus-background fit is performed to each of this artificial signal plus data timing distribution. The signal component is added at three distinct $\text{BR}(\text{H} \rightarrow \text{NLSP NLSP})$ values of 1%, 10% and 20%.

In each of these tests, the signal-plus-background fit resulted in the fitted $\text{BR}(\text{H} \rightarrow \text{NLSP NLSP})$ equal to the injected one. The agreement between the background from the signal-plus-background fit along with the injected signal at 10% $\text{BR}(\text{H} \rightarrow \text{NLSP NLSP})$ for the $(60, 0.5, 2)$ signal point overlaid on top of it is shown against the data-plus-injected signal for the last pointing category in each channel is shown in Figure 10.10. It is clear that the fitted background along with the 10% signal component agrees with the data-plus-injected signal distribution, thus validating this study. The fitted $\text{BR}(\text{H} \rightarrow \text{NLSP NLSP})$ values from signal-plus-background fits for each injected $\text{BR}(\text{H} \rightarrow \text{NLSP NLSP})$ for different signal points is shown in Figure 10.11. It can be seen that the difference of the fitted $\text{BR}(\text{H} \rightarrow \text{NLSP NLSP})$ values from this signal-plus-background fits to the data plus injected signal to that of the fitted $\text{BR}(\text{H} \rightarrow \text{NLSP NLSP})$ values for signal-plus-background fits to only the data in $\text{VR}(t)$ region is in excellent agreement with the injected $\text{BR}(\text{H} \rightarrow \text{NLSP NLSP})$ values.

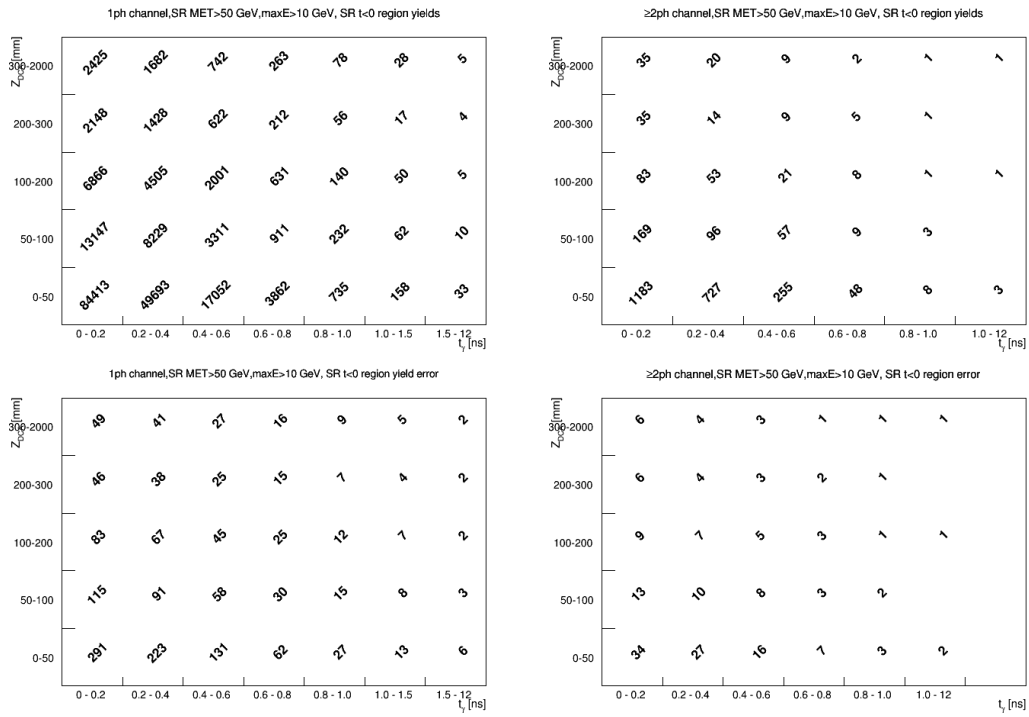


Figure 10.1: The data yields in the high- Δm VR(t) region in two dimensions of photon pointing and timing for the 1γ channel (left) and the $\geq 2\gamma$ channel (right) in the first row. Similar plots are available in the second row for the uncertainties on these data yields. The X-axis corresponds to the photon timing and the Y-axis corresponds to the photon pointing.

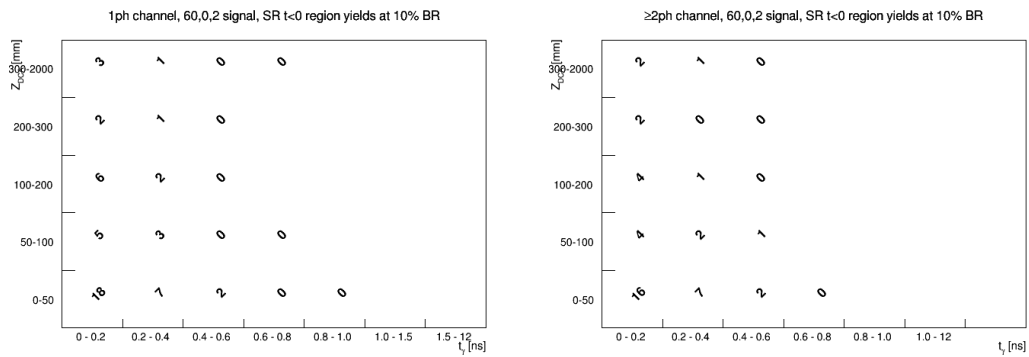


Figure 10.2: The signal yields for the (60,0.5,2) signal point in the high- Δm VR(t) region in two dimensions of photon pointing and timing for the 1γ channel (left) and the $\geq 2\gamma$ channel (right). The X-axis corresponds to the photon timing and the Y-axis corresponds to the photon pointing.

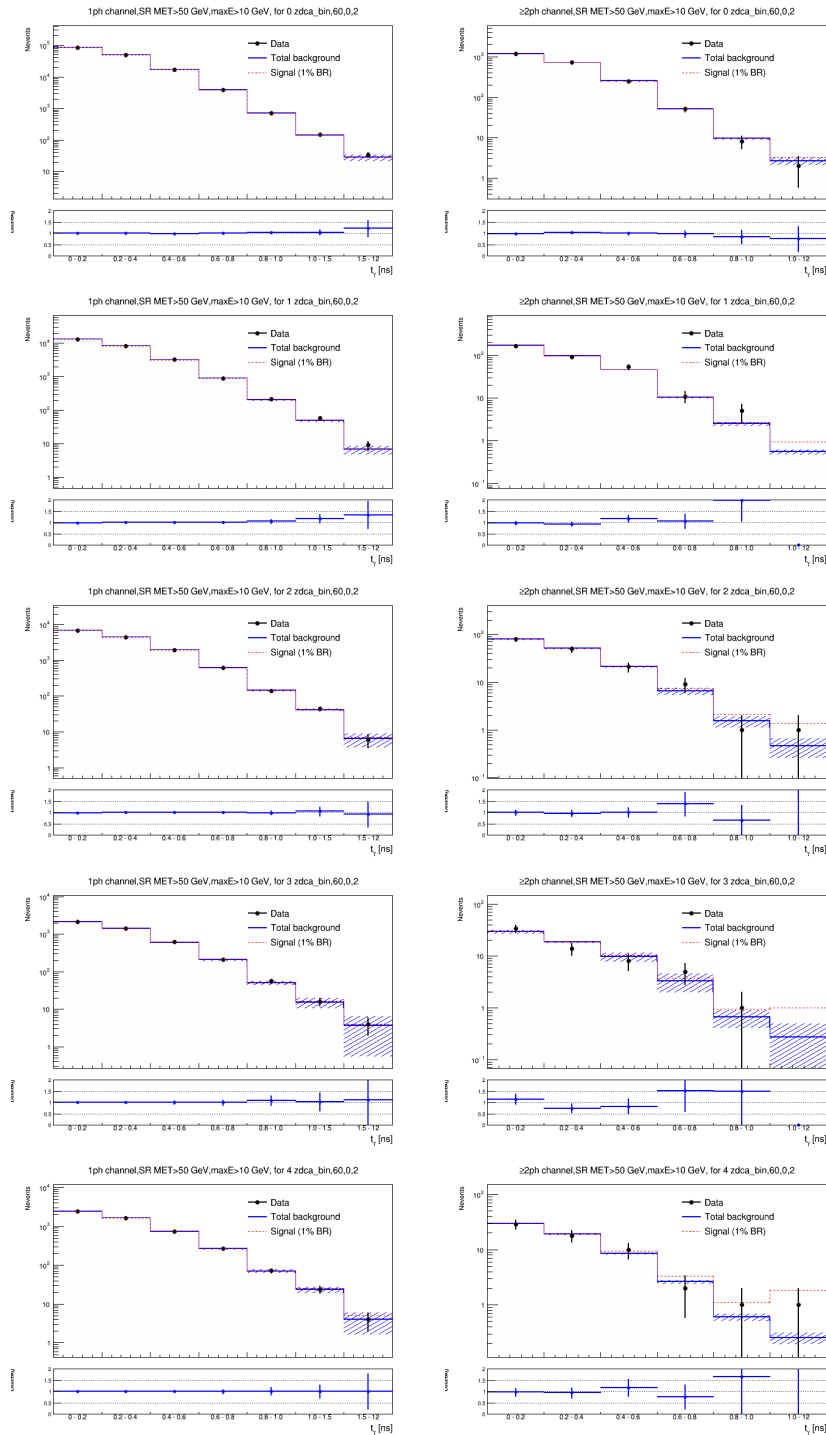


Figure 10.3: Timing distribution for data and background-only fit in the high- Δm VR(t) region for different pointing categories in the 1γ channel (left) and the $\geq 2\gamma$ channel (right).

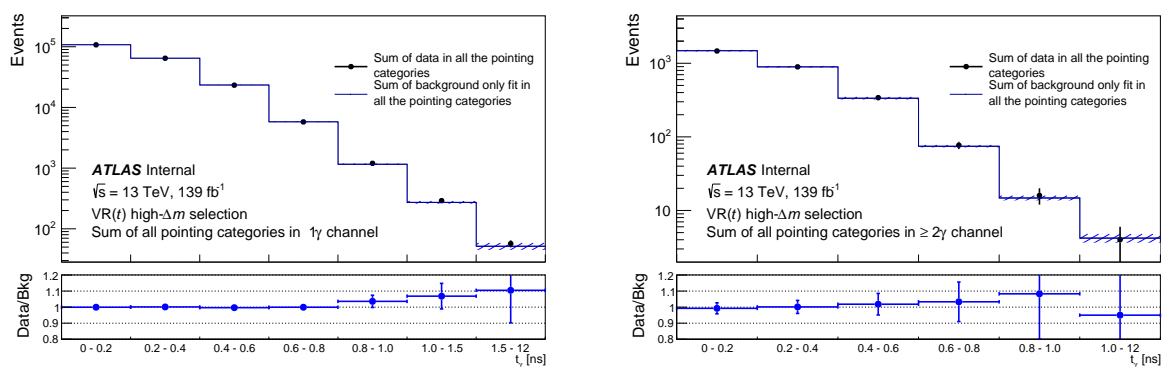


Figure 10.4: Comparison of the sum of the timing distribution in 5 pointing categories for data and background-only fits for the 1γ channel (left) and the $\geq 2\gamma$ channel on the right for the high- Δm VR(t) region. Note that the fit is still performed simultaneously in the 10 pointing categories, the sum of the timing distributions shown here are for display purposes only.

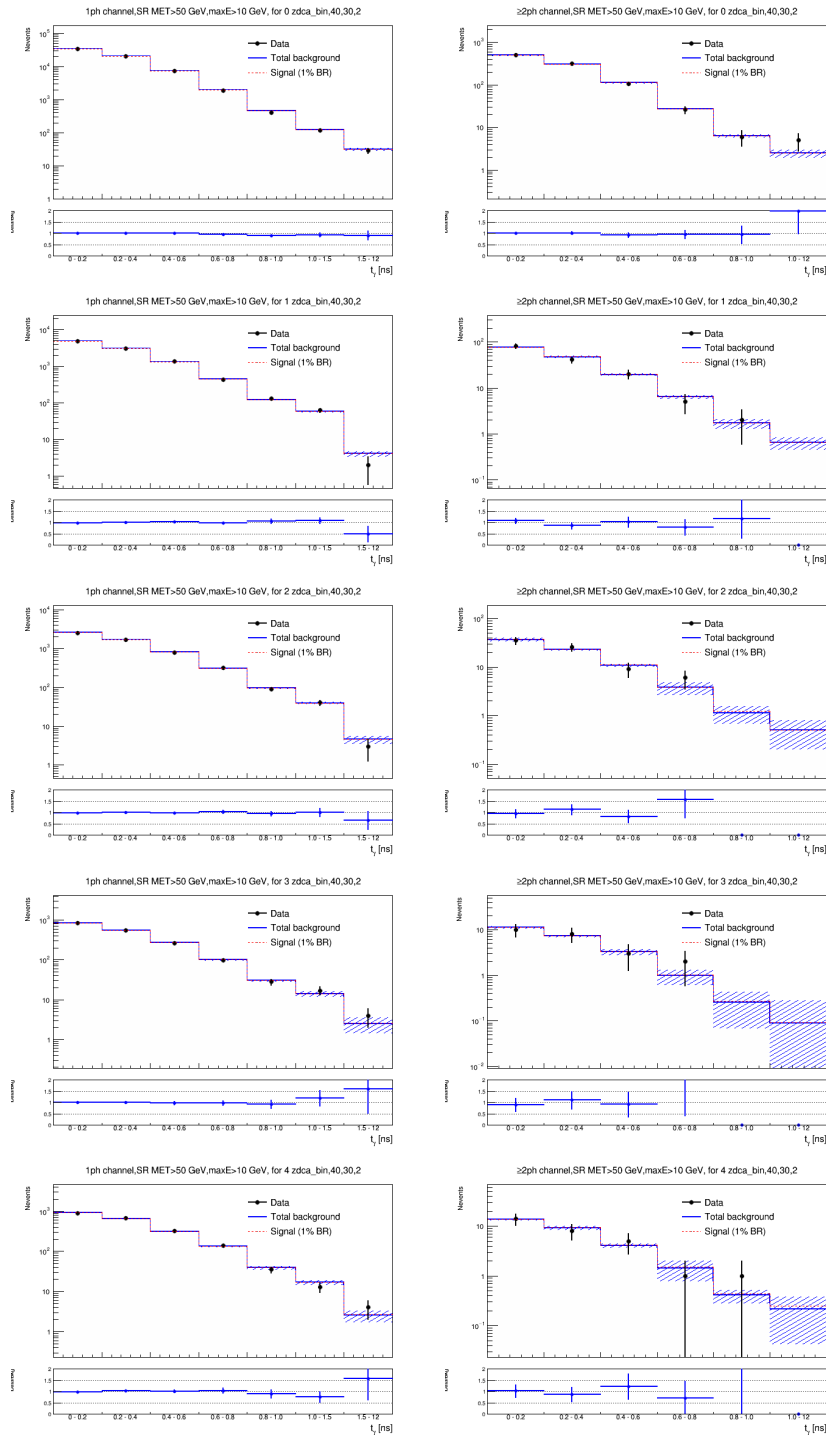


Figure 10.5: Timing distribution for data and background-only fit in the high- Δm VR(t) region for different pointing categories in the 1 γ channel (left) and the $\geq 2\gamma$ channel (right).

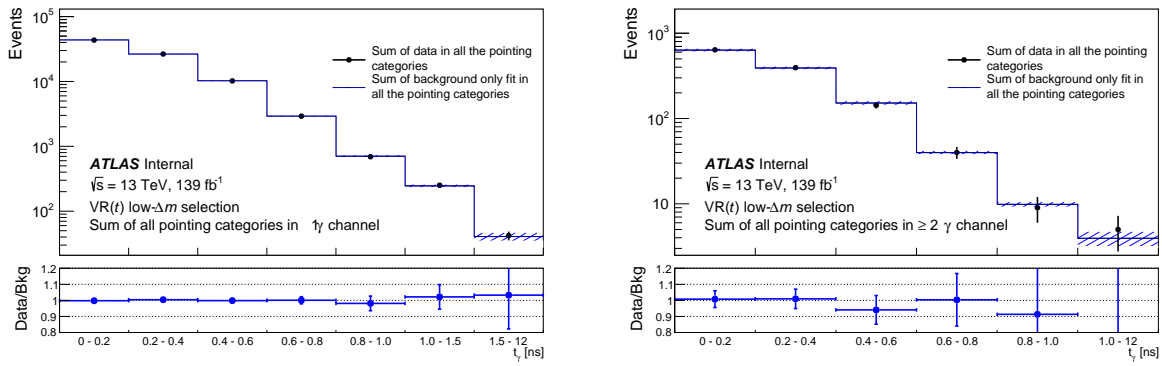


Figure 10.6: Comparison of the sum of the timing distribution in 5 pointing categories for data and background-only fits for the 1γ channel (left) and the $\geq 2\gamma$ channel (right) for the low- Δm VR(t) region. Note that the fit is still performed simultaneously in the 10 pointing categories, the sum of the timing distributions shown here are for display purposes only.

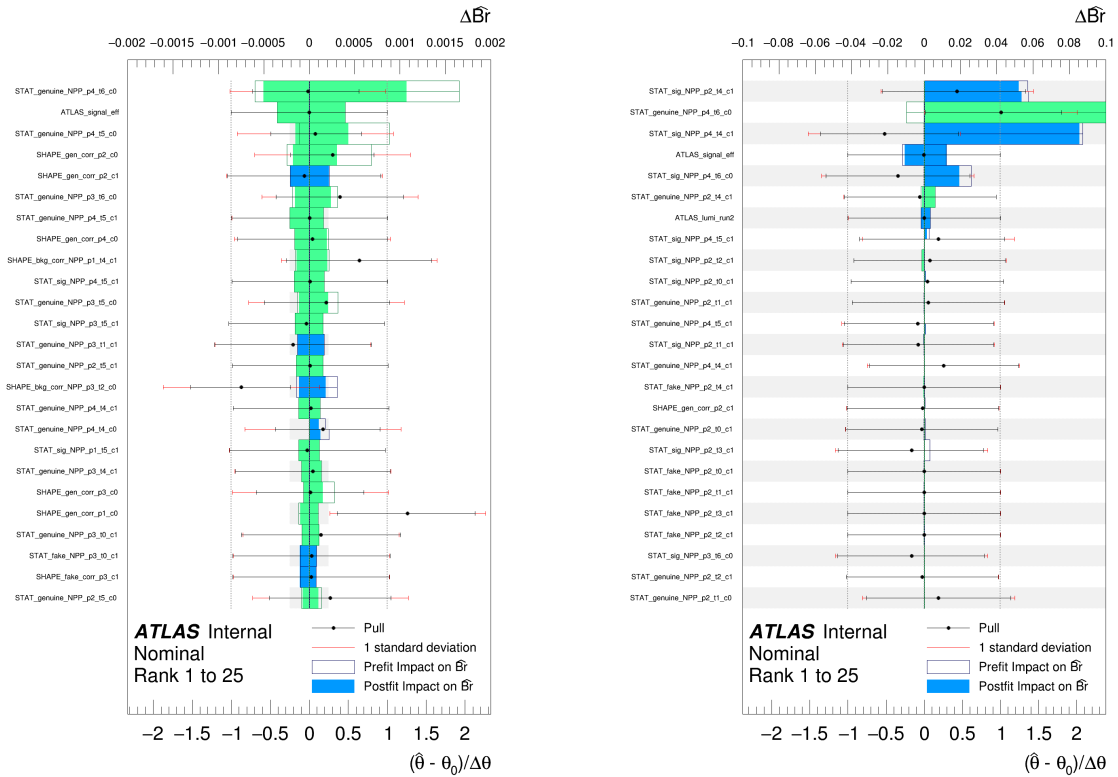


Figure 10.7: Post-fit nuisance parameter pull plots showing the top 25 nuisance parameters with maximum impact on the fitted μ . The left plot corresponds to the high- Δm VR(t) analysis using signal point $(m_{NLSP}, m_{LSP}, \tau) = (60, 0.5, 2)$ and the right plot corresponds to the low- Δm VR(t) analysis using signal point $(m_{NLSP}, m_{LSP}, \tau) = (40, 30, 2)$. The black box corresponds to the pre-fit impact on the μ . The blue band represents post-fit impact on the μ when the Br and NP change in the same direction and green band represents the same when they change in the opposite direction. The black dot is the uncertainty on the NP pull and red band corresponds to its 1σ band.

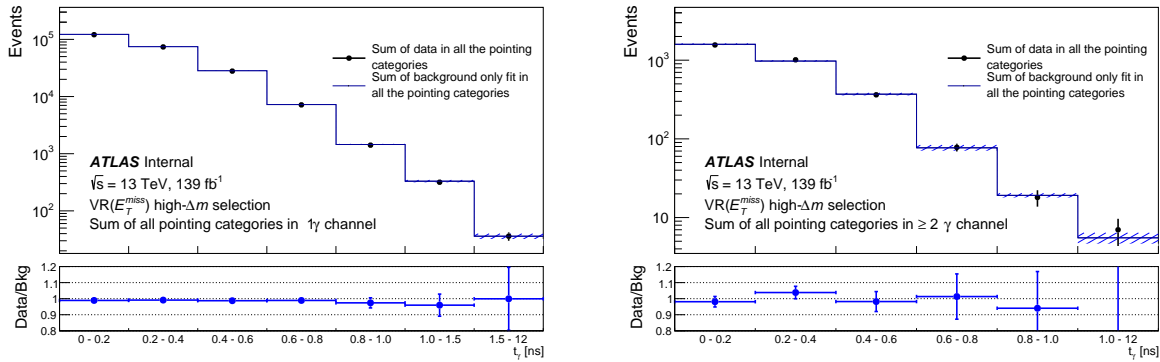


Figure 10.8: Comparison for the sum of the timing distribution in 5 pointing categories for data and background-only fits for the 1γ channel (left) and the $\geq 2\gamma$ channel (right) for the high- Δm $VR(E_T^{miss})$ region. Note that the fit is still performed simultaneously in the 10 pointing categories, the sum of the timing distributions shown here are for display purposes only.

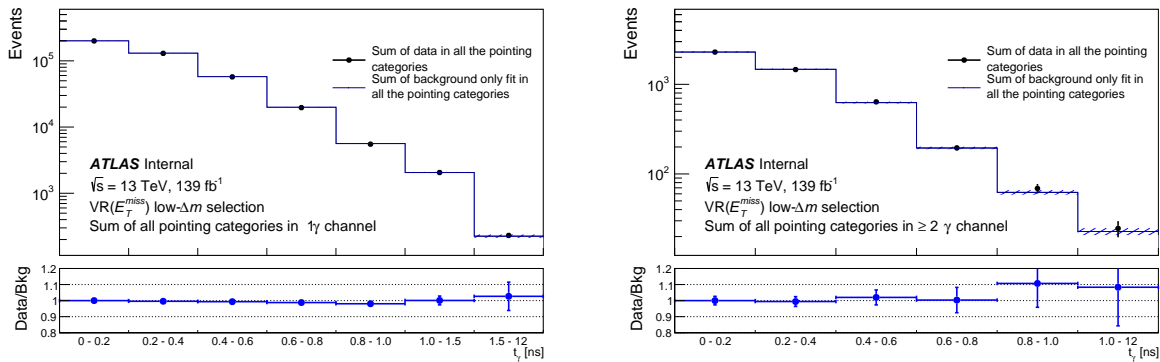


Figure 10.9: Comparison for the sum of the timing distribution in 5 pointing categories for data and background-only fits are compared for the 1γ channel (left) and the $\geq 2\gamma$ channel (right) for the low- Δm $VR(E_T^{miss})$ region. Note that the fit is still performed simultaneously in the 10 pointing categories, the sum of the timing distributions shown here are for display purposes only.

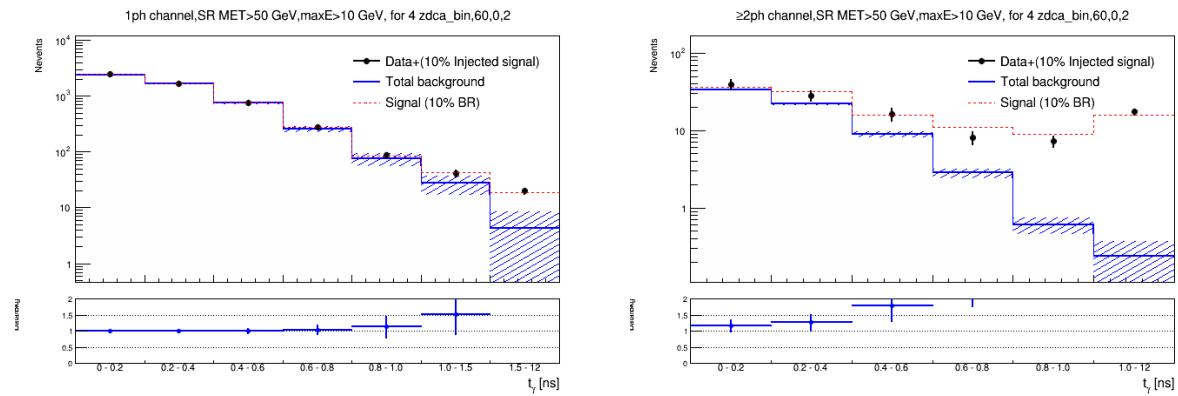


Figure 10.10: Comparison for the timing distribution for data plus injected signal from the (60,0.5,2) signal point at $\text{BR}(H \rightarrow \text{NLSP NLSP})=10\%$ (black) against fitted background from signal-plus-background (blue) along with the signal contribution at the injected BR (red) is shown in the last pointing category for the 1γ channel (left) and the $\geq 2\gamma$ channel (right) for the high- Δm $\text{VR}(E_T^{\text{miss}})$ region.

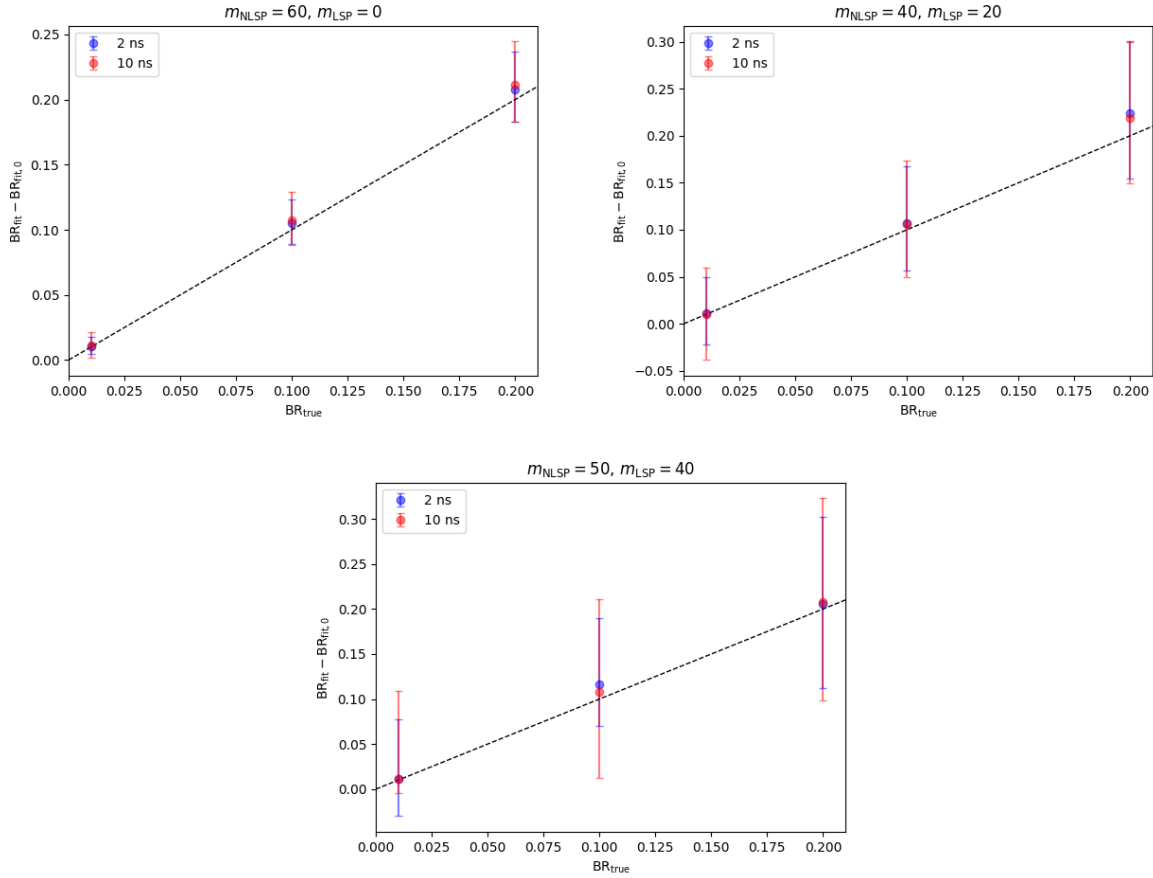


Figure 10.11: Difference between the fitted $\text{BR}(H \rightarrow \text{NLSP NLSP})$ values from the signal-plus-background fit to data-plus-injected signal to that of the fitted $\text{BR}(H \rightarrow \text{NLSP NLSP})$ values for signal-plus-background fits to only the data in $\text{VR}(t)$ region at different injected $\text{BR}(H \rightarrow \text{NLSP NLSP})$ values for $(m_{\text{NLSP}}, m_{\text{LSP}}) = (60, 0.5)$ in the top left plot, for $(40, 20)$ on the top right plot and $(50, 40)$ in the bottom plot. Note that the high- Δm analysis selections are used in the first row while the low- Δm analysis selections are used in the bottom row. Each plot shows the results for both lifetimes of 2 and 10 ns.

Chapter 11

Results

A likelihood-based fit to the timing distribution is performed simultaneously in the 10 different pointing categories using the background-only hypothesis to fit the data in the signal region. The mixing fractions or purity of the real-enhanced and the fake-enhanced templates from this fit are presented in Tables 11.1 and 11.2 for the high- Δm and low- Δm analysis respectively. The purity for the two pointing categories where the real-enhanced and fake-enhanced timing templates are indistinguishable in the high mass analysis following the prescription from Chapter 8.

The comparison between the data and fitted background using this background-only fit in the signal region is presented in Figures 11.1 and 11.2 for the high- Δm and low- Δm analysis respectively. The estimated background agrees very well with the data. No significant excess

Pointing category	Purity	error
0-50mm, 1γ	0.826	0.080
50-100mm, 1γ	0.500	
100-200mm, 1γ	0.891	0.179
200-300mm, 1γ	0.461	0.130
300-2000mm, 1γ	1.000	0.155
0-50mm, $\geq 2\gamma$	0.567	0.324
50-100mm, $\geq 2\gamma$	0.500	
100-200mm, $\geq 2\gamma$	0.00	0.984
200-300mm, $\geq 2\gamma$	1.000	0.970
300-2000mm, $\geq 2\gamma$	0.000	0.866

Table 11.1: The measured purity values for the real-enhanced and fake-enhanced timing templates in the fit to the observed data for the high- Δm analysis using the background-only fit for the ten different pointing categories.

Pointing category	Purity	error
0-50mm, 1γ	0.729	0.096
50-100mm, 1γ	1.000	0.617
100-200mm, 1γ	0.739	0.135
200-300mm, 1γ	0.427	0.138
300-2000mm, 1γ	1.000	0.921
0-50mm, $\geq 2\gamma$	0.963	0.963
50-100mm, $\geq 2\gamma$	1.000	0.713
100-200mm, $\geq 2\gamma$	0.742	0.871
200-300mm, $\geq 2\gamma$	0.380	0.690
300-2000mm, $\geq 2\gamma$	1.000	0.949

Table 11.2: The measured purity values for the real-enhanced and fake-enhanced timing templates in the fit to the observed data for the low- Δm analysis using background-only fit for the ten different pointing categories.

is observed. The maximum excess is around 0.84σ (1.2σ) for the high- Δm (low- Δm) analysis.

The post-fit nuisance parameter pull plots showing the top 25 nuisance parameters with the maximum impact on the fitted branching ratio for the signal-plus-background fits to the signal region can be found in Figure 11.3. The nuisance parameter pulls corresponding to the nuisance parameters with the highest impact on the fitted μ are well behaved, within $\pm 1\sigma$.

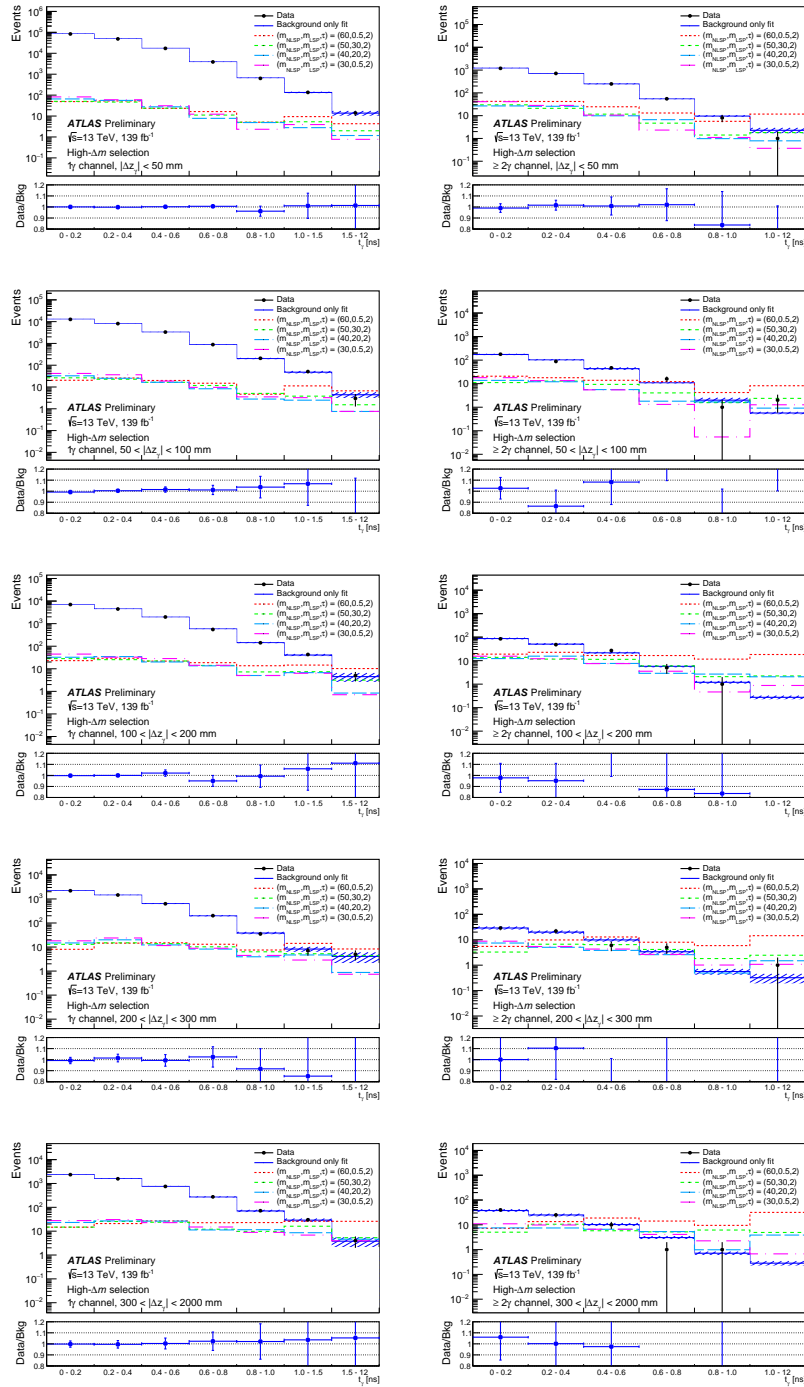


Figure 11.1: Timing distributions for the data and the estimated background, as determined by the background-only fit, for the high- Δm selection in different pointing categories for the 1γ ($\geq 2\gamma$) final state on the left (right). For comparison, the expected timing shapes for a few different signal points are superimposed, with a signal normalization corresponding to a value of $\text{BR}(H \rightarrow \text{NLSP NLSP}) = 20\%$. The signal models are labelled by their values of the NLSP and LSP masses (in GeV) and NLSP lifetime (in ns).

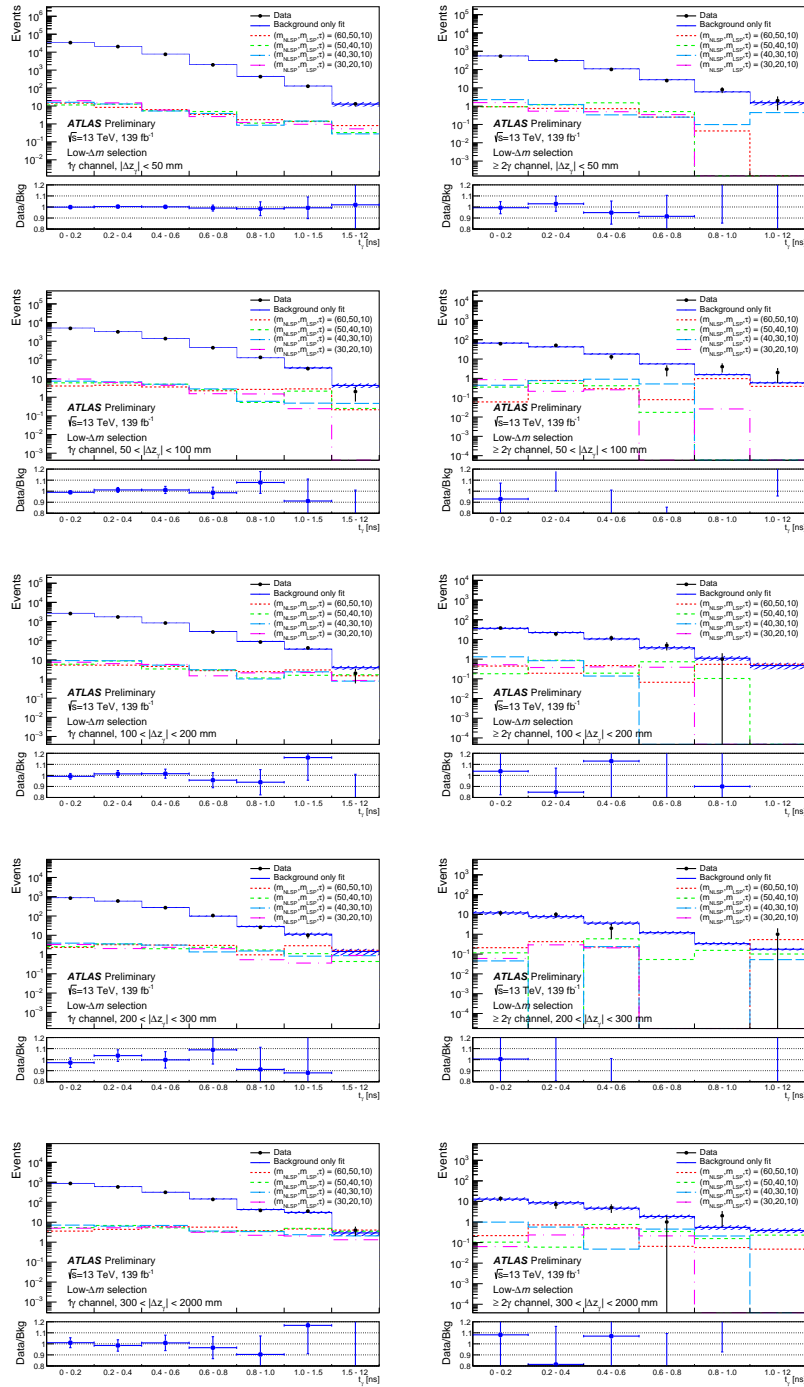


Figure 11.2: Timing distributions for data and the estimated background, as determined by the background-only fit, for the low- Δm selection in different pointing categories for the 1γ ($\geq 2\gamma$) final state on the left (right). For comparison, the expected timing shapes for a few different signal points are shown superimposed, with a signal normalization corresponding to a value of $\text{BR}(H \rightarrow \text{NLSP NLSP}) = 20\%$. The signal models are labelled by their values of the NLSP and LSP masses (in GeV) and NLSP lifetime (in ns).

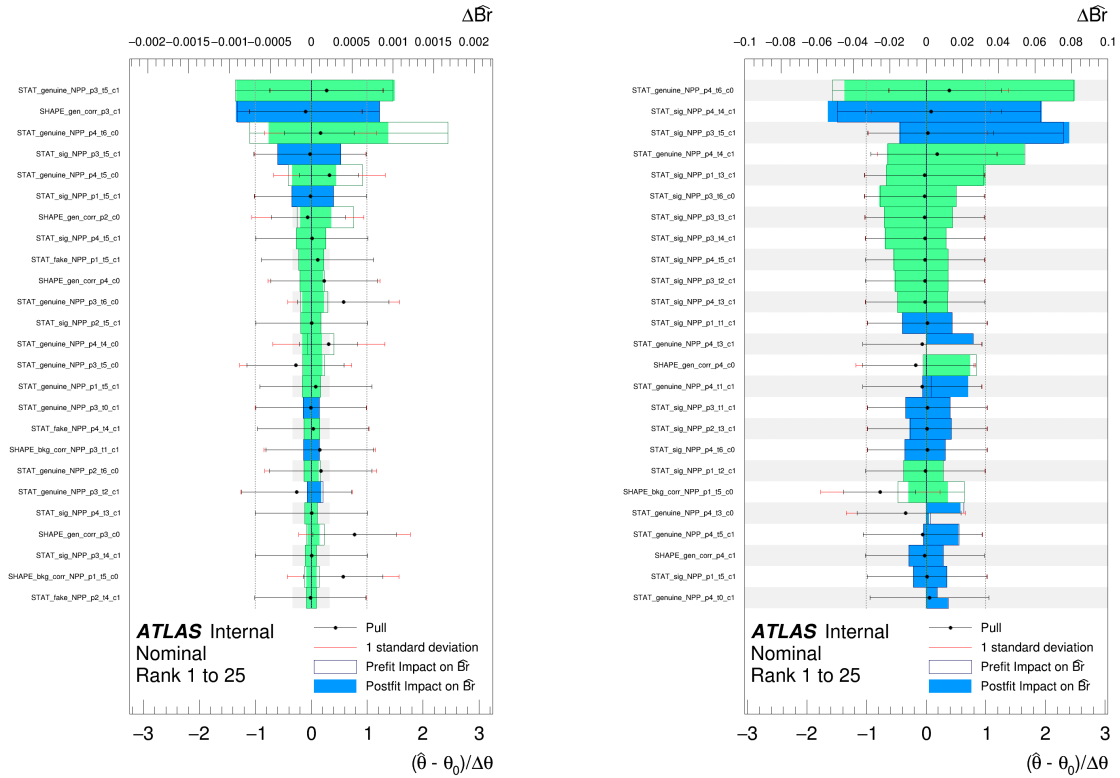


Figure 11.3: Post-fit nuisance parameter pull plots showing the top 25 nuisance parameters (NPs) with the maximum impact on the fitted μ using the signal-plus-background fit to the observed data. The left plot corresponds to the high- Δm analysis using signal point $(m_{NLSP}, m_{LSP}, \tau) = (60, 0.5, 2)$ and the right plot corresponds to the low- Δm analysis using signal point $(m_{NLSP}, m_{LSP}, \tau) = (40, 30, 2)$. The black box corresponds to the pre-fit impact on the μ . The blue band represents the post-fit impact on the μ when the μ and NP change in the same direction and green band represents the same when they change in the opposite direction. The black dot is the uncertainty on the NP pull and red band corresponds to its 1σ band.

11.1 Sensitivity for the simulated signal samples

Given the null result for the presence of the signal, the results can be utilized to place constraints on the signal phase space. The 95% CL expected and observed limits on the $\text{BR}(H \rightarrow \text{NLSP NLSP})$ are placed on the 36 simulated signal samples and are shown in Figure 11.4. The best sensitivity which is around 1.3% on $\text{BR}(H \rightarrow \text{NLSP NLSP})$ corresponds to the highest m_{NLSP} and the lowest m_{LSP} (at the bottom right corner of each plot). This large Δm results in high photon acceptance as higher fraction of these photons pass the p_T threshold compared to the other signal points. For the signal points away from the bottom right corner, the photon acceptance decreases as the photons tend to be softer, resulting in a worse limit. The comparison between the two lifetimes of 2 and 10 ns shows that the sensitivity is better for the 2-ns samples. This is because for samples with lower lifetime, there is a higher probability that at least one NLSP decays before the calorimeter, resulting in higher photon acceptance.

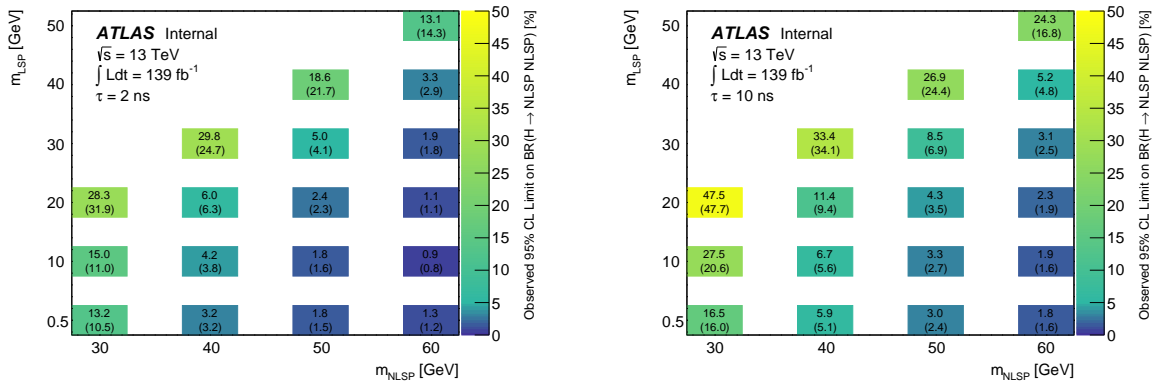


Figure 11.4: The 95% CL observed limits on the $\text{BR}(H \rightarrow \text{NLSP NLSP})$ along with the expected limits in the brackets for different simulated signal points. The X-axis corresponds to the m_{NLSP} and the Y-axis corresponds to the m_{LSP} . The lifetime of the NLSP is 2 ns (10 ns) for the left (right) plot.

11.2 Interpolation of the results

The displaced photon signature has three independent parameters: m_{NLSP} , m_{LSP} and τ for the NLSP. This section extends the result to a wide range in each of these parameters.

11.2.1 Intermediate mass interpolation

An interpolation of the results between all the signal points for each lifetime is performed separately. The high- Δm analysis enables this interpolation for different masses of the NLSP and LSP while the low- Δm points allow interpolation for different masses of the NLSP but at a constant $\Delta m = 10$ GeV. Given that the selections are independent for these two analyses, a smooth transition between the results is not expected. The 95% CL expected and observed limits on the BR($H \rightarrow NLSP NLSP$) for the high- Δm and low- Δm analysis are shown in Figures 11.5 and 11.6 respectively. For the high- Δm analysis, most of the signal phase space can be excluded based on this analysis while only the higher m_{NLSP} signal points are excluded beyond what is constrained by the upper limits on BR($H \rightarrow$ undetected) $< 21\%$.

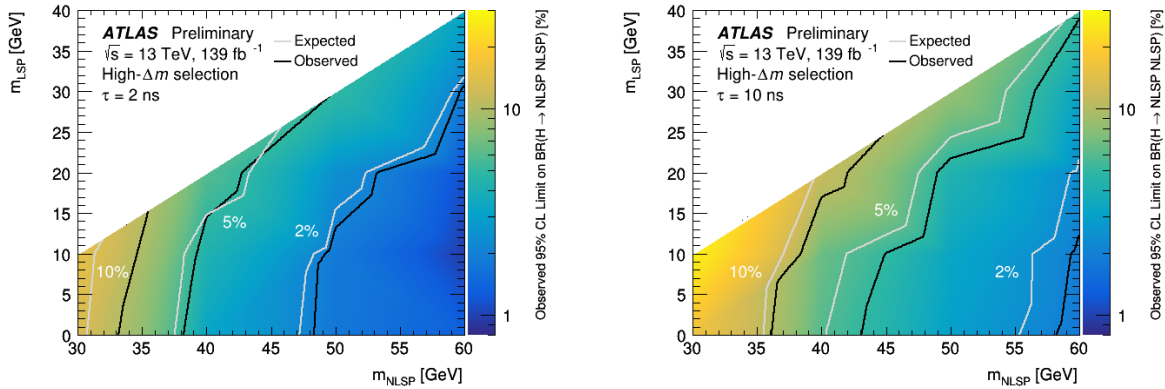


Figure 11.5: The 95% CL observed limits on the BR($H \rightarrow NLSP NLSP$) for the high- Δm analysis with contours indicating the various observed limits (2, 5 and 10 %) in black along with the corresponding expected limits in grey. The X-axis corresponds to the m_{NLSP} and the Y-axis corresponds to the m_{LSP} . The lifetime of the NLSP is 2 ns (10 ns) for the left (right) plot.

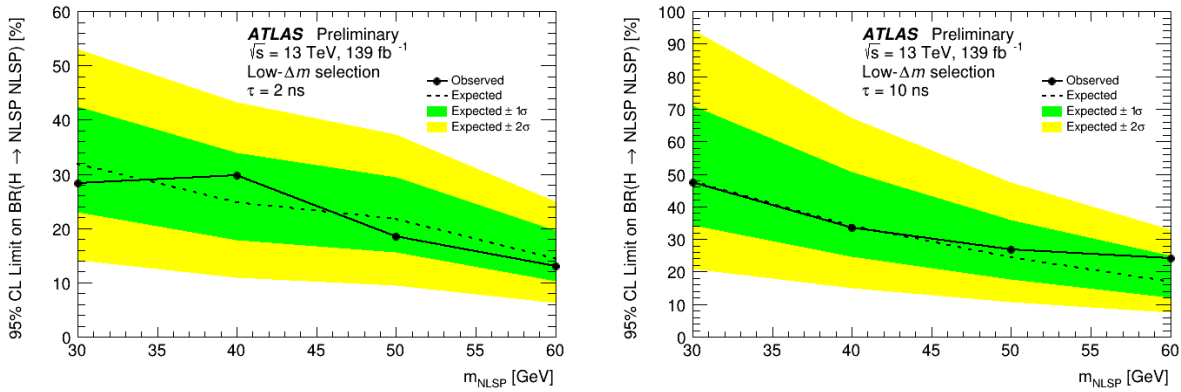


Figure 11.6: The 95% CL observed limits on the $\text{BR}(H \rightarrow \text{NLSP NLSP})$ for the low- Δm analysis along with the expected limits. The X-axis corresponds to the m_{NLSP} and note that $m_{LSP} = m_{\text{NLSP}} - 10$ GeV. The lifetime of the NLSP is 2 ns (10 ns) for the left (right) plot.

11.2.2 Lifetime reweighting procedure

In order to extrapolate the results to a wide range of lifetimes between 0.25 and 100 ns, a lifetime reweighting procedure is implemented on the signal grid. Each signal event contains two photons from each of the NLSP decays and the decay of each NLSP depends on its lifetime. Using the decay time of the target lifetime and the decay time of the initial sample, an event weight is calculated to simulate the target lifetime. Given the low statistics of the signal sample, a fit to the functional form of an ideal exponential decay is performed for both the NLSP lifetimes to avoid statistical fluctuations. Next, an event weight is applied to scale the events from the source lifetime to the target lifetime, and it is given by

$$wt_{\text{source} \rightarrow \text{target}} = \left(\frac{\tau}{\tau'}\right)^2 \exp\left[(-\tau_1 - \tau_2) * \left(\frac{1}{\tau'} - \frac{1}{\tau}\right)\right] \quad (11.1)$$

where the τ is the source lifetime, τ' is the target lifetime, and τ_1, τ_2 are the parent particle proper times for the leading and sub-leading photon in each event, respectively.

A closure test is shown in Figure 11.7. This test is performed by reweighting the $(m_{\text{NLSP}}, m_{LSP}, \tau) = (60 \text{ GeV}, 0.5 \text{ GeV}, 10 \text{ ns})$ signal point to itself. The final reweighted lifetime distribution is consistent with the initial lifetime profile. In order to reweight the signal samples from 0.25 to 100 ns, validation tests are performed starting with different source lifetimes and reweighting to target lifetimes of 0.3, 5 and 10ns. The results for these tests are shown in Figures 11.8, 11.9 and 11.10 respectively. Each of these figures shows the comparison between the time distribution in each pointing category starting at different source lifetimes. The ratio panel shows that each of these samples are in agreement within the statistical uncertainty. This validation studies show consistent behavior for signal events

between 0.3 and 100 ns, facilitating the interpolation of the results in this range. Note that the uncertainties associated with this reweighting procedure are taken into account for the sensitivity estimate.

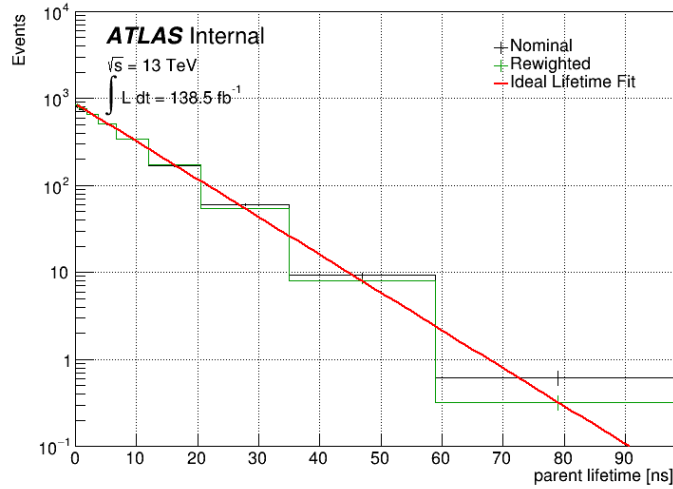


Figure 11.7: The lifetime of the signal point $(m_{NLSP}, m_{LSP}, \tau) = (60 \text{ GeV}, 0.5 \text{ GeV}, 10 \text{ ns})$ before reweighting (black), after reweighting (green) and the ideal exponential decay time (red).

11.2.3 Lifetime interpolation

For a particular m_{NLSP} of 30, 40, 50 and 60 GeV, the 95% CL limits as a function of the lifetime and m_{LSP} are shown in Figure 11.11. For $m_{NLSP} = 60 \text{ GeV}$, the signal phase space for lifetimes of 0.3 to 100 ns and up to m_{LSP} around 40 GeV can be excluded. The sensitivity is the highest for $m_{NLSP} = 60 \text{ GeV}$ for a wide range of lifetimes as the photon acceptance is highest compared to the other lower m_{NLSP} .

The 95% CL limits on the $\text{BR}(H \rightarrow \text{NLSP NLSP})$ as a function of m_{NLSP} and lifetime is shown in Figure 11.12. Different colors correspond to different m_{LSP} in these plots. Each of these plots shows that the best sensitivity is around 2 ns and it gets worse as we move away in lifetime in either direction. This is expected because at higher lifetimes, the probability that at least one NLSP will decay before the calorimeter producing a displaced photon signature decreases. This results in lower photon acceptance and hence sensitivity. For the lifetimes below 2 ns, the signal starts to have narrower photon pointing and timing distributions due to the low lifetime of the NLSP. This makes it difficult to distinguish between the signal and the prompt background, resulting in reduced sensitivity.

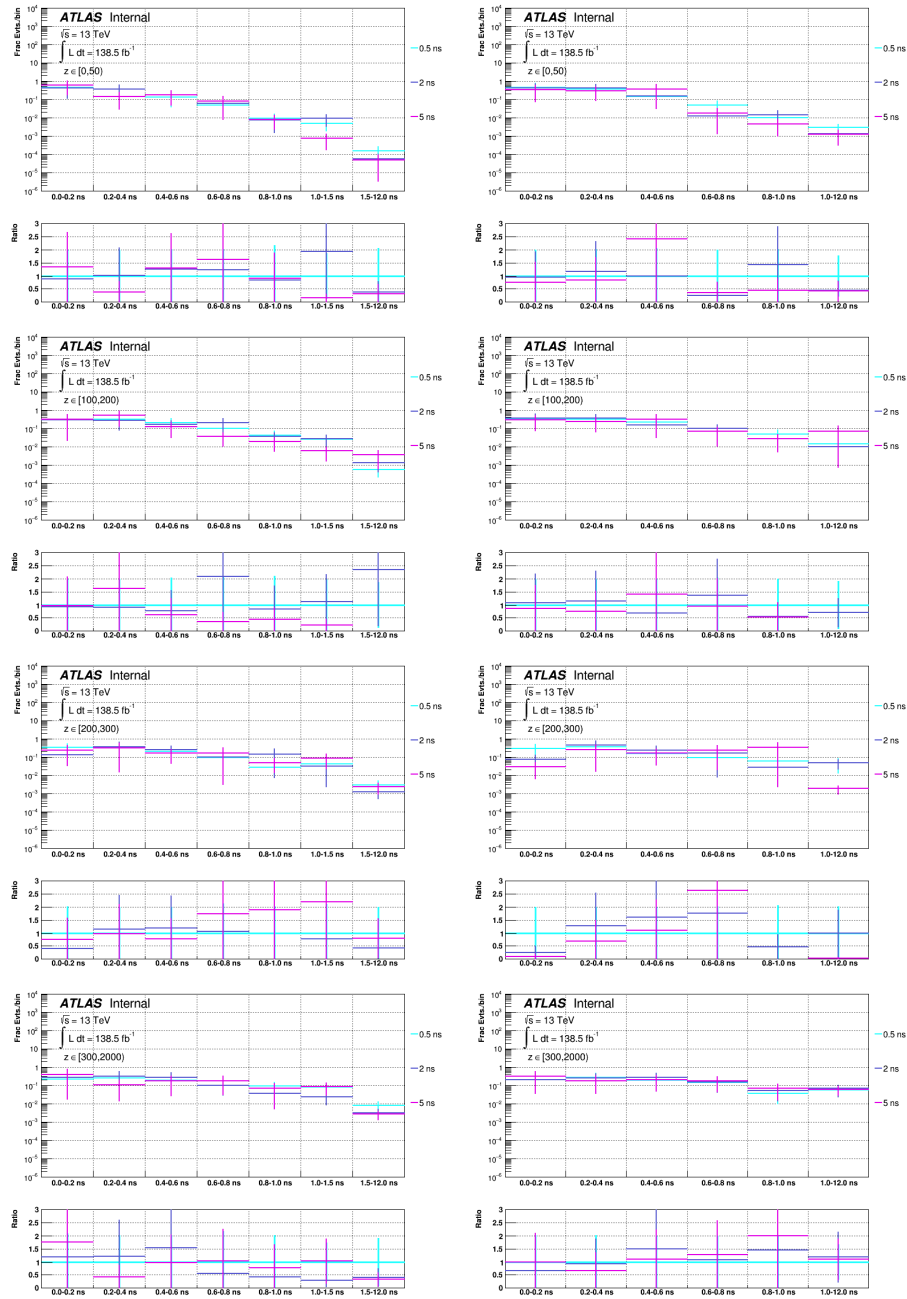


Figure 11.8: Comparison of 0.5 ns, 2 ns, and 5 ns parent lifetime samples reweighted to 0.3 ns target lifetime in each pointing category, for the 1γ channel (left) and the $\geq 2\gamma$ channel (right). The ratio of each reweighted distribution is taken with the reweighted 0.5 ns sample, which is the closest generated sample to the target lifetime. The X-axis corresponds to the various timing bins.

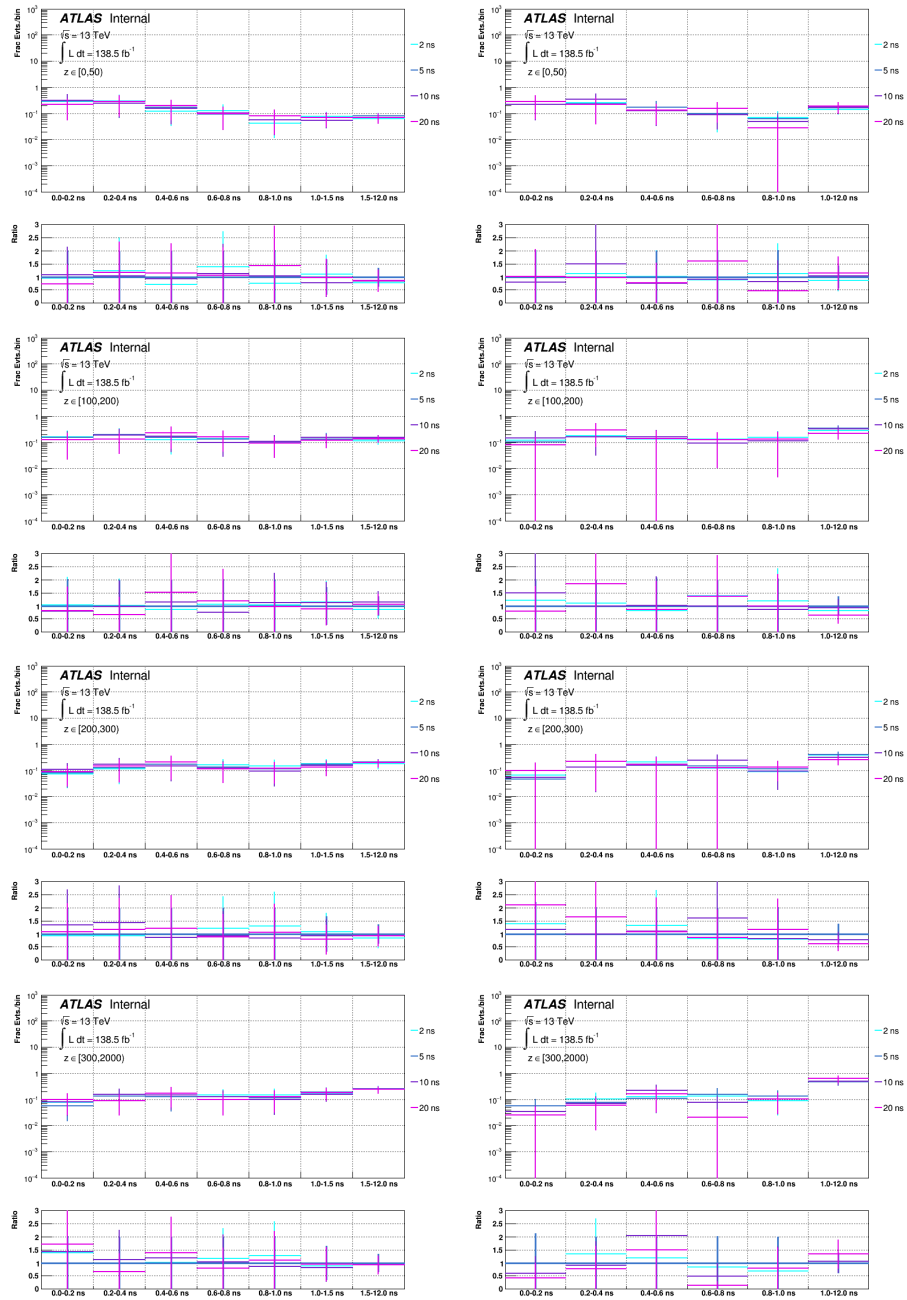


Figure 11.9: Comparison of 2 ns, 5 ns, 10 ns, and 20 ns parent lifetime samples reweighted to 5 ns target lifetime in each pointing category, for the 1γ channel (left) and the $\geq 2\gamma$ channel (right). The ratio of each reweighted distribution is taken with the 5 ns sample. The X-axis corresponds to the various timing bins.

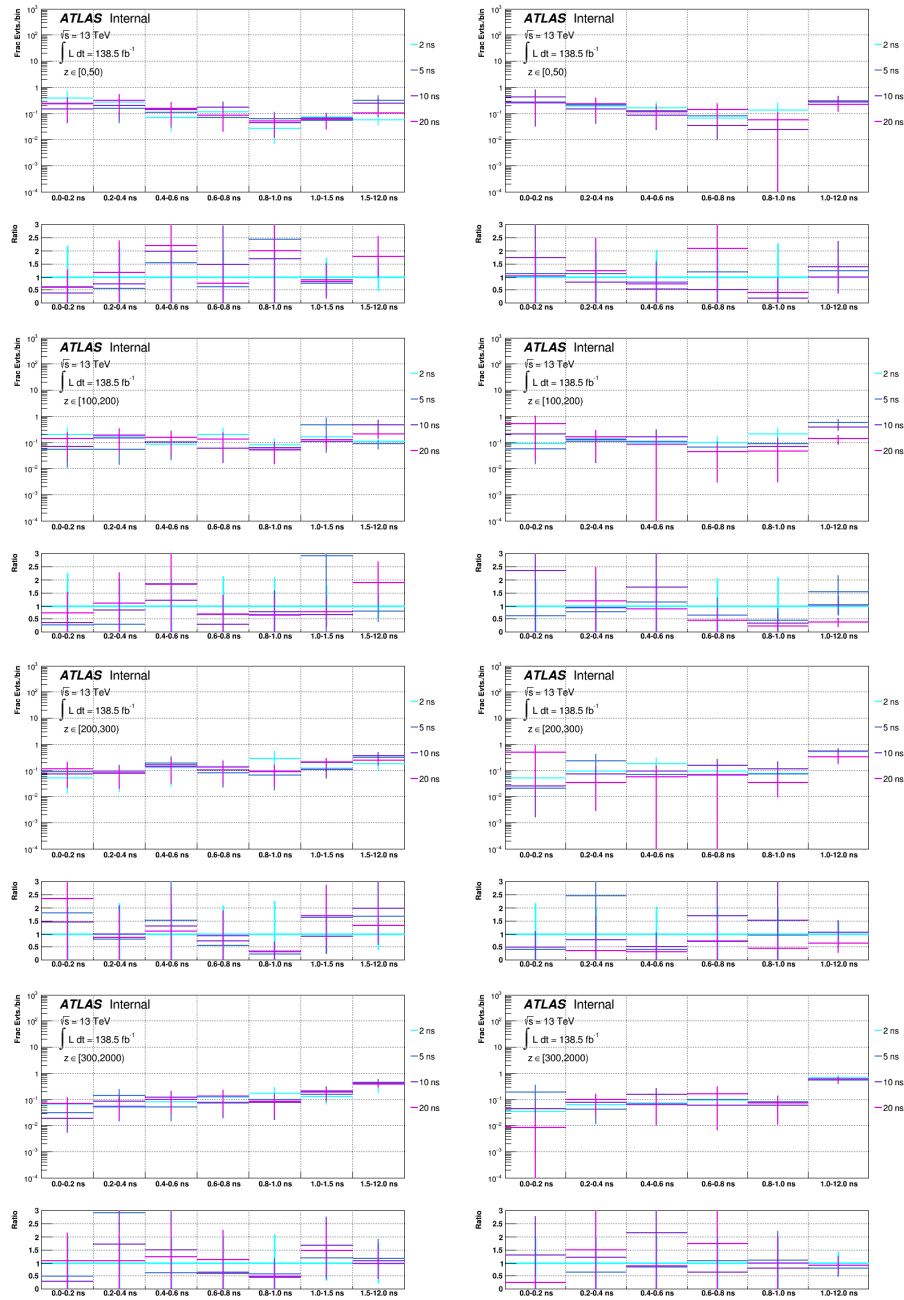


Figure 11.10: Comparison of 2 ns, 5 ns, 10 ns, and 20 ns parent lifetime samples reweighted to the 100 ns target lifetime in each pointing category, for the 1γ channel (left) and the $\geq 2\gamma$ channel (right). The ratio of each reweighted distribution is taken with the reweighted 20 ns sample, which is the closest generated sample to the target lifetime.

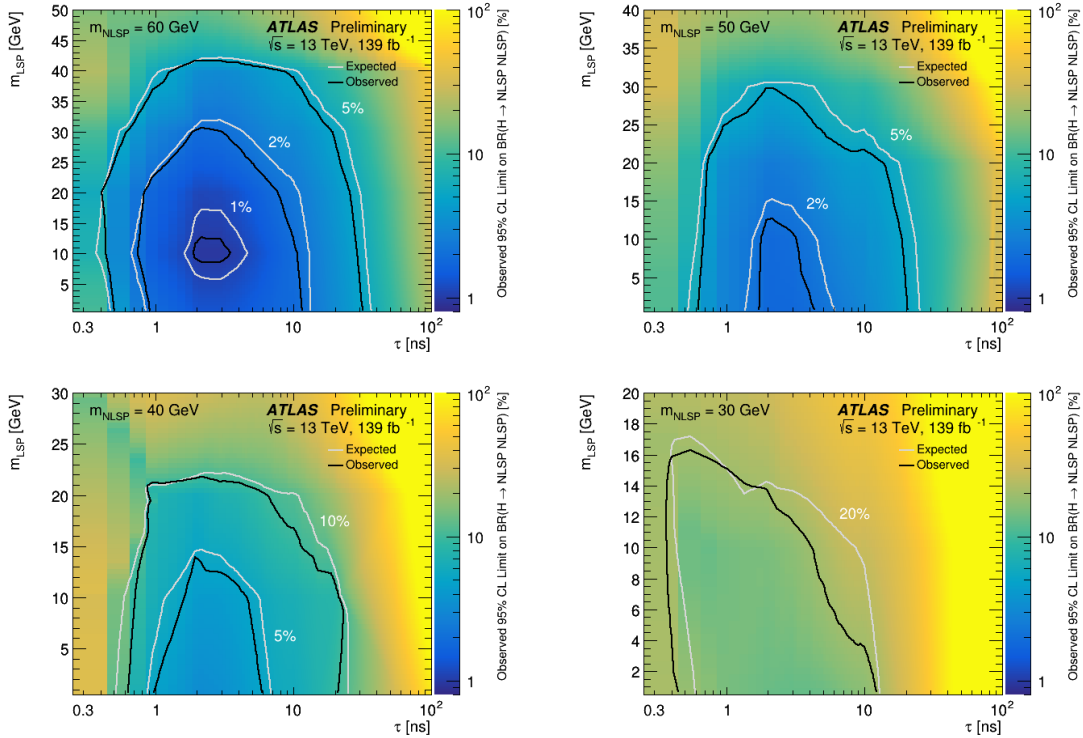


Figure 11.11: Interpolated 95% CL limits on $\text{BR}(H \rightarrow \text{NLSP NLSP})$ as a function of lifetime (X-axis) and m_{LSP} (Y-axis) for fixed $m_{NLSP} = 60$ GeV (top left), 50 GeV (top right), 40 GeV (bottom left), and 30 GeV (bottom right). Expected (grey) and observed (black) contours for limits are superimposed where possible.

11.3 Model-independent results

This section allows the analysis to be interpreted for any signal model involving displaced photons and summarizes the event selection applied at the truth level, corresponding acceptance and efficiencies along with the expected background yield and observed number of events in relevant model-independent signal regions.

The event preselection requirements applied at the truth level for the signal events are documented in Table 11.3.

After the preselection is applied, events with at least one electron are vetoed if the invariant mass of the electron and the photon is within the Z mass window $|m_{e\gamma} - 91.18| < 15$ GeV. The signal region is selected by applying $\text{MET} > 50$ GeV. For the 1γ channel, the model-independent region of interest is selected by requiring $300 < |\text{truth pointing}| < 2000$ mm and $1.5 < |\text{truth timing}| < 12$ ns whereas for the $\geq 2\gamma$ channel the requirements are

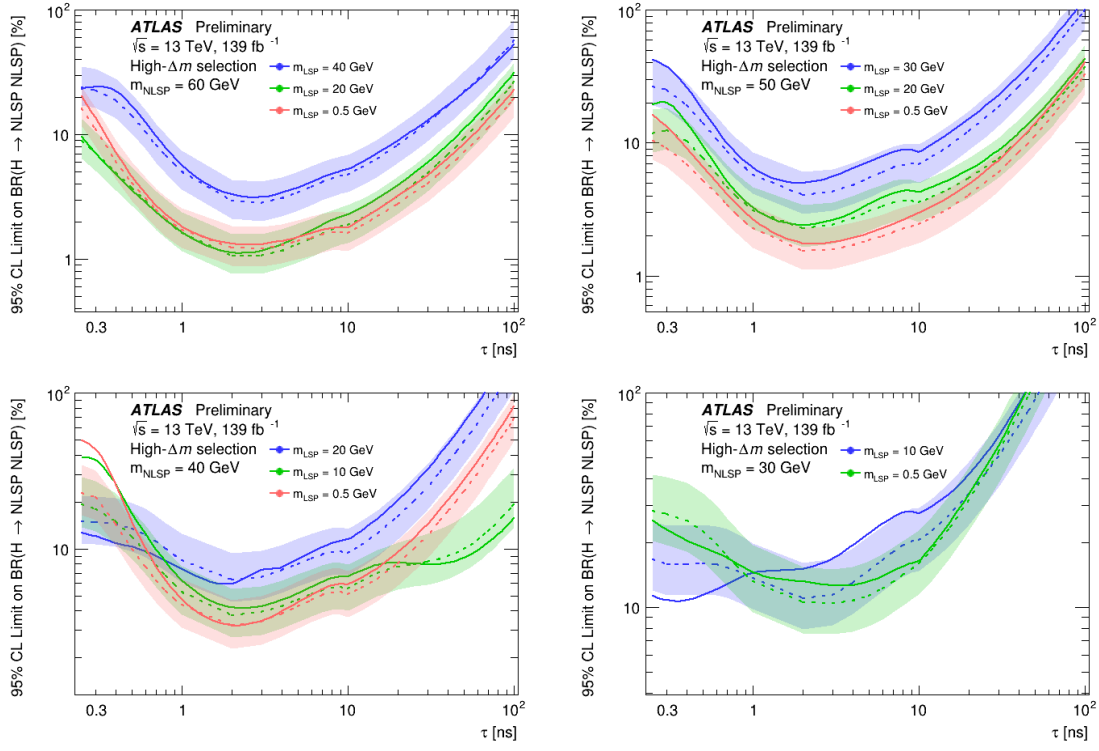


Figure 11.12: Interpolated 95% CL limits on $\text{BR}(H \rightarrow \text{NLSP NLSP})$ as a function of lifetime (X-axis) and m_{NLSP} (Y-axis). Different colors correspond to different m_{LSP} .

$300 < |\text{truth pointing}| < 2000$ mm and $1 < |\text{truth timing}| < 12$ ns. Here, truth pointing and timing are calculated using geometry and analytical calculations.

	Lepton	Photon
Multiplicity	≥ 1	≥ 1
Leading p_T [GeV] (subleading)	> 27 (> 10)	> 10
$ \eta $	< 1.37 or $[1.52, 2.47]$ (e), < 2.7 (μ)	< 1.37 or $[1.52, 2.37]$
		Photon production vertex $ z \leq 3704$ mm and $ r \leq 1567.33$ mm

Table 11.3: Table of common event preselection criteria at the truth level for analysis regions.

Table 11.4 compares the event yield for the (60,0.5,2) signal point at reconstruction level against the truth level yield at various stages of the selection. The truth level acceptance and the efficiency is also available in this table for this signal point. The acceptance and efficiency in the model-independent regions for the 1γ and $\geq 2\gamma$ channel for all the signal

Reco selections	Reco yield	Truth selections	Truth yield	Truth acceptance(%)	Efficiency Reco/Truth(%)
Total	75527.29	Total	75527.24	100.0000	100.0001
$\geq 1\text{lep}$	40034.45	$\geq 1\text{lep}$	49245.89	65.2028	81.2950
Trigger	34907.83			0.0000	
$\geq 1\gamma$	16309.59	$\geq 1\gamma$	31029.4	41.0837	52.5617
$ m_{e\gamma} - 91.18 > 15 \text{ GeV}$	14617.6	$ m_{e\gamma} - 91.18 > 15 \text{ GeV}$	28743.47	38.0571	50.8554
$E_{\text{cell}} \geq 10$	11129.08			0.0000	
$\text{MET} > 50$	6439.51	$\text{MET} > 50$	17647.59	23.3659	36.4895
1γ	3681.045	1γ	5880.763	7.7863	62.5947
$300 < z < 2000\text{mm}$	835.3094	$300 < z < 2000\text{mm}$	2254.321	2.9848	37.0537
$1.5 < t < 12\text{ns}$	129.3727	$1.5 < t < 12\text{ns}$	682.1475	0.9032	18.9655
$\geq 2\gamma$	2758.466	$\geq 2\gamma$	11766.82	15.5796	23.4427
$300 < z < 2000\text{mm}$	499.8719	$300 < z < 2000\text{mm}$	3694.713	4.8919	13.5294
$1 < t < 12\text{ns}$	158.3569	$1 < t < 12\text{ns}$	2102.022	2.7831	7.5336

Table 11.4: Comparison of event yields for 60,0.5,2 signal point at different stages of reconstructed level selections against the selections at truth level. The truth acceptance and the efficiency is also included here.

points is available in Table 11.5. The efficiency in the 1γ channel ranges from 1-19% and the efficiency in the $\geq 2\gamma$ channel ranges from 0-25% and is presented in Figure 11.13.

The model-independent limits are available for separately for the 1γ channel with photon timing range of 1.5-12 ns and for the $\geq 2\gamma$ channel with photon timing range of 1-12 ns in the pointing category $300 < |z| < 2000 \text{ mm}$.

The number of observed events for these bins are obtained from the high- Δm analysis data. The procedure to obtain the expected background and the uncertainty in this bin is to use the first few timing bins in the $300 < |z| < 2000 \text{ mm}$ category to obtain fitted values for all the parameters and use these fitted values to extrapolate the background estimate to the last timing bin which is of interest. The number of observed events along with the expected background and the corresponding 95% CL limit on the signal yield are available in Table 11.6.

mchi20 [GeV]	mchi10 [GeV]	tau[ns]	1γ binyield	$\geq 2\gamma$ binyield	total yield	1γ acceptance(%)	$\geq 2\gamma$ acceptance(%)	1γ efficiency (Reco/truth)%	$\geq 2\gamma$ efficiency (Reco/Truth)%
30	0	2	313.8	105.8	7.55E+04	0.4154	0.14	6.3034	3.2136
30	0	10	570	26.06	7.55E+04	0.7547	0.0345	5.6158	24.4436
30	10	2	267.7	94	7.55E+04	0.3545	0.1245	5.9694	6.8511
30	10	10	470.4	20.75	7.55E+04	0.6228	0.02748	3.9435	16.4145
30	20	2	94.49	44.88	7.55E+04	0.1251	0.05942	5.2376	3.6765
30	20	10	193.1	11.2	7.55E+04	0.2557	0.01482	1.4972	0.0000
40	0	2	656.2	434.6	7.55E+04	0.8688	0.5754	7.7522	8.3019
40	0	10	1126	129.5	7.55E+04	1.49	0.1714	8.4076	3.4880
40	10	2	655.9	416.6	7.55E+04	0.8684	0.5516	5.7234	7.0523
40	10	10	1221	124.9	7.55E+04	1.617	0.1654	7.0934	7.6717
40	20	2	509.4	301.4	7.55E+04	0.6745	0.399	4.5053	6.4001
40	20	10	1025	74.85	7.55E+04	1.358	0.0991	4.3707	10.9980
40	30	2	205.4	76.92	7.55E+04	0.2719	0.1018	2.2308	3.6531
40	30	10	428	21.85	7.55E+04	0.5667	0.02893	2.1619	2.4650
50	0	2	771	1076	7.55E+04	1.021	1.425	10.5525	8.2807
50	0	10	1840	416.8	7.55E+04	2.436	0.5518	9.6576	7.5888
50	10	2	787.8	1018	7.55E+04	1.043	1.347	9.6789	7.2790
50	10	10	1800	389	7.55E+04	2.383	0.5151	8.6278	8.6632
50	20	2	790.3	845	7.55E+04	1.046	1.119	5.9990	5.2201
50	20	10	1718	355.6	7.55E+04	2.274	0.4709	7.0896	6.9123
50	30	2	688.1	640.8	7.55E+04	0.9111	0.8484	3.8730	3.8530
50	30	10	1472	263.6	7.55E+04	1.949	0.349	4.2711	3.6764
50	40	2	283.2	138.9	7.55E+04	0.375	0.1839	2.4806	1.1677
50	40	10	653	76.83	7.55E+04	0.8646	0.1017	1.6401	0.7238
60	0	2	682.1	2102	7.55E+04	0.9032	2.783	18.9708	7.5357
60	0	10	1891	1061	7.55E+04	2.504	1.405	11.3591	7.1074
60	10	2	696.8	2037	7.55E+04	0.9226	2.698	18.0970	7.5896
60	10	10	1940	1168	7.55E+04	2.568	1.546	11.6701	5.6918
60	20	2	730.1	1907	7.55E+04	0.9667	2.525	16.6142	6.4289
60	20	10	1898	1008	7.55E+04	2.513	1.334	12.3130	3.2917
60	30	2	747.3	1629	7.55E+04	0.9895	2.156	9.2493	5.3726
60	30	10	1853	933.6	7.55E+04	2.454	1.236	7.4258	5.2367
60	40	2	777.3	1177	7.55E+04	1.029	1.559	5.7198	4.1759
60	40	10	1666	624.9	7.55E+04	2.205	0.8274	5.4298	2.9173
60	50	2	462.7	226.3	7.55E+04	0.6127	0.2996	1.4740	4.4940
60	50	10	905.6	146	7.55E+04	1.199	0.1933	2.2228	0.1633

Table 11.5: Signal yields at truth level, acceptance and efficiency in the 1γ and $\geq 2\gamma$ model-independent regions.

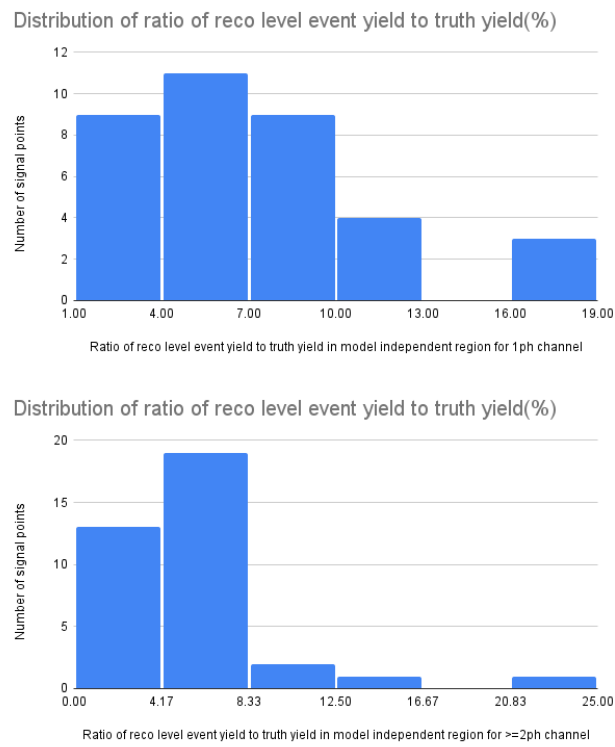


Figure 11.13: Ratio of the reconstructed yields to the truth yields in the model-independent signal regions in the 1γ and $\geq 2\gamma$ channel for all signal points.

	$1\gamma, 1.5 < t < 12$ ns	$\geq 2\gamma, 1 < t < 12$ ns	Combined $1\gamma + \geq 2\gamma$
N_data	4	0	4
N_bkg	3.80	0.28	4.08
N_bkg error	1.61	0.044	1.66
p-value	0.47	0.77	0.513
significance	0.08	-0.75	-0.03
95% CL expected limit	5.65	3	5.76
95% CL observed limit	5.82	3	5.70

Table 11.6: Model-independent limits using the last timing bin in the highest pointing category for the 1γ and $\geq 2\gamma$ channels separately. Limits for the combination of these two channels is presented in the last column. The table also includes the observed number of events N_data, background estimation N_bkg and the systematic uncertainty of the estimated background, N_bkg error.

Chapter 12

Summary and outlook

The ATLAS detector recorded 139 fb^{-1} of proton-proton collision data at center of mass energy of 13 TeV during the Run 2 of the Large Hadron Collider. This dataset provided an opportunity to search for beyond Standard Model physics using the Standard Model Higgs boson as a probe. The current upper limits on the branching ratio of the Higgs boson decaying into undetected particles is 21%, leaving room for new physics in the exotic decays of the Higgs boson.

This thesis described a search for the exotic decay of the Higgs boson to a pair of long-lived next-to-lightest supersymmetric particle (NLSP). Each of the NLSPs decayed into a photon and a stable lightest supersymmetric particle (LSP). Such a signature has never been explored before. This exotic decay of the Higgs boson was produced in association production with $W/Z/t\bar{t}$ processes and the resulting electrons and muons from their decay was used to trigger the event.

The signal photons were delayed with respect to the prompt photons in their arrival at the ATLAS electromagnetic calorimeter resulting in delayed photons and their direction of flight pointed away from the primary vertex, resulting in non-pointing photons. This unique nature of non-pointing and delayed photons was used as a smoking gun to search for this signature and to distinguish the signal and the background. The background processes, which result primarily from the prompt photon, an electron misidentified as a photon, or a jet misidentified as a photon, had low photon pointing and timing compared to the signal photons.

The signal region events were required to have at least one lepton, one photon and high missing transverse energy. The analysis strategy was to divide the events in the Signal region into 10 categories based on photon pointing and number of photons. A simultaneous fit to the timing distribution was performed in each of these 10 categories. The background estimation was performed in a completely data-driven technique where they were estimated as a linear combination of real-enhanced and fake-enhanced photon timing templates obtained from the data control regions. The validation of the background estimation procedure and the statistical treatment of data was performed extensively using two different validation regions.

The background processes described the data well and no significant excess was observed.

This allowed for the 95% Confidence Level upper limits be established on the branching ratio of the Higgs decay to this signature in the three signal model parameters of mass and lifetime of the NLSP and the mass of LSP. The exclusion limits were interpreted in masses of the NLSP ranging from 30 to 60 GeV for different masses of LSP ranging from 0.5 to LSP-10 GeV and the lifetime ranging from 0.25 to 100 ns. This was the first set of results from the ATLAS collaboration exploring this phase space. While this search targets a specific signal model, a more model-independent signal region was identified and results were presented here to allow for the reinterpretation of this result to any signal model involving non-pointing and delayed photons.

This analysis can serve as a baseline for displaced-photon search program within the ATLAS collaboration. The analysis techniques and the development of displaced photon identification, timing and pointing measurements developed here will be extremely relevant to any future analysis involving such a signature. One such search that involved a search for displaced photon vertex is currently underway in the ATLAS collaboration and many more are planned for Run-3. Other analysis can also benefit from the calorimeter timing and pointing capabilities such as the search for displaced charged particles which are produced at large radius that will not have a reconstructible track in the inner detector.

Appendix A

Power board stress testing

The High Luminosity Large Hadron Collider will deliver an instantaneous luminosity of $5 \times 10^{34} \text{ cm}^{-2} \text{ s}^{-1}$ and around 200 proton-proton collisions per bunch crossing. The current ATLAS detector needs to be upgraded to work under these challenging conditions. The inner detector of the upgraded ATLAS detector will be all silicon-based. In particular the Semiconductor Tracker (SCT) strip detector will be replaced by the Inner Tracker (ITk) strip detector.

The ITk strip detector will comprise of four-layer barrel section between -1.4 to 1.4 m in Z-axis range with each layer made of a cylinder surrounding the beam line. The strip system is extended by one end-cap on each side of the barrel. Each end-cap is made of six disks where each disk is shaped into a ring and the end-cap extends to 3 m in Z-axis. Together, the barrel and end-cap strip system provide coverage in $-2.5 < \eta < 2.5$.

My contribution to the ATLAS upgrade efforts is documented in this appendix. The subsequent sections describe the silicon module and the power board along with various stress tests performed on it to understand its performance under various conditions.

A.1 Module

The building block of the strip detector is a module that consists of the components shown in Figure A.1. It is placed on a stave in the barrel and a petal in the end-cap region. Each module can have different length and geometry depending on the location in the detector but it has the same components. For the first two layers of the barrel detector, shorter strips are used to provide greater segmentation and the outer two layers are made of longer strips. Hence, the barrel layers are made out of short-strip and long-strip modules. The end-cap module design is more complicated as each disk is of different size and at different distance in z direction from the interaction region. Please refer to the ATLAS Inner Tracker Strip Detector Technical Design Report [81] for more details about the geometry.

Figure A.2 shows a short-strip module assembled at the Lawrence Berkeley National Laboratory. Each short-strip module consists of two hybrids, each with ten ATLAS Binary

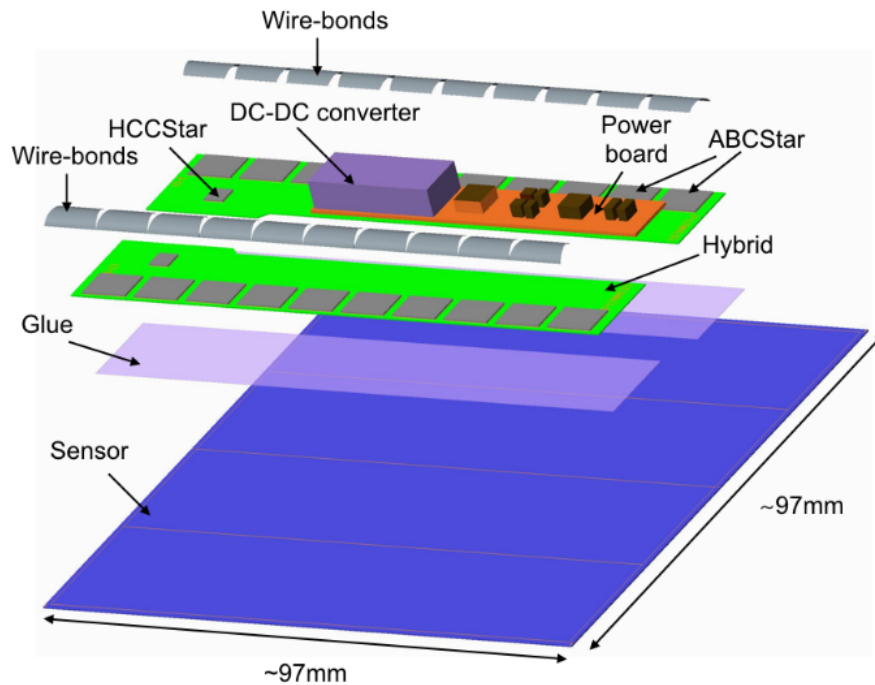


Figure A.1: Short-strip module in barrel layer. The other barrel and end-cap modules have same components with different arrangement.

Chip (ABCStar) glued to a silicon sensor. When a charged particle passes through the sensor, it creates a signal within the sensor diode which is transmitted to the ABCStar front-end chip. Each hybrid is equipped with a Hybrid Controller Chip (HCCStar) that collects the signal from the front-end chips and transmits it to the service bus of the corresponding stave/petal.

A.2 Power board

Each module has one power board located between the two hybrids not only provides the two hybrids with the required power but also provides many different functionalities.

A.2.1 Components and functions

Power board version 2 is 72 mm in length and 9 mm in width with components displayed in Figure A.3. The components and their functions are described below.

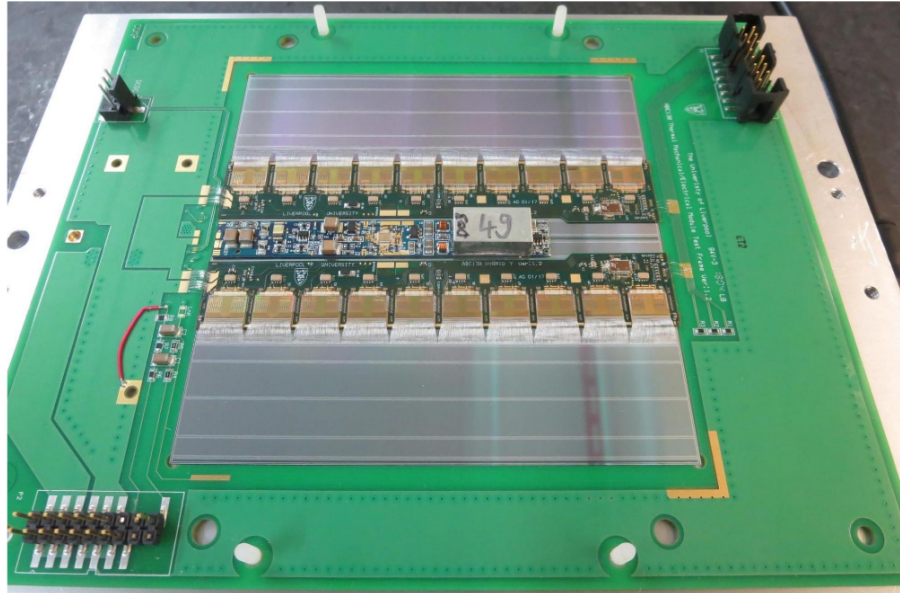


Figure A.2: A short-strip module assembled at the Lawrence Berkeley National Laboratory.

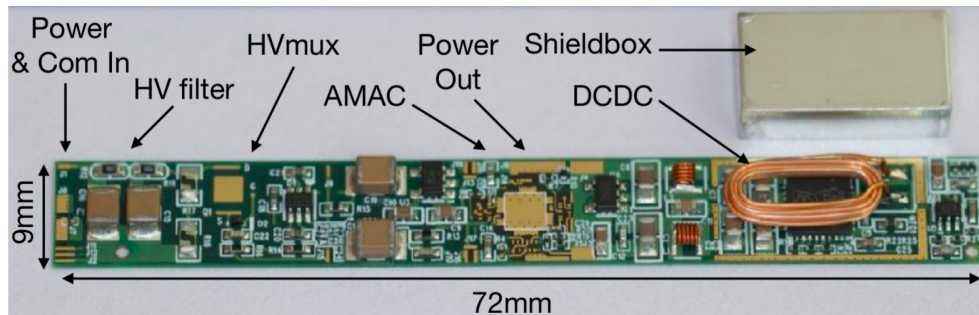


Figure A.3: Power board version 2 assembled at the Lawrence Berkeley National Laboratory.

1. FEAST: Power board v2 uses a DC-DC converter, FEAST 2.1, that converts the input voltage of 11 V down to 1.5 V that is used to power the front-end chips. The FEAST chip can be operated up to an output current of 4 A. The DC-DC buck converter operates at a switching frequency of 1.8 MHz.
2. AMAC: Autonomous Monitoring And Control chip is a custom ASIC designed to constantly measure the internal temperature, input voltage and current, output voltage and current and a variety of handles to examine conditions on the power board. Power

board v2 has an AMACv1 chip.

3. HV_MUX: High Voltage Multiplexer is designed to connect or disconnect any malfunctioning sensor from the sensor bias voltage. This is important as four modules are connected to High Voltage bias in parallel and if one of them suffers from early breakdown, then other sensors might not be operated at their design voltage.

Although I worked on the prototype version 2, an updated version of this will be installed in the upgraded ATLAS detector.

A.3 Power board testing

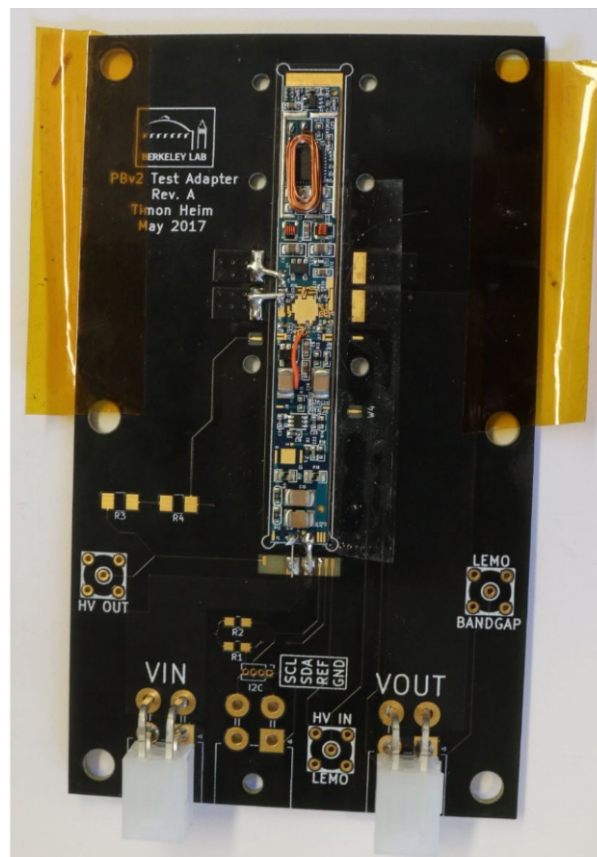


Figure A.4: Single power board test adapter.

The power board can be a single-point failure for an entire module. Testing the power board functionalities is important to ensure that it works efficiently at design specifications. Every AMAC is tested and calibrated separately before mounting on the power board.

The power board is mounted on a test adapter, shown in Figure A.4, that allows to test a single power board at a time. It is tested by using an external power supply to provide input voltage and current, a variable load to draw power from the board and an I²C communication from the AMAC to the computer to enable communication.

A.3.1 Efficiency measurement

One of the best ways to characterize the power board performance is to study its efficiency. Here, efficiency is defined as the ratio of power output to power input. Efficiency is measured as a function of current drawn from the power board. This also tells us the best working point of the power board and how much the efficiency drops as we draw different current. An example of an efficiency curve is given in Figure A.5. This measurement tells us the most

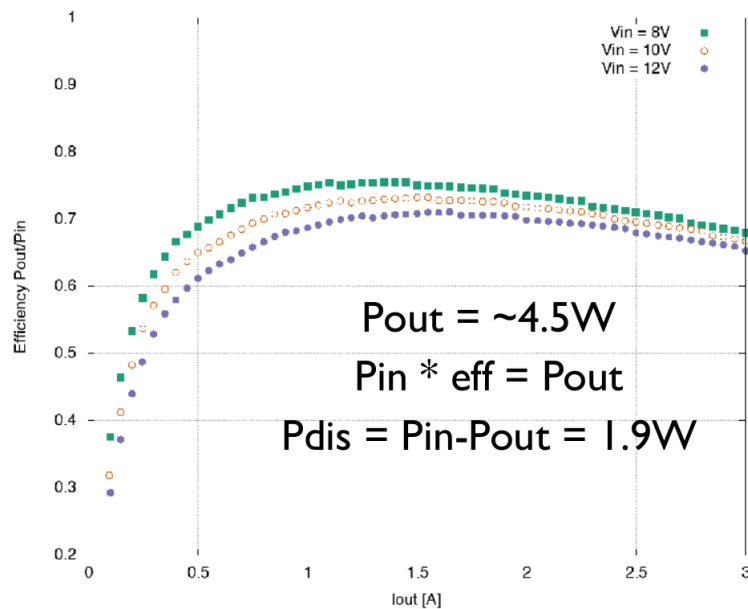


Figure A.5: Efficiency curve from the Power board specifications.

efficient working point for the power board is at an output current of 1A. The maximum efficiency is around 75% and it drops to around 65% at an output current of 3A which might be the actual working point of the power board.

A.3.2 Other measurements

The AMAC provides multiple handles to monitor the voltages, currents and temperatures on the power board. For example, there is an NTC thermistor on the power board that gives temperature information and it can be read out using the AMAC. There is a PTAT component at the FEAST to record its local temperature and the AMAC is used to read out this information. Another important measurement would be to monitor input voltage, current using the AMAC and verify it against the information from the power supply.

These tests are performed on every power board before placing it on a module.

A.4 Power board reliability measurement

A.4.1 Reliability definition

Reliability is the survival probability of an electrical component operating under specific conditions for a given period of time. In order to make sure that the upgraded ATLAS detector works reliably beyond the HL-LHC timeline, we need to test each and every component that goes into the detector.

In practice, reliability is measured by accelerating the potential failure modes of the component and studying how the component fails over a given time. For example, one possible failure mode of the power board is failure that occurs during power cycling of the input power. To estimate reliability for this failure mode, I would power cycle the boards every 10 seconds and see when, if any, failure occurs over time. This would give a probability of the product survival with respect to this failure mode. In order to estimate the total reliability of the power board, I need to identify all the possible failure modes and measure reliability with respect to each failure mode and then estimate the total reliability using this information.

A.4.2 Failure modes of power board

As can be seen in Figure A.3, the power board contains many components and failures can stem from variety of factors.

1. ASIC failure: Failure of active components like the AMAC, FEAST and HVMux will result in single-module failure. The reliability of these components is tested independent of the power board and the information is readily available.
2. Connection failures: The traces and/or wire bonds might be damaged that might result in the failure of a power board. To ensure reliability, the traces are 120- μm -wide and multiple wire bonds are used wherever possible.
3. External conditions: Efficient performance and longevity of a power board also depends on the operational conditions and changes in it.

- a. Power cycling: Fluctuations in the input voltage and current delivered to a power board can cause failure in the board over time.
- b. Long-term power-on test: Run the power boards for a long time to see if there are any unexpected failures.
- c. Temperature fluctuations: The nominal operational temperature of the power board in the detector would be -10°C but fluctuations in this over time or thermal cycling might reduce the reliability of the power board.
- d. Magnetic field changes: The power board in both the barrel and end-cap will be in a magnet and fluctuations in this might result in decreased performance.
- e. Radiation effects: The power board need to be qualified under radiation conditions to ensure the performance in the detector conditions. This can be done with later versions of the power board as all their components are radiation hard.

The power board has to be tested under each of these external conditions to determine its reliability.

The pixel system in the CMS experiment, which uses similar DC-DC converter as the power board, saw failure in operation in 2017¹. This made stress testing of the power board extremely critical.

For this project, I had set out to measure reliability under each of these external failure modes of the power board. This was a challenge due to the low number of power boards available and the necessity of characterizing the boards under these conditions. The tests performed by the author are described in the next section.

A.5 Stress testing the power board

A.5.1 Power cycling test

Goal of this test was to power cycle the power board frequently and study its performance over time. This was an important test to make sure that the board will run efficiently even after many power cycles or fluctuations. At the time this test was performed, the exact cause of the CMS pixel system failure was unknown and power cycling was thought to be the culprit, making this test very relevant.

The set up for this test involved the power board loaded on the single test adapter from Figure A.4, a power supply, an I²C communication device and a $0.5\ \Omega$ resistor (six $3\ \Omega$ resistors connected in parallel) that acts as a constant load. The setup can be seen in Figure A.6. The load draws 1.5 V voltage and 3 A current generating power of 4.5 W.

¹In early 2019, the problem was figured out to be because of transistors getting damaged under radiation [82]. This resulted in the FEAST2 DC-DC converter failure. The solution for future versions of FEAST was to add a resistor to the circuit. The final version of power board will use bPOL12V instead of FEAST which will implement this fix.

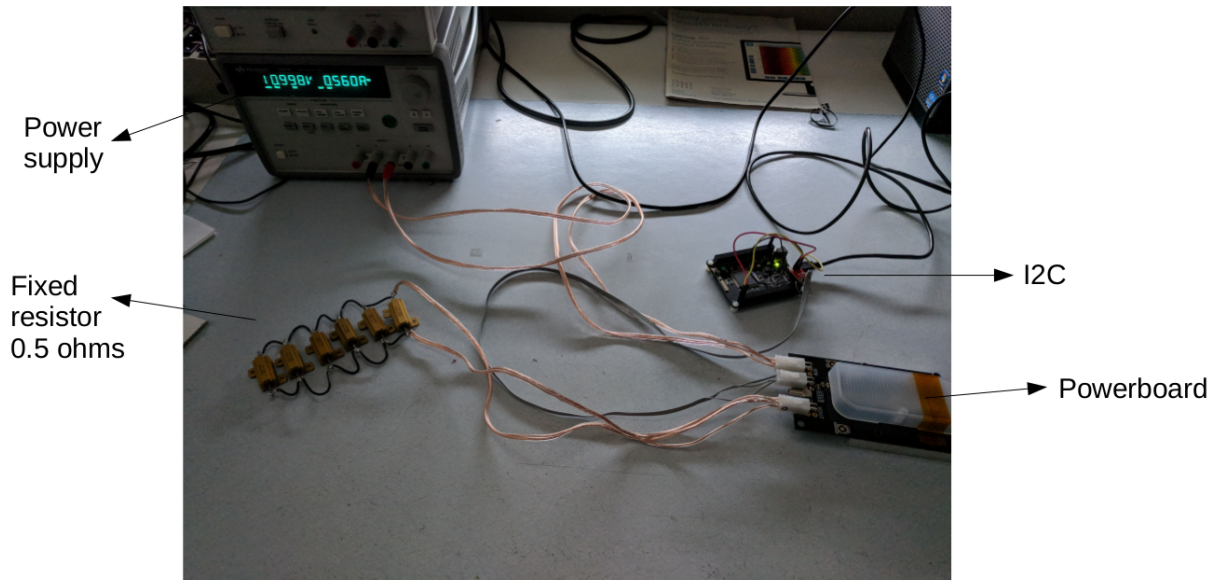


Figure A.6: Test setup for power cycling test.

The test essentially power cycled in combination with switching the low voltage (LV) enable on/off. At the beginning of the test, power supply was turned on and LV was disabled and the following information was read out: the input voltage, current from the power supply and monitor input voltage, current, temperature monitors NTC, PTAT, output voltage and current from the AMAC using the I²C communication. After each read out and a 10 second delay, another reading of the similar parameters was performed. This reading was repeated 10 times before turning the LV on and the repeated readout was done again. These 20 read outs taken during LV disable and enable was considered one cycle. After one cycle, the power board was turned off and then turned on followed by next cycle of measurements resulting in the power cycling of the system every 200 seconds.

This test ran for approximately 2 months before the power board ceased to work, possibly due to user error. One of the easiest ways to kill a v2 power board is to reverse the input and output wires; this may have been the cause of the observed failure. This has been fixed for the next version for more robust handling of the boards. The power boards ran without glitches for 6000 power cycles.

The main motive of the run was to monitor the efficiency, defined in Section A.3.1, over many power cycles. The result showing efficiency of the power board is presented in Figure A.7 and we can see that the efficiency rises with time, with many glitches after nearly 6000 power cycles. The rise in efficiency was not because of the better performance of the power board. It was due to the increase in resistance of the load and/or connecting wires as the system heats up over time. The load outputs 4.5 W and no cooling system was used to

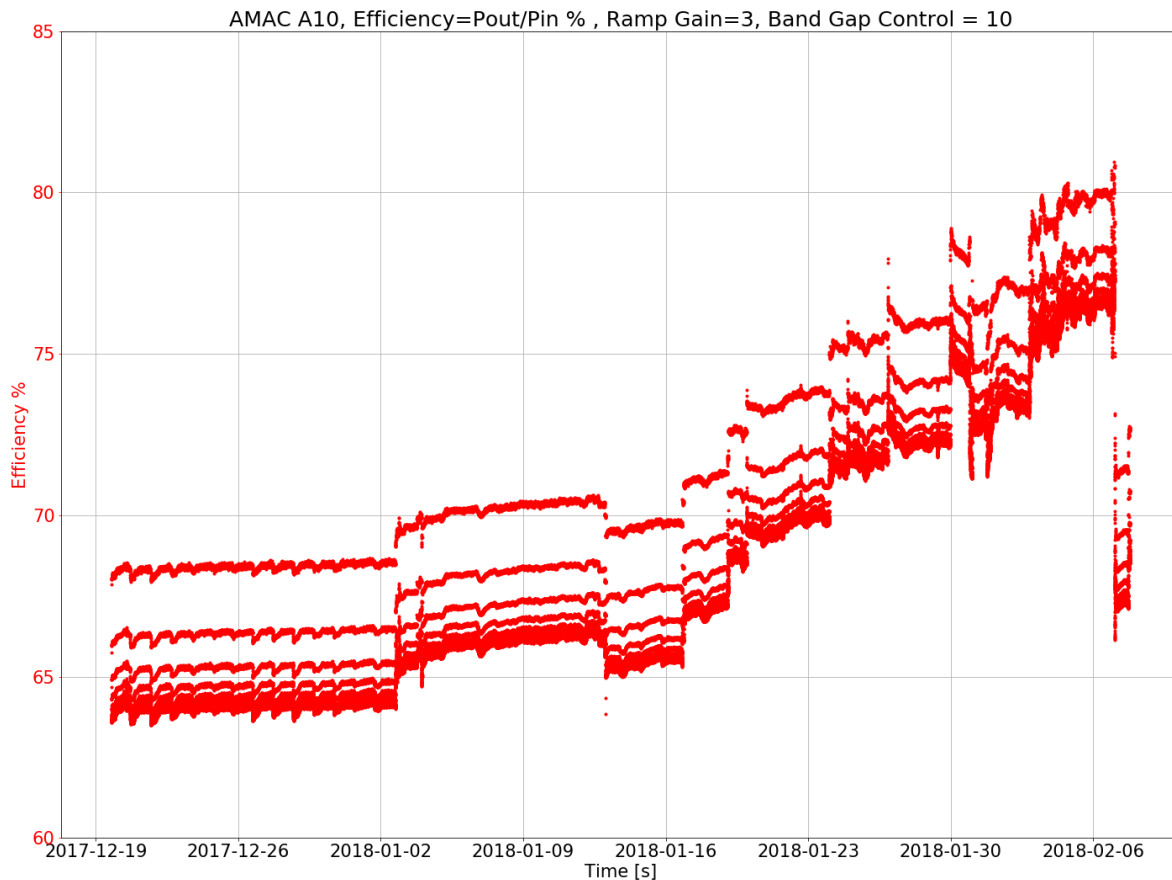


Figure A.7: Efficiency over time for power cycling. The rise in the efficiency was because no cooling system was in place to dissipate the heat as the load drew around 4.5 W from the power board.

regulate the temperature of the load. Another key lesson learnt from this test was the need of voltage monitoring on the load. These shortcomings have been rectified in the long-term test described next.

A.5.2 Long-term power-on test

After acquiring more power boards to test, the set up shown in Figure A.8 was assembled to run the power boards for long term and study their performance. For this test, 9 power boards were loaded without an AMAC on the passive mass tester which allowed the mass testing of 9 power boards at once and each power board was connected in series to the power supply. Each power board had a 0.5 Ohm resistor load connected to it. Depending on the

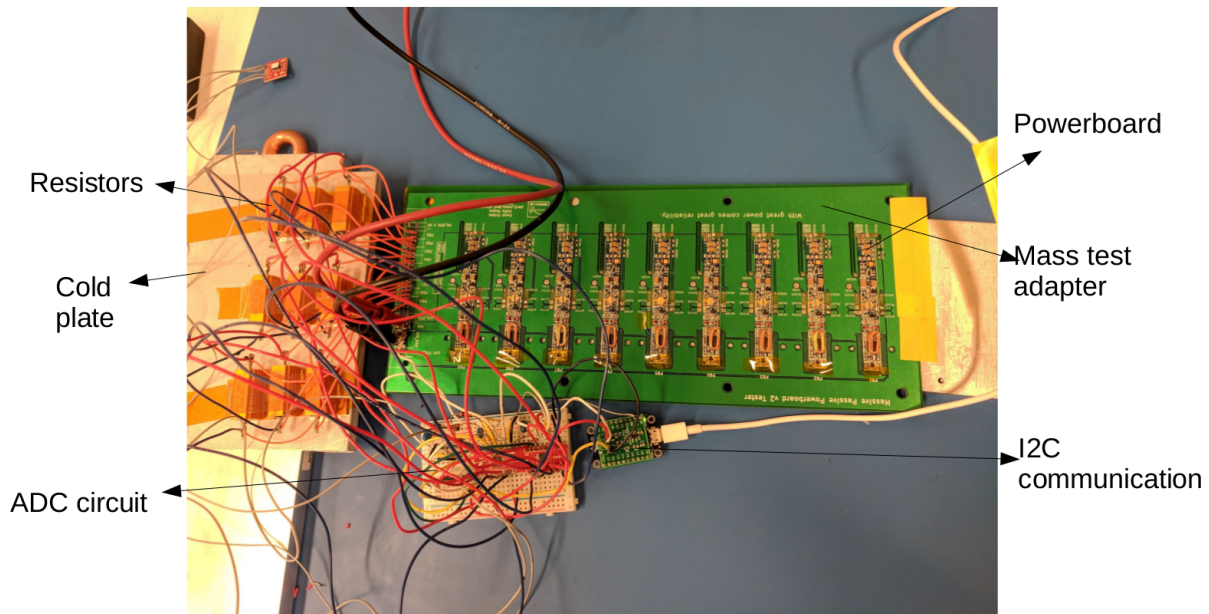


Figure A.8: Set up for the long-term test. This includes the mass testing of 9 power boards with one resistor load each and a cooling system.

position of the power board on the tester, the effective load could vary on each depending on the traces. The voltage across each resistor was monitored and the system was read every 10 seconds.

From the experience of power cycling test, a cooling system was in place for this test to ensure the heat dissipation from the loads. The temperature and humidity sensors were added to the set up to understand how these conditions might effect the efficiency. Unfortunately, one power board shorted during soldering, 8 power boards were working. After few glitches with the ADC device problems, only 6 of the resistors could be read out. The test ran for around 3 months with intermittent stops due to technical difficulties (power outages, cooling motor not working, system reboot). The test worked much beyond the 3 months that I was involved in the project.

As there is no AMAC, a lot of the power board functionalities could not be monitored. However, the voltage and current from the power supply along with the voltage over each resistor was available. Using this information, the efficiency of the power boards could be monitored.

The current drawn by the resistors is given in Figures A.9 to A.11. The current is more or less constant during all the runs. The efficiency is plotted in Figure A.12 to A.14. The efficiency is constant for over 900 hours in the November run. This is an excellent sign telling us that the performance of the power board doesn't drastically decrease over time. Given

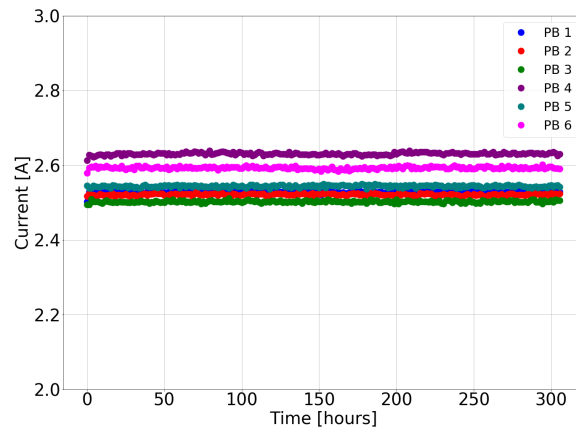


Figure A.9: Current across resistor as a function of time for 3-24 October 2018 run.

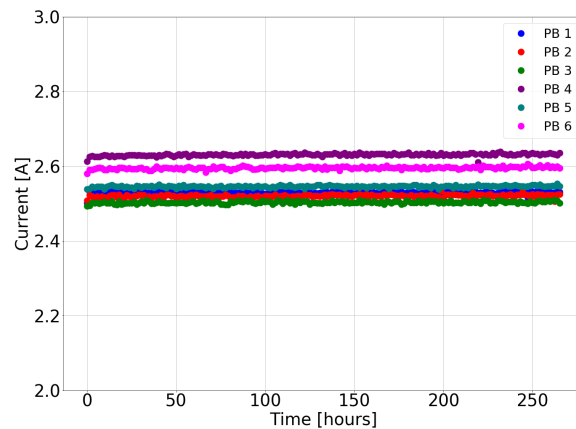


Figure A.10: Current across resistor as a function of time for 24 October - 12 November 2018 run.

the addition of the cooling system, the efficiency doesn't increase over time verifying that the artificial feature seen in Figure A.7 was due to the absence of a temperature control.

A.5.3 Thermal characterization

The power board will be operated at -10° C inside the ATLAS detector. However, it is important to characterize the power boards at different temperatures to study the changes

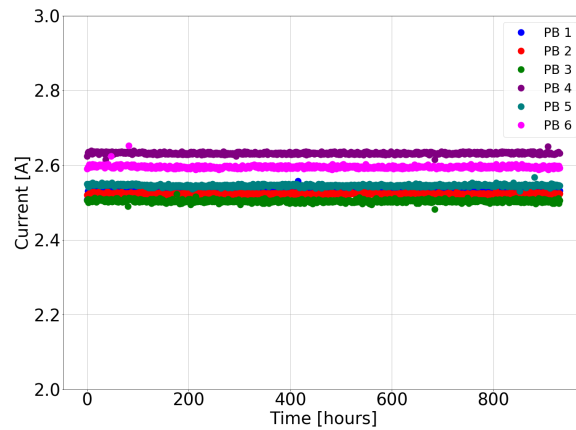


Figure A.11: Current across resistor as a function of time for 12 November 2018 - 24 January 2019 run.

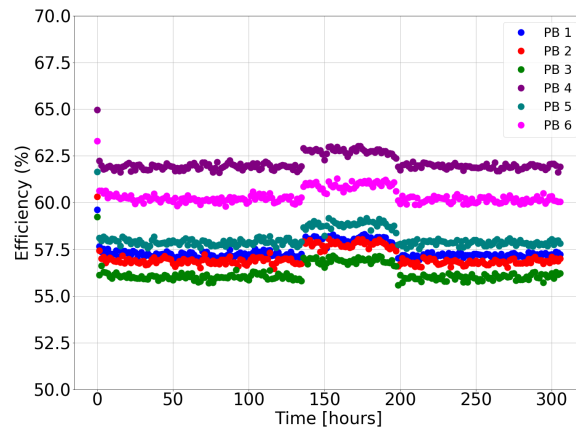


Figure A.12: Efficiency of the power board as a function of time for 3-24 October 2018 run.

in performance in case of temperature fluctuations.

Power board loaded on a test adapter was placed in a climate chamber that operated between -75 to $+200^{\circ}$ C. A power supply, commercial variable load and I²C communication device are connected to the power board. Temperature and humidity sensor were installed to get an independent measurement of the temperature inside the climate chamber.

The test procedure involved varying the temperature of the climate chamber from -40 to $+40^{\circ}$ C in increments of 5° C. After the temperature stabilized at a temperature setting,

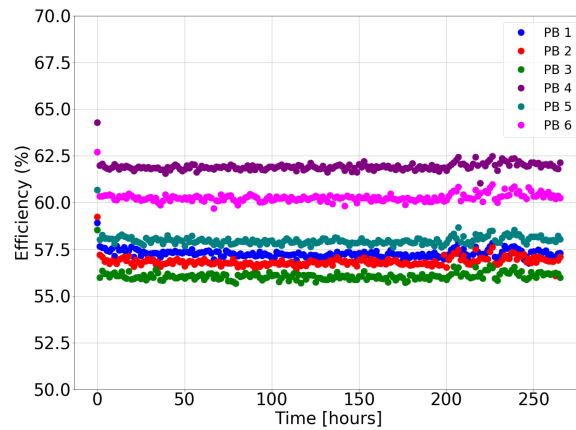


Figure A.13: Efficiency of the power board as a function of time for 24 October - 12 November 2018 run.

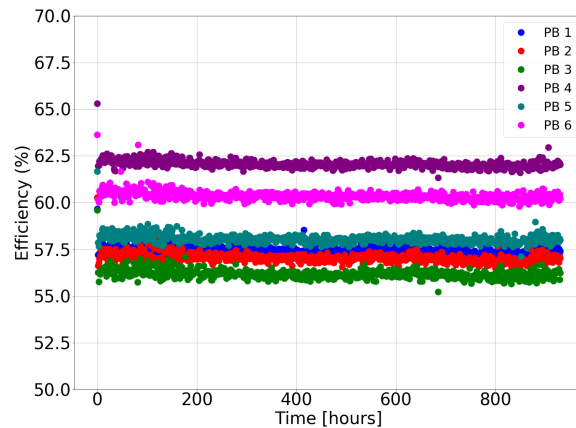


Figure A.14: Efficiency of the power board as a function of time for 12 November 2018 - 24 January 2019 run.

the current drawn by the DC load was varied and the efficiency at each temperature for various current drawn was measured. In addition to this, various AMAC channels like the NTC, PTAT, input voltage and current, output voltage and current were monitored. The saturation of the AMAC responses at high temperatures was also measured.

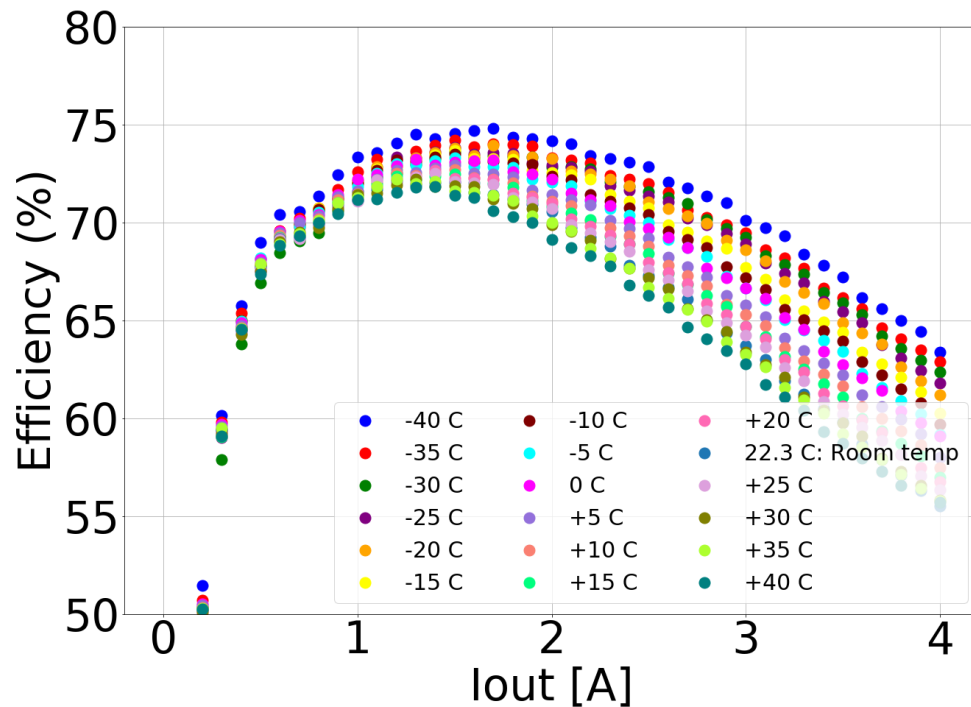


Figure A.15: Efficiency as a function of current output by the power board. The power board is most efficient at the lowest temperature and the efficiency drops as the temperature increases.

The efficiency of the power board as a function of current drawn by the DC load at a constant input voltage of 11 V is shown in Figure A.15 for a range of possible operating temperatures. For comparison, Figure A.5 gives a similar plot at a temperature of approximately 22° C where the maximum efficiency is approximately 72%. Figure A.15 shows the efficiency of the power board is higher at lower temperature and gets worse at high temperature, as expected. At 3 A current output, the efficiency ranges from 63% to 70% in the temperature ranges from -40° C to +40° C.

Some of the AMAC channels saturated at high temperature when high current is drawn from the power board. For example, the ADC counts for output current measured from the AMAC as a function of output current, measured from the variable load is shown in Figure A.16. The ADC values saturate at approximately 3 A at +40° C. This is due to the Over-Temperature Protection on the FEAST which turns off the converter at high temperature of around 100° C and this study verified its function.

As the load draws more current from the power board, the FEAST heats up. We monitor

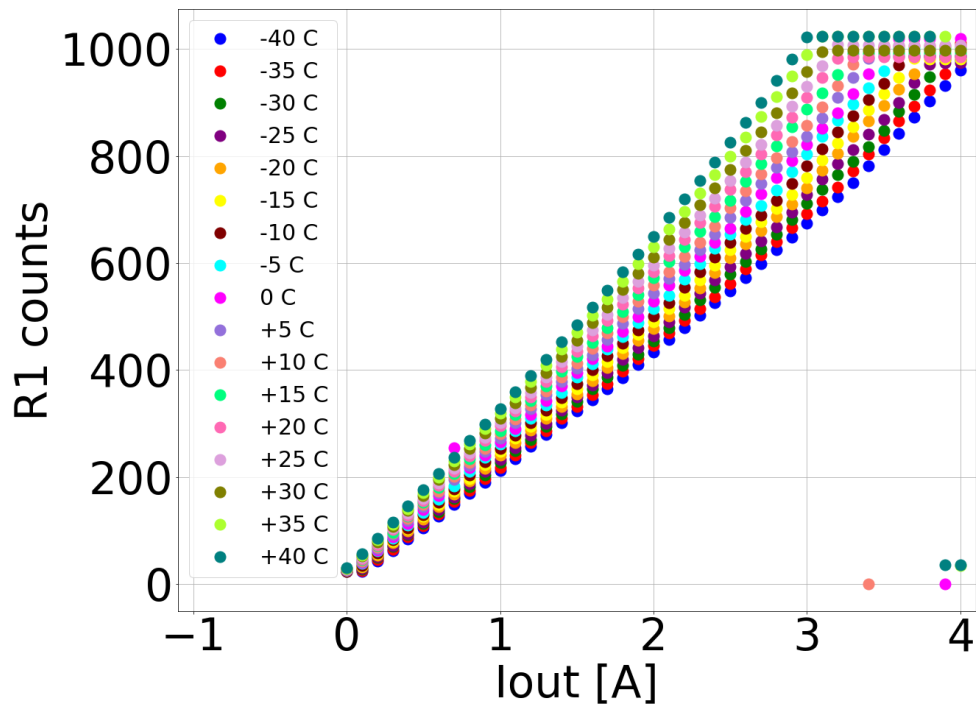


Figure A.16: ADC counts from R1 (output current) channel on AMAC on Y-axis and output current measured from the variable load on X-axis.

this heating with help of a PTAT (Proportional To Absolute Temperature) device located at the FEAST and read it out through the AMAC. As the name suggests, the ADC counts on this device is indeed proportional to the absolute temperature and hence to temperature in Celsius. For calibration of this device, we use the fact that initially when no current is drawn from the power board, the PTAT temperature should be the same as that of the climate chamber. Hence, at every temperature, we use the PTAT counts when Iout is 0 A and correlate it to the climate chamber temperature as given in Figure A.17. The slope in this figure is used as the calibration for the PTAT readings.

Using this calibration, the PTAT ADC counts are converted to the corresponding temperature in Celsius and the result is shown in Figure A.18. The FEAST heated up as more current is drawn from the power board and at higher temperature, the maximum temperature reached is higher. The FEAST has Over-Temperature Protection (OTP) which disables the FEAST when the temperature reaches about 103° C. This is reflected in the figure for climate chamber temperature of +40° C and a load current of 3.5 A.

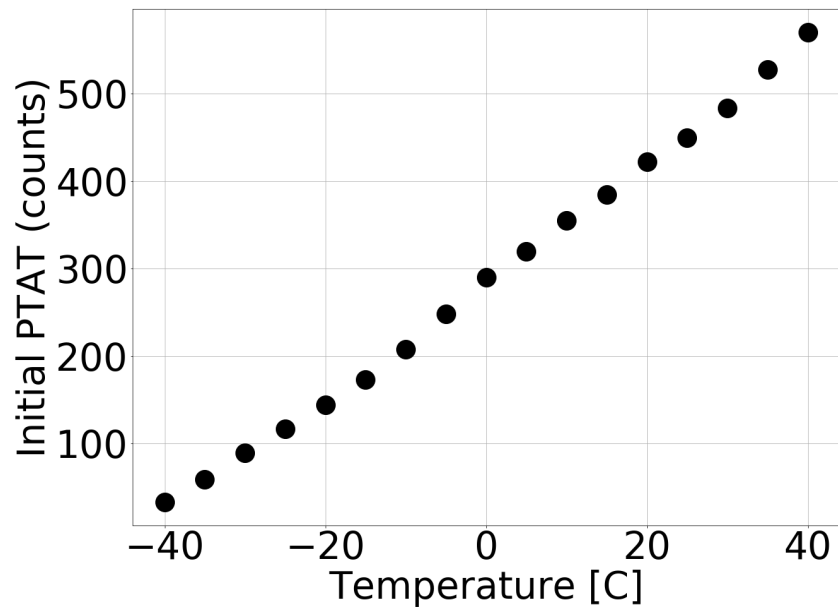


Figure A.17: PTAT calibration curve with PTAT ADC counts at 0A output current on Y-axis and the climate chamber temperature on X-axis.

The power board also has another temperature device, NTC (Negative Temperature Coefficient), at the AMAC. This NTC device is placed in series with a 500 Ohm resistor. After taking this into account and using a factory B value of 4500 and characteristic resistance R_0 is 1 kOhm, the temperature from the NTC device was calculated. The temperature at the AMAC as a function of current drawn from the power board is shown in Figure A.19. We see that the temperature rises as a function of current drawn and the maximum temperature reached is highest at +40° C. The temperature rise measured from NTC was significantly less when compared to the PTAT because the PTAT is located near the FEAST which has higher heat dissipation compared to the other parts of the power board.

This concluded the various tests performed by the author on the power board but note that further efforts in reliability testing continue at the Lawrence Berkeley National Laboratory (LBNL).

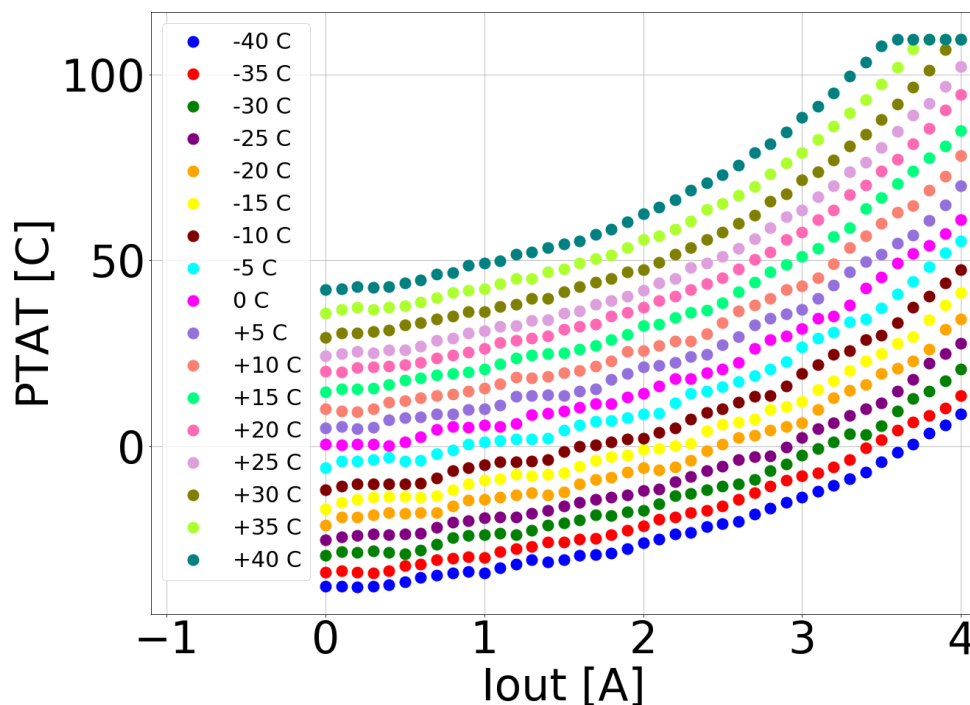


Figure A.18: Temperature of the FEAST, measured from PTAT, as a function of current drawn from the power board.

A.6 Summary and outlook

The performance of the power board version 2 under various stress conditions was studied. The effects of power cycling, temperature and long term power-on test was quantified for the first time. The power board works according to the design specifications under these stress conditions. More studies beyond what is outlined here are necessary to estimate the reliability of the power board which are underway at LBNL. The results from these studies helped design the tests that are running at LBNL, such as the long term power-on tests for multiple power boards in a cold environment. This will help assess the power board under realistic temperature conditions. All of these tests will help estimate the reliability of the power board and ensure it outlasts the HL-LHC era.

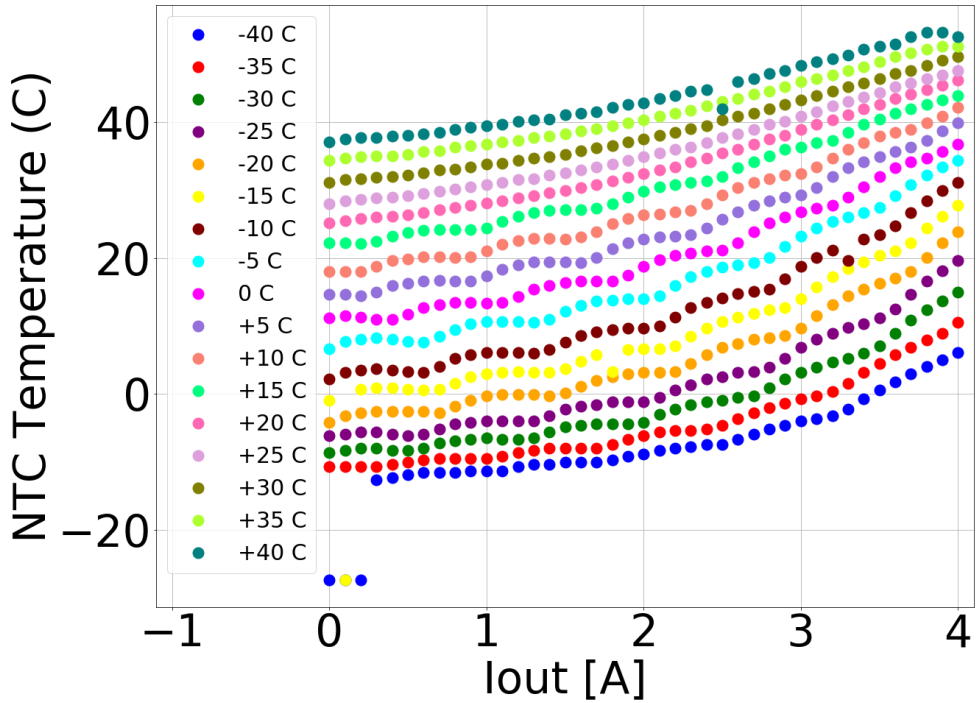


Figure A.19: NTC temperature as a function of current drawn from the power board.

Appendix B

Studying performance of the Strips module using X-ray beams

This appendix summarizes the measurement of the border of the charge collection area on the silicon strip sensors on an ITk strips module under micro-focused X-ray beams.

The ATLAS ITk strips detector is made of silicon strip sensors designed to enable efficient particle detection in a high luminosity environment. The silicon module is shown in Figure A.2 for reference. The sensor consists of 1282 silicon strips (each with 75 μm strip pitch and 300 μm thickness) out of which 1280 are read out using the front-end boards while the outermost strip on either side is a field-shaping strip which allows the uniformity of the electric field in the sensor area by grounding these strips. The active charge collection area is surrounded by three implant rings which separate the sensor from the dicing edge shown in Figure B.1. The first ring surrounding the sensors is the bias ring which ensures all the strips have a homogeneous potential. This is followed by the guard ring which smooths the field gradient between the sensor and the edge. The final ring is the edge ring which separates the depleted sensor region from the dicing edge. The sensor design criterion is to minimize the inactive sensor area to ensure detector hermeticity.

The goal of this study is to map the edge of the charge collection area precisely. This is important as it determines the position resolution at the edge of the sensor and is also relevant for accurate hermeticity estimates and tracking performance.

B.1 Experimental setup

A micro-focused (dimensions $\sigma_x \times \sigma_y = 2.6 \times 1.3^2$ X-ray beam with an energy of 15 keV is provided by the Diamond Light Source [83]. The measurements were made using two types of silicon strip modules: a short-strip module with strip length of about 2.5 cm (with an ATLAS12A sensor [84] and ABC130 ASICs [85]) and a long-strip module with strip length of about 5 cm (with an ATLAS17LS sensor [86] and ABCStar ASICs [87]). The X-ray beam is incident at the fully depleted module at a bias voltage of 400 V from two different angles:

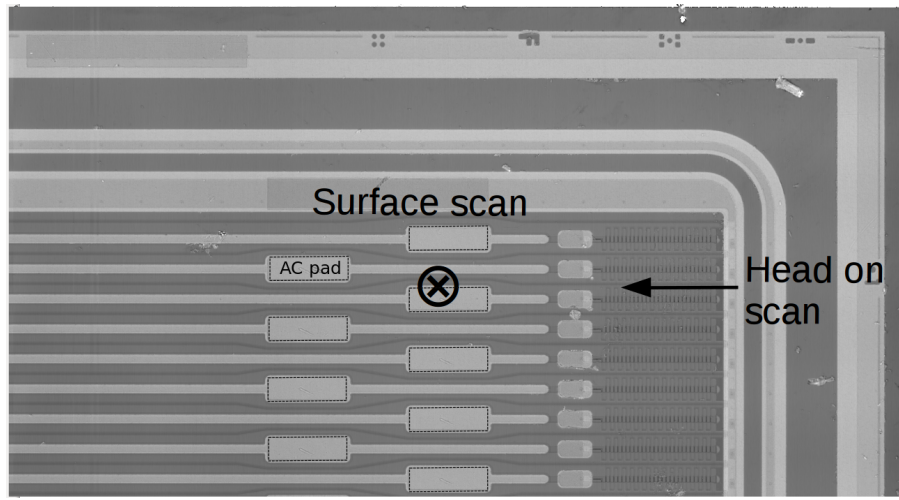


Figure B.1: Sensor corner for silicon sensor shows the active area with individual strip implants including the surrounding bias ring, guard ring and edge ring. The AC pad in the first read-out enabled sensor is shown for reference. The X-ray beam orientations for the surface and head-on scans are also shown here.

perpendicular to the sensor surface (surface scan) and parallel to the sensor surface (head-on scan). The directions of incidence are indicated in Figure B.1. The surface scan allows to scan the charge collection along the strip and across the strip while the head-on scan enables the scan within the sensor thickness. The surface scan is performed using both the short strip and the long strip module while the head-on scan is only done using the short strip module. The X-ray beam is focused on Strip 1 and Strip 2, one at a time and the charge collection pattern is recorded. Note that Strip 0 is not grounded for this study.

The scans target the three consecutive strips located at the sensor edge: field-shaping strip (Strip 0) closest to the sensor edge, followed by Strip 1 and Strip 2.

The setup for the two modules is summarized below:

The short strip module: The sensor is fully depleted and the module is maintained at a temperature of 15°C . The step size of the surface scan is $15\mu\text{m}$ across the strip and $40\mu\text{m}$ along the strip. The step size of the head-on scan is $15\mu\text{m}$ across the strip and $15\mu\text{m}$ along the sensor thickness.

The long strip module: The sensor is fully depleted and maintained at 8°C and the step size is $10\mu\text{m}$ across the strip and $15\mu\text{m}$ along the strip.

B.2 Results

B.2.1 Surface scan

The charge collection pattern in the short strip module from Strip 1 incidence is shown in Figure B.2. The Figure also clearly outlines individual strips and AC pads. This clearly shows the charge collected in the field shaping strip, Strip 0, when Strip 1 is incident. The shape of the charge collection map in Strip 0 agrees with the shape of the strip as can be seen from the AC pad outline. This is clearer from the scan of long strip module. This effect is caused due to the capacitive coupling between Strip 0 and Strip 1. This cross talk between adjacent strip is not expected due to the individual strip isolation and has not been seen for the other adjacent strips. The charge collection from Strip 2 incidence is shown in Figure B.3 and the lack of the hits in Strip 1 indicates negligible cross talk between the strips.

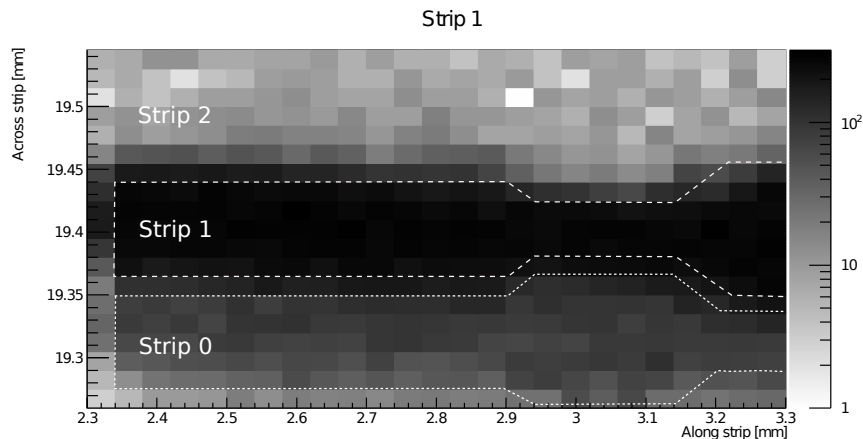


Figure B.2: Charge collection pattern when Strip 1 is incident with X-ray beams is shown here. The individual strips along with the AC pad positions are highlighted here. The X-axis corresponds to the direction along the strip and the Y-axis corresponds to the direction perpendicular to the strip.

Results for the long strip module for Strip 1 and Strip 2 incidence are shown in Figures B.4 and B.5. This data is recorded with finer step size providing a sharper charge collection boundary and a clear strip shape. The results agree with the observations from the short strip module. The charge collection area in Strip 0 clearly shows a wide area consistent with the AC pad of the Strip 0 giving further proof that this is due to the charge coupling between Strip 0 and Strip 1 rather than a generic wide charge collection area of Strip 1. Another feature is the clear alternating AC bond pad positions for the consecutive strips.

B.2.2 Head-on scan

The short strip module is studied using a head-on X-ray beam positioned parallel to the sensor plane. The charge collection pattern is recorded in the sensor thickness and is shown in Figure B.6. This shows a uniform charge collection in the bulk of the silicon sensor along with the charge collection in Strip 0. Note that the beam is lost during this scan due to a power outage resulting in partial data collection. The module is tilted with respect to the beam due to some minor bowing resulting from internal stresses, as the module is not held down by vacuum. This results in the charge collection to different depths for different strips.

The charge collection in Strip 0 when the Strip 1 is incident is due to the charge coupling between these strips. This coupling results in fake hits to be read out by Strip 1 which increases its charge collection area which impacts the position resolution. This effect is seen both on the surface of the silicon sensor and the silicon bulk. Similar study for the charge collection area of the sensor edge is planned with and without the grounded AC pad of the field-shaping strip.

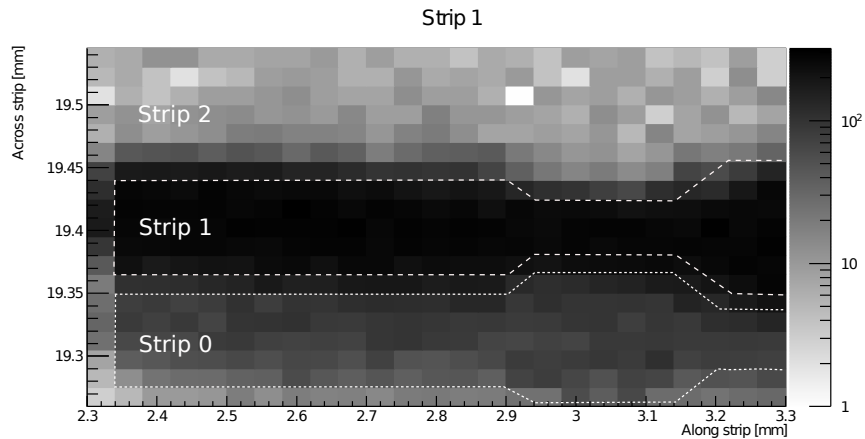


Figure B.3: Charge collection pattern when Strip 2 is incident with X-ray beams is shown here. The individual strips along with the AC pad positions are highlighted here. The X-axis corresponds to the direction along the strip and the Y-axis corresponds to the direction perpendicular to the strip.

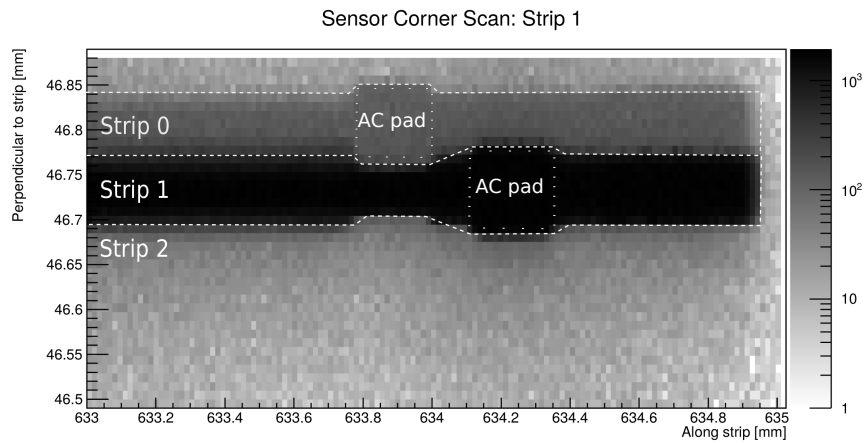


Figure B.4: Charge collection pattern when Strip 1 is incident with X-ray beams is shown here. The individual strips along with the AC pad positions are highlighted here. The X-axis corresponds to the direction along the strip and the Y-axis corresponds to the direction perpendicular to the strip.

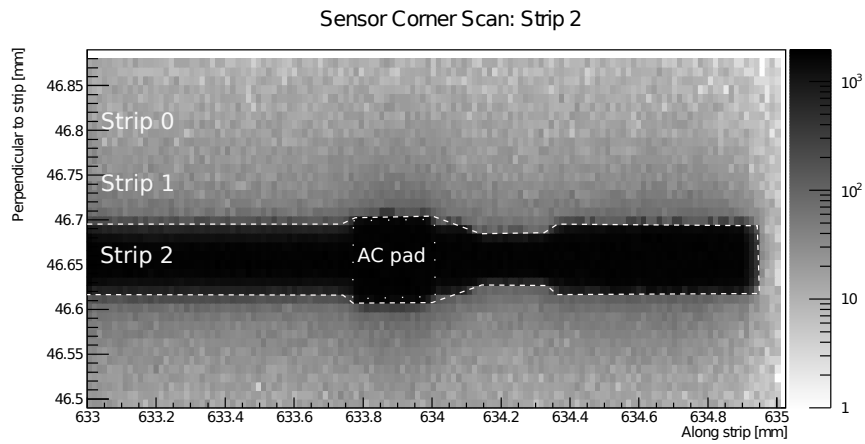


Figure B.5: Charge collection pattern when Strip 2 is incident with X-ray beams is shown here. The individual strips along with the AC pad positions are highlighted here. The X-axis corresponds to the direction along the strip and the Y-axis corresponds to the direction perpendicular to the strip.

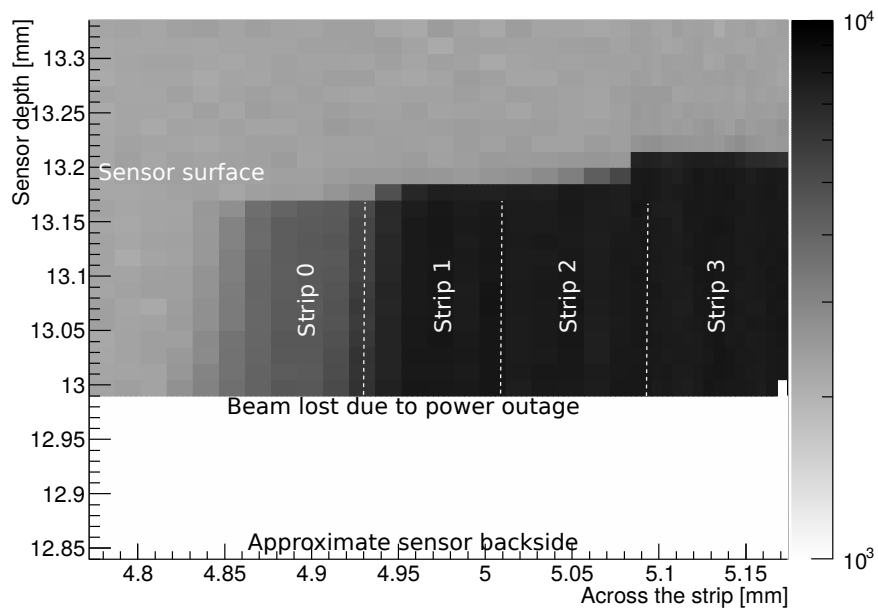


Figure B.6: Charge collection pattern in the bulk of the sensor. The X-axis corresponds to the direction across the strip and the Y-axis corresponds to the sensor depth. The individual strips are outlined here for reference. The sensor tilted here due to internal stresses as it is not held down by a vacuum.

Bibliography

- [1] URL: <https://atlas.cern/>.
- [2] Particle Data Group and Zyla, P A et al. “Review of Particle Physics”. In: *Progress of Theoretical and Experimental Physics* 2020.8 (Aug. 2020). 083C01. ISSN: 2050-3911. DOI: 10.1093/ptep/ptaa104. eprint: <https://academic.oup.com/ptep/article-pdf/2020/8/083C01/34673722/ptaa104.pdf>. URL: <https://doi.org/10.1093/ptep/ptaa104>.
- [3] Sheldon L. Glashow. “Partial-symmetries of weak interactions”. In: *Nuclear Physics* 22.4 (1961), pp. 579–588. ISSN: 0029-5582. DOI: [https://doi.org/10.1016/0029-5582\(61\)90469-2](https://doi.org/10.1016/0029-5582(61)90469-2). URL: <https://www.sciencedirect.com/science/article/pii/0029558261904692>.
- [4] Steven Weinberg. “A Model of Leptons”. In: *Phys. Rev. Lett.* 19 (21 Nov. 1967), pp. 1264–1266. DOI: 10.1103/PhysRevLett.19.1264. URL: <https://link.aps.org/doi/10.1103/PhysRevLett.19.1264>.
- [5] Abdus Salam. “Weak and Electromagnetic Interactions”. In: *Conf. Proc. C* 680519 (1968), pp. 367–377. DOI: 10.1142/9789812795915_0034.
- [6] David J. Gross and Frank Wilczek. “Ultraviolet Behavior of Non-Abelian Gauge Theories”. In: *Phys. Rev. Lett.* 30 (26 June 1973), pp. 1343–1346. DOI: 10.1103/PhysRevLett.30.1343. URL: <https://link.aps.org/doi/10.1103/PhysRevLett.30.1343>.
- [7] URL: https://commons.wikimedia.org/wiki/File:Standard_Model_of_Elementary_Particles.svg.
- [8] G. Aad et al. “Observation of a new particle in the search for the Standard Model Higgs boson with the ATLAS detector at the LHC”. In: *Physics Letters B* 716.1 (2012), pp. 1–29. ISSN: 0370-2693. DOI: <https://doi.org/10.1016/j.physletb.2012.08.020>. URL: <https://www.sciencedirect.com/science/article/pii/S037026931200857X>.
- [9] S. Chatrchyan et al. “Observation of a new boson at a mass of 125 GeV with the CMS experiment at the LHC”. In: *Physics Letters B* 716.1 (2012), pp. 30–61. ISSN: 0370-2693. DOI: <https://doi.org/10.1016/j.physletb.2012.08.021>. URL: <https://www.sciencedirect.com/science/article/pii/S0370269312008581>.

- [10] Y. Fukuda et al. “Evidence for Oscillation of Atmospheric Neutrinos”. In: *Phys. Rev. Lett.* 81 (8 Aug. 1998), pp. 1562–1567. DOI: 10.1103/PhysRevLett.81.1562. URL: <https://link.aps.org/doi/10.1103/PhysRevLett.81.1562>.
- [11] Q.R. Ahmad et al. “Direct Evidence for Neutrino Flavor Transformation from Neutral-Current Interactions in the Sudbury Neutrino Observatory”. In: *Phys. Rev. Lett.* 89 (1 June 2002), p. 011301. DOI: 10.1103/PhysRevLett.89.011301. URL: <https://link.aps.org/doi/10.1103/PhysRevLett.89.011301>.
- [12] T. S. van Albada et al. “Distribution of dark matter in the spiral galaxy NGC 3198.” In: 295 (Aug. 1985), pp. 305–313. DOI: 10.1086/163375.
- [13] Joseph D. Lykken. *Beyond the Standard Model*. 2011. arXiv: 1005.1676 [hep-ph].
- [14] Stephen P. Martin. “A Supersymmetry primer”. In: *Adv. Ser. Direct. High Energy Phys.* 18 (1998). Ed. by Gordon L. Kane, pp. 1–98. DOI: 10.1142/9789812839657_0001. arXiv: hep-ph/9709356.
- [15] Sidney Coleman and Jeffrey Mandula. “All Possible Symmetries of the S Matrix”. In: *Phys. Rev.* 159 (5 July 1967), pp. 1251–1256. DOI: 10.1103/PhysRev.159.1251. URL: <https://link.aps.org/doi/10.1103/PhysRev.159.1251>.
- [16] P. Fayet. “Supersymmetry and weak, electromagnetic and strong interactions”. In: *Physics Letters B* 64.2 (1976), pp. 159–162. ISSN: 0370-2693. DOI: [https://doi.org/10.1016/0370-2693\(76\)90319-1](https://doi.org/10.1016/0370-2693(76)90319-1). URL: <https://www.sciencedirect.com/science/article/pii/0370269376903191>.
- [17] URL: <https://www.slac.stanford.edu/pubs/slacreports/reports17/slac-r-865.pdf>.
- [18] A. Takenaka et al. “Search for proton decay via $p \rightarrow e^+\pi^0$ and $p \rightarrow \mu^+\pi^0$ with an enlarged fiducial volume in Super-Kamiokande I-IV”. In: *Physical Review D* 102.11 (Dec. 2020). DOI: 10.1103/physrevd.102.112011. URL: <https://doi.org/10.1103/5C%2Fphysrevd.102.112011>.
- [19] R. N. Mohapatra and S. Nandi. “New Messenger Sector for Gauge Mediated Supersymmetry Breaking”. In: *Physical Review Letters* 79.2 (July 1997), pp. 181–184. DOI: 10.1103/physrevlett.79.181. URL: <https://doi.org/10.1103%5C%2Fphysrevlett.79.181>.
- [20] URL: <https://atlas.cern/updates/briefing/strengthening-SUSY-searches>.
- [21] G. Aad et al. “Combined measurements of Higgs boson production and decay using up to 80 fb^{-1} of proton-proton collision data at $\sqrt{s} = 13 \text{ TeV}$ collected with the ATLAS experiment”. In: *Physical Review D* 101.1 (Jan. 2020). DOI: 10.1103/physrevd.101.012002. URL: <https://doi.org/10.1103%5C%2Fphysrevd.101.012002>.

- [22] Khilesh Pradip Mistry, Christopher Meyer, and Hugh Williams. *Supporting Note: Search for Rare Higgs Decays to Neutralinos and Gravitinos with 2015+2016+2017 13 TeV data*. Tech. rep. Geneva: CERN, Mar. 2018. URL: <https://cds.cern.ch/record/2306702>.
- [23] G. Aad et al. “Search for nonpointing photons in the diphoton and E_T^{miss} final state in $\sqrt{s}=7$ TeV proton-proton collisions using the ATLAS detector”. In: *Physical Review D* 88.1 (July 2013). DOI: 10.1103/physrevd.88.012001. URL: <https://doi.org/10.1103%5C%2Fphysrevd.88.012001>.
- [24] G. Aad et al. “Search for nonpointing and delayed photons in the diphoton and missing transverse momentum final state in 8 TeV pp collisions at the LHC using the ATLAS detector”. In: *Physical Review D* 90.11 (Dec. 2014). DOI: 10.1103/physrevd.90.112005. URL: <https://doi.org/10.1103%5C%2Fphysrevd.90.112005>.
- [25] A. M. Sirunyan et al. “Search for long-lived particles using delayed photons in proton-proton collisions at $\sqrt{s} = 13$ TeV”. In: *Phys. Rev. D* 100 (11 Dec. 2019), p. 112003. DOI: 10.1103/PhysRevD.100.112003. URL: <https://link.aps.org/doi/10.1103/PhysRevD.100.112003>.
- [26] Thomas Sven Pettersson and P Lefèvre. *The Large Hadron Collider: conceptual design*. Tech. rep. Oct. 1995. URL: <https://cds.cern.ch/record/291782>.
- [27] Oliver Sim Brüning et al. *LHC Design Report*. CERN Yellow Reports: Monographs. Geneva: CERN, 2004. DOI: 10.5170/CERN-2004-003-V-1. URL: <https://cds.cern.ch/record/782076>.
- [28] Christiane Lefèvre. “The CERN accelerator complex. Complexe des accélérateurs du CERN”. Dec. 2008. URL: <https://cds.cern.ch/record/1260465>.
- [29] G. Aad et al. “The ATLAS Experiment at the CERN Large Hadron Collider”. In: *JINST* 3 (2008). Also published by CERN Geneva in 2010, S08003. 437 p. DOI: 10.1088/1748-0221/3/08/S08003. URL: <https://cds.cern.ch/record/1129811>.
- [30] S. Chatrchyan et al. “The CMS experiment at the CERN LHC. The Compact Muon Solenoid experiment”. In: *JINST* 3 (2008). Also published by CERN Geneva in 2010, S08004. 361 p. DOI: 10.1088/1748-0221/3/08/S08004. URL: <https://cds.cern.ch/record/1129810>.
- [31] A. Augusto Alves et al. “The LHCb Detector at the LHC”. In: *JINST* 3 (2008). Also published by CERN Geneva in 2010, S08005. DOI: 10.1088/1748-0221/3/08/S08005. URL: <https://cds.cern.ch/record/1129809>.
- [32] K. Aamodt et al. “The ALICE experiment at the CERN LHC. A Large Ion Collider Experiment”. In: *JINST* 3 (2008). Also published by CERN Geneva in 2010, S08002. 259 p. DOI: 10.1088/1748-0221/3/08/S08002. URL: <https://cds.cern.ch/record/1129812>.
- [33] Werner Herr and B Muratori. “Concept of luminosity”. In: (2006). DOI: 10.5170/CERN-2006-002.361. URL: <https://cds.cern.ch/record/941318>.

- [34] G. Avoni et al. “The new LUCID-2 detector for luminosity measurement and monitoring in ATLAS”. In: *JINST* 13 (2018), P07017. 33 p. DOI: 10.1088/1748-0221/13/07/P07017. URL: <http://cds.cern.ch/record/2633501>.
- [35] G. Aad et al. “Improved luminosity determination in pp collisions at $\sqrt{s} = 7$ TeV using the ATLAS detector at the LHC”. In: *The European Physical Journal C* 73.8 (Aug. 2013). ISSN: 1434-6052. DOI: 10.1140/epjc/s10052-013-2518-3. URL: <http://dx.doi.org/10.1140/epjc/s10052-013-2518-3>.
- [36] M. Aaboud et al. “Luminosity determination in pp collisions at $\sqrt{s} = 8$ TeV using the ATLAS detector at the LHC”. In: *The European Physical Journal C* 76.12 (Nov. 2016). ISSN: 1434-6052. DOI: 10.1140/epjc/s10052-016-4466-1. URL: <http://dx.doi.org/10.1140/epjc/s10052-016-4466-1>.
- [37] *Luminosity determination in pp collisions at $\sqrt{s} = 13$ TeV using the ATLAS detector at the LHC*. Tech. rep. Geneva: CERN, June 2019. URL: <http://cds.cern.ch/record/2677054>.
- [38] Joao Pequenaio. “Computer generated image of the whole ATLAS detector”. Mar. 2008. URL: <https://cds.cern.ch/record/1095924>.
- [39] *ATLAS inner detector: Technical Design Report, 1*. Technical design report. ATLAS. Geneva: CERN, 1997. URL: <https://cds.cern.ch/record/331063>.
- [40] M Capeans et al. *ATLAS Insertable B-Layer Technical Design Report*. Tech. rep. Sept. 2010. URL: <https://cds.cern.ch/record/1291633>.
- [41] Joao Pequenaio. “Computer generated image of the ATLAS inner detector”. Mar. 2008. URL: <https://cds.cern.ch/record/1095926>.
- [42] G. Aad et al. “ATLAS pixel detector electronics and sensors”. In: *JINST* 3 (2008), P07007. DOI: 10.1088/1748-0221/3/07/P07007. URL: <https://cds.cern.ch/record/1119279>.
- [43] A. Ahmad et al. *The Silicon Microstrip Sensors of the ATLAS Semiconductor Tracker*. Tech. rep. Geneva: CERN, Mar. 2007. DOI: 10.1016/j.nima.2007.04.157. URL: <https://cds.cern.ch/record/1019885>.
- [44] T. Åkesson et al. “Status of design and construction of the transition radiation tracker (TRT) for the ATLAS experiment at the LHC”. In: *Nucl. Instrum. Methods Phys. Res., A* 522 (2004), pp. 131–145. DOI: 10.1016/j.nima.2004.01.033. URL: <http://cds.cern.ch/record/818540>.
- [45] Joao Pequenaio. “Computer Generated image of the ATLAS calorimeter”. Mar. 2008. URL: <https://cds.cern.ch/record/1095927>.
- [46] *ATLAS liquid-argon calorimeter: Technical Design Report*. Technical design report. ATLAS. Geneva: CERN, 1996. URL: <https://cds.cern.ch/record/331061>.

- [47] G. Aad et al. “Readiness of the ATLAS Liquid Argon Calorimeter for LHC Collisions. Readiness of the ATLAS Liquid Argon Calorimeter for LHC Collisions”. In: *Eur. Phys. J. C* 70 (May 2010), 723–753. 31 p. DOI: 10.1140/epjc/s10052-010-1354-y. arXiv: 0912.2642. URL: <https://cds.cern.ch/record/1228823>.
- [48] *ATLAS tile calorimeter: Technical Design Report*. Technical design report. ATLAS. Geneva: CERN, 1996. URL: <https://cds.cern.ch/record/331062>.
- [49] G. Aad et al. “Readiness of the ATLAS Tile Calorimeter for LHC collisions”. In: *The European Physical Journal C* 70.4 (Dec. 2010), pp. 1193–1236. ISSN: 1434-6052. DOI: 10.1140/epjc/s10052-010-1508-y. URL: <http://dx.doi.org/10.1140/epjc/s10052-010-1508-y>.
- [50] G. Aad et al. “The ATLAS Experiment at the CERN Large Hadron Collider”. In: *JINST* 3 (2008). Also published by CERN Geneva in 2010, S08003. 437 p. DOI: 10.1088/1748-0221/3/08/S08003. URL: <https://cds.cern.ch/record/1129811>.
- [51] *ATLAS muon spectrometer: Technical Design Report*. Technical design report. ATLAS. Geneva: CERN, 1997. URL: <https://cds.cern.ch/record/331068>.
- [52] Joao Pequeno. “Computer generated image of the ATLAS Muons subsystem”. Mar. 2008. URL: <https://cds.cern.ch/record/1095929>.
- [53] The ATLAS collaboration. “Operation of the ATLAS trigger system in Run 2”. In: *Journal of Instrumentation* 15.10 (Oct. 2020), P10004–P10004. ISSN: 1748-0221. DOI: 10.1088/1748-0221/15/10/p10004. URL: <http://dx.doi.org/10.1088/1748-0221/15/10/P10004>.
- [54] URL: <https://twiki.cern.ch/twiki/bin/view/AtlasPublic/ApprovedPlotsDAQ>.
- [55] M. Aaboud et al. “Performance of the ATLAS Trigger System in 2015. Performance of the ATLAS Trigger System in 2015”. In: *Eur. Phys. J. C* 77 (Nov. 2016), 317. 76 p. DOI: 10.1140/epjc/s10052-017-4852-3. arXiv: 1611.09661. URL: <https://cds.cern.ch/record/2235584>.
- [56] URL: https://twiki.cern.ch/twiki/bin/view/AtlasPublic/LuminosityPublicRe%20sultsRun2#Multiple_Year_Collision_Plots.
- [57] G Aad. “Performance of electron and photon triggers in ATLAS during LHC Run 2”. In: *Eur. Phys. J. C* 80 (Sept. 2019). 56 pages in total, author list starting page 40, 26 figures, 10 tables, published in EPJC. All figures including auxiliary figures are available at <https://atlas.web.cern.ch/Atlas/GROUPS/PHYSICS/PAPERS/TRIG-2018-05,47>. 56 p. DOI: 10.1140/epjc/s10052-019-7500-2. arXiv: 1909.00761. URL: <https://cds.cern.ch/record/2688248>.
- [58] G. Aad et al. “Performance of the ATLAS muon triggers in Run 2”. In: *JINST* 15 (Apr. 2020), P09015. 60 p. DOI: 10.1088/1748-0221/15/09/p09015. arXiv: 2004.13447. URL: <http://cds.cern.ch/record/2716326>.

- [59] Johan Alwall et al. “MadGraph 5: going beyond”. In: *Journal of High Energy Physics* 2011.6 (June 2011). DOI: 10.1007/jhep06(2011)128. URL: <https://doi.org/10.1007%5C%2Fjhep06%5C%282011%5C%29128>.
- [60] Richard D. Ball et al. “Parton distributions for the LHC run II”. In: *Journal of High Energy Physics* 2015.4 (Apr. 2015). DOI: 10.1007/jhep04(2015)040. URL: <https://doi.org/10.1007%5C%2Fjhep04%5C%282015%5C%29040>.
- [61] CERN. *CERN Yellow Reports: Monographs, Vol 2 (2017): Handbook of LHC Higgs cross sections: 4. Deciphering the nature of the Higgs sector*. en. 2017. DOI: 10.23731/CYRM-2017-002. URL: <https://e-publishing.cern.ch/index.php/CYRM/issue/view/32>.
- [62] Torbjörn Sjöstrand et al. “An introduction to PYTHIA 8.2”. In: *Computer Physics Communications* 191 (June 2015), pp. 159–177. DOI: 10.1016/j.cpc.2015.01.024. URL: <https://doi.org/10.1016%5C%2Fj.cpc.2015.01.024>.
- [63] *ATLAS Pythia 8 tunes to 7 TeV data*. Tech. rep. All figures including auxiliary figures are available at <https://atlas.web.cern.ch/Atlas/GROUPS/PHYSICS/PUBNOTES/ATL-PHYS-PUB-2014-021>. Geneva: CERN, Nov. 2014. URL: <https://cds.cern.ch/record/1966419>.
- [64] S. Agostinelli et al. “Geant4—a simulation toolkit”. In: *Nuclear Instruments and Methods in Physics Research Section A: Accelerators, Spectrometers, Detectors and Associated Equipment* 506.3 (2003), pp. 250–303. ISSN: 0168-9002. DOI: [https://doi.org/10.1016/S0168-9002\(03\)01368-8](https://doi.org/10.1016/S0168-9002(03)01368-8). URL: <https://www.sciencedirect.com/science/article/pii/S0168900203013688>.
- [65] *The ATLAS Collaboration Software and Firmware*. Tech. rep. Geneva: CERN, May 2021. URL: <https://cds.cern.ch/record/2767187>.
- [66] Enrico Bothmann et al. “Event generation with Sherpa 2.2”. In: *SciPost Physics* 7.3 (Sept. 2019). DOI: 10.21468/scipostphys.7.3.034. URL: <https://doi.org/10.21468%5C%2Fscipostphys.7.3.034>.
- [67] Paolo Nason. “A New Method for Combining NLO QCD with Shower Monte Carlo Algorithms”. In: *Journal of High Energy Physics* 2004.11 (Nov. 2004), pp. 040–040. DOI: 10.1088/1126-6708/2004/11/040. URL: <https://doi.org/10.1088%5C%2F1126-6708%5C%2F2004%5C%2F11%5C%2F040>.
- [68] Joao Pequeno and Paul Schaffner. “How ATLAS detects particles: diagram of particle paths in the detector”. Jan. 2013. URL: <https://cds.cern.ch/record/1505342>.
- [69] T Cornelissen et al. *Concepts, Design and Implementation of the ATLAS New Tracking (NEWT)*. Tech. rep. Geneva: CERN, Mar. 2007. URL: <https://cds.cern.ch/record/1020106>.

- [70] M. Aaboud et al. “Reconstruction of primary vertices at the ATLAS experiment in Run 1 proton–proton collisions at the LHC”. In: *The European Physical Journal C* 77.5 (May 2017). DOI: 10.1140/epjc/s10052-017-4887-5. URL: <https://doi.org/10.1140%5C%2Fepjc%5C%2Fs10052-017-4887-5>.
- [71] G. Aad et al. “Topological cell clustering in the ATLAS calorimeters and its performance in LHC Run 1”. In: *The European Physical Journal C* 77.7 (July 2017). DOI: 10.1140/epjc/s10052-017-5004-5. URL: <https://doi.org/10.1140%5C%2Fepjc%5C%2Fs10052-017-5004-5>.
- [72] G. Aad et al. “Electron and photon performance measurements with the ATLAS detector using the 2015–2017 LHC proton-proton collision data”. In: *Journal of Instrumentation* 14.12 (Dec. 2019), P12006–P12006. DOI: 10.1088/1748-0221/14/12/p12006. URL: <https://doi.org/10.1088%5C%2F1748-0221%5C%2F14%5C%2F12%5C%2Fp12006>.
- [73] M. Aaboud et al. “Jet reconstruction and performance using particle flow with the ATLAS Detector”. In: *The European Physical Journal C* 77.7 (July 2017). DOI: 10.1140/epjc/s10052-017-5031-2. URL: <https://doi.org/10.1140%5C%2Fepjc%5C%2Fs10052-017-5031-2>.
- [74] G. Aad et al. “Topological cell clustering in the ATLAS calorimeters and its performance in LHC Run 1”. In: *The European Physical Journal C* 77.7 (July 2017). DOI: 10.1140/epjc/s10052-017-5004-5. URL: <https://doi.org/10.1140%5C%2Fepjc%5C%2Fs10052-017-5004-5>.
- [75] Matteo Cacciari, Gavin P Salam, and Gregory Soyez. “The anti-ktjet clustering algorithm”. In: *Journal of High Energy Physics* 2008.04 (Apr. 2008), pp. 063–063. DOI: 10.1088/1126-6708/2008/04/063. URL: <https://doi.org/10.1088%5C%2F1126-6708%5C%2F2008%5C%2F04%5C%2F063>.
- [76] G. Aad et al. “Muon reconstruction performance of the ATLAS detector in proton–proton collision data at $\sqrt{s} = 13$ TeV”. In: *The European Physical Journal C* 76.5 (May 2016). DOI: 10.1140/epjc/s10052-016-4120-y. URL: <https://doi.org/10.1140%5C%2Fepjc%5C%2Fs10052-016-4120-y>.
- [77] G. Aad et al. “Muon reconstruction and identification efficiency in ATLAS using the full Run 2 pp collision data set at $\sqrt{s} = 13$ TeV”. In: *Eur. Phys. J., C* 81 (Dec. 2020). 64 pages in total, author list starting page 42, auxiliary material starting at page 59, 34 figures, 3 tables. All figures including auxiliary figures are available at <https://atlas.web.cern.ch/Atlas/GROUPS/PHYSICS/PAPERS/MUON-2018-03/>, 578. 44 p. DOI: 10.1140/epjc/s10052-021-09233-2. arXiv: 2012.00578. URL: <https://cds.cern.ch/record/2746302>.
- [78] M. Aaboud et al. “Performance of missing transverse momentum reconstruction with the ATLAS detector using proton–proton collisions at $\sqrt{s} = 13$ TeV”. In: *The European Physical Journal C* 78.11 (Nov. 2018). DOI: 10.1140/epjc/

- s10052-018-6288-9. URL: <https://doi.org/10.1140/5C%2Fepjc%5C%2Fs10052-018-6288-9>.
- [79] W.E. Cleland and E.G. Stern. “Signal processing considerations for liquid ionization calorimeters in a high rate environment”. In: *Nuclear Instruments and Methods in Physics Research Section A: Accelerators, Spectrometers, Detectors and Associated Equipment* 338.2 (1994), pp. 467–497. ISSN: 0168-9002. DOI: [https://doi.org/10.1016/0168-9002\(94\)91332-3](https://doi.org/10.1016/0168-9002(94)91332-3). URL: <https://www.sciencedirect.com/science/article/pii/0168900294913323>.
- [80] *Luminosity determination in pp collisions at $\sqrt{s} = 13$ TeV using the ATLAS detector at the LHC*. Tech. rep. All figures including auxiliary figures are available at <https://atlas.web.cern.ch/Atlas/GROUPS/PHYSICS/CONFNOTES/ATLAS-CONF-2019-021>. Geneva: CERN, June 2019. URL: <https://cds.cern.ch/record/2677054>.
- [81] *Technical Design Report for the ATLAS Inner Tracker Strip Detector*. Tech. rep. Geneva: CERN, Apr. 2017. URL: <http://cds.cern.ch/record/2257755>.
- [82] URL: https://indico.cern.ch/event/788031/attachments/1794169/2923948/ESE%5C_seminar%5C_Feb19%5C_talk.pdf.
- [83] K. J. S. et al. Sawhney. “A Test Beamline on Diamond Light Source”. In: *AIP Conference Proceedings* 1234.1 (2010), pp. 387–390. DOI: 10.1063/1.3463220. eprint: <https://aip.scitation.org/doi/pdf/10.1063/1.3463220>. URL: <https://aip.scitation.org/doi/abs/10.1063/1.3463220>.
- [84] Y. Unno et al. “Development of n+-in-p large-area silicon microstrip sensors for very high radiation environments – ATLAS12 design and initial results”. In: *Nuclear Instruments and Methods in Physics Research Section A: Accelerators, Spectrometers, Detectors and Associated Equipment* 765 (2014). HSTD-9 2013 - Proceedings of the 9th International ”Hiroshima” Symposium on Development and Application of Semiconductor Tracking Detectors, pp. 80–90. ISSN: 0168-9002. DOI: <https://doi.org/10.1016/j.nima.2014.06.086>. URL: <https://www.sciencedirect.com/science/article/pii/S0168900214008407>.
- [85] K. et al. Mahboubi. “The front-end hybrid for the ATLAS HL-LHC silicon strip tracker”. In: *Journal of Instrumentation* 9.2, C02027 (Feb. 2014), p. C02027. DOI: 10.1088/1748-0221/9/02/C02027.
- [86] Y. et al. Unno. “ATLAS17LS – A large-format prototype silicon strip sensor for long-strip barrel section of ATLAS ITk strip detector”. In: *Nucl. Instrum. Meth. A* 989 (2021), p. 164928. DOI: 10.1016/j.nima.2020.164928.
- [87] W. et al. Lu. “Development of the ABCStar front-end chip for the ATLAS silicon strip upgrade”. In: *Journal of Instrumentation* 12.4 (Apr. 2017), p. C04017. DOI: 10.1088/1748-0221/12/04/C04017.